Determining the Acceleration Mechanism and Topological Structure of Solar Jets: Evidence of Multiple Acceleration Mechanisms in Coronal Jets

By

Samaiyah I. Farid

Dissertation

Submitted to the Faculty of the

Graduate School of Vanderbilt University

in partial fulfillment of the requirements

for the degree of

DOCTOR OF PHILOSOPHY

in

Astrophysics

August 31, 2020

Nashville, Tennessee

Approved:

Keivan Stassun

Andreas Berlind

Kelly Holley-Bockelmann

David Weintraub

Katharine Reeves

TABLE OF CONTENTS

LIST OF TABLES

LIST OF FIGURES

LIST OF ABBREVIATIONS

CCD Charge Coupled Device

FWHM Full Width Half-Maximum

POS Plane-of-Sky

Chapter 1

Introduction

1.1 The Solar Corona

Our closest star, the Sun, is a G-type yellow dwarf around 4.6 billion years old. It is a main-sequence star, i.e. half-way through its lifetime and will continue fusing hydrogen in its core until the helium is depleted and the outer layers are swept away leaving a white dwarf. Like other main-sequence stars, the Sun creates a magnetic field though vigorous interior motions. The manifestation of the magnetic field is the highly stratified, dynamic outer layer of the solar atmosphere, the solar corona. The solar corona is characterized by periodic changes in activity and structure. In particular, the corona produces dynamic eruptions that spew high energy particles and radiation into the interplanetary medium. The catalyst for these eruptions have been investigated for decades, yet a consensus has not been reached. It is well accepted that the fundamental process driving these eruptions involves the release of magnetic energy.However the process of converting magnetic energy into kinetic and thermal energy is still debated. Fundamentally, understanding these eruptions and specifically coronal jets is intertwined with understanding the physical processes that are responsible for energy storage and release in the corona. In the following sections we briefly describe the solar atmosphere and coronal eruptions, in relation to coronal jets. Specifically I discuss jet morphological and physical properties, associated magnetic properties, as well their relationship to other solar phenomena.

1.2 Eruptions in Solar Atmosphere

The layers of the solar atmosphere are delineated based on plasma density, temperature and plasma β (the relationship between gas pressure and magnetic pressure), and include the photosphere, chromosphere, transition region and the corona. The photosphere is a thin region (.5 Mm) of comparatively dense ($10^{23}m^{-3}$) responsible for emitting most of the Sun's light. The chromosphere is characterized by less dense ($10^{17}\mathrm{m}^{-3}$) plasma in the range from 5,000 K to 7,000 K and stretches from 500 km to about 2,000 km. In the upper chromosphere the temperature of the atmosphere rises dramatically to 10^6 K over a very narrow altitude range. This part of the atmosphere is called the transition region. The temperature continues to rise until reaching the outermost layer of the atmosphere, the solar corona (10^{15} - $10^7\mathrm{m}^{-3}$), which extends several solar radii into space and reaches millions of degrees Kelvin. Figure 1.1 shows the solar interior and atmosphere.

The solar atmosphere is in constant motion,and evolves in activity over of a period of 22 years, a time period referred to as the solar cycle. During solar minimum, coronal holes (regions of open magnetic flux) dominate the corona near the poles, spewing the fast solar wind through open magnetic field lines. During solar maximum, sunspots (regions of strong magnetic flux) and subsequently coronal eruptions are more frequent and are responsible for the release of strong eruptions of high energy particles and radiation (called solar flares), and large amounts of mass, called coronal mass ejections.

Eruptions occur over the solar atmosphere and throughout the solar cycle. Figure 1.4 shows some of the eruptions found in different layers of the solar atmosphere. In the chromosphere, dynamic, spike-like eruptions called spicules, dominate the quiet sun and can best be observed at the solar limb. In the transition region and corona, active regions often erupt causing solar flares and sometimes coronal mass ejections. Large coronal eruptions like flares and coronal mass ejections can influence the Earth's magnetosphere where they can trigger magnetic storms, disturbances in communication systems, damage satellites, cause power outages, and expose astronauts to life-threatening radiation. The eruptions of

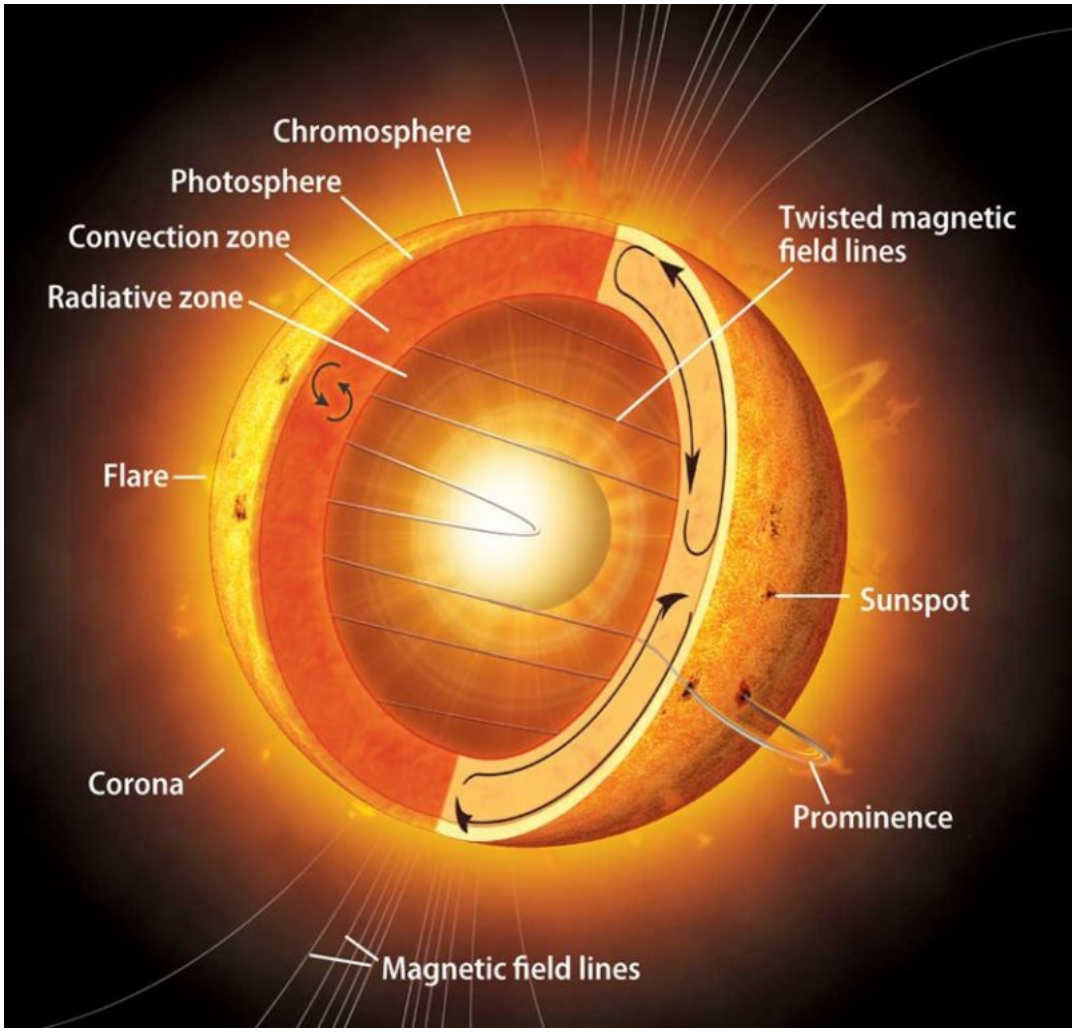

Figure 1.1: Morphology of the Solar Interior and Atmosphere. The dynamics of the upper solar atmosphere (transition region and corona) is dominated by the magnetic field induced by turbulent motions in the Sun's convection zone. Image courtesy of NASA.

coronal jets are on much smaller spatial scales than flares, however they occur much more frequently, and are ubiquitous over the solar cycle and coronal surface. Coronal jets are collimated, beam-like eruptions, that originate in the lower corona and propagate outward along the magnetic field. Jets have various typologies; they are commonly observed with a bright dome-shaped base, and narrow spire, and thus are often described as having an inverted-Y shape, but their spire can also be broad, and helical. See Figure 1.4 and 1.6. Jets are most apparent in EUV and X-ray observations, where they appear bright against

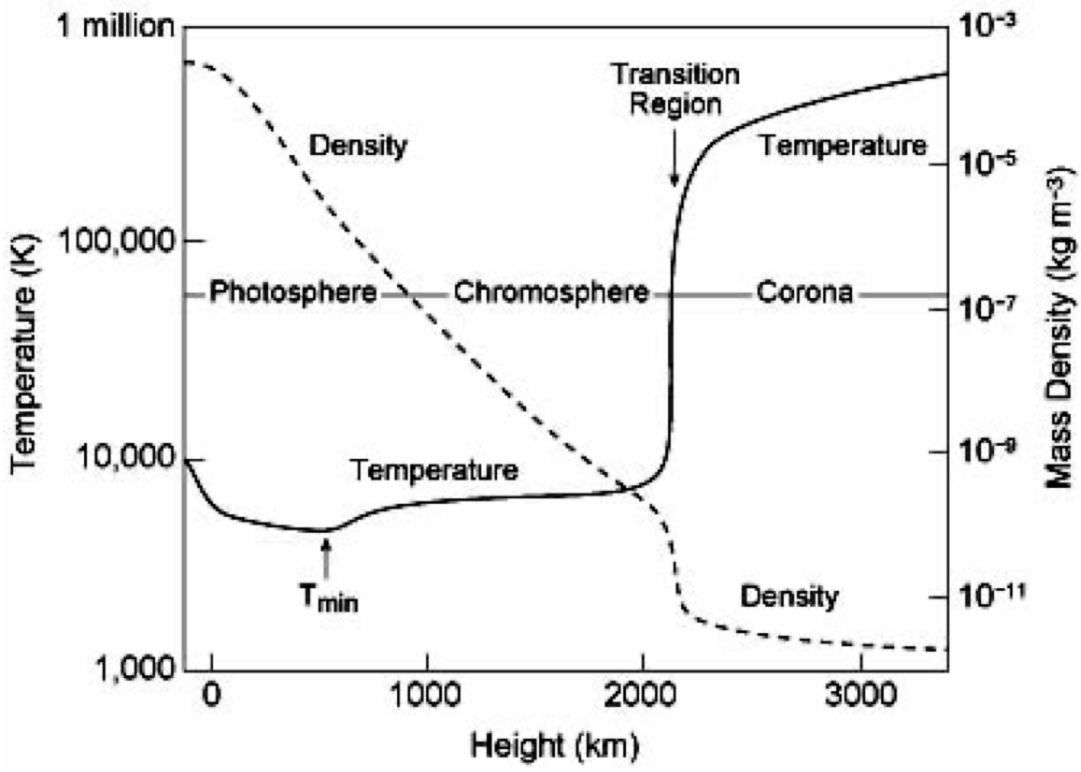

Figure 1.2: Solar atmosphere as a function of height from [Mariska, 1992]. Above the chromosphere, temperature dramatically increases in the transition region, while density decreases exponentially, resulting in low density,10^{-3}kg$m-3$, high temperature (over 1 MK) corona.

dark coronal holes, but are also found in active and quiet sun regions. Studies have found that the formation of jets in the corona occur simultaneously with sudden changes in the underlying magnetic field [Shimojo et al., 1998]. The Figure 1.3 shows a schematic of the canonical example of a coronal jet, where magnetic reconnection occurs between the open region of the ambient magnetic field and closed field of the emerging bipolar region and corresponding jet in AIA 131Å image.

Spicules, coronal jets, mass ejections, and other solar transient eruptions share many common properties. Specifically, they are all thought to be driven by the solar magnetic field [Hale, 1908]. Shown in Figure 1.4a-g are images of the most common types eruptions. The magnetic drivers of coronal mass ejections [Webb et al., 2014], coronal jets

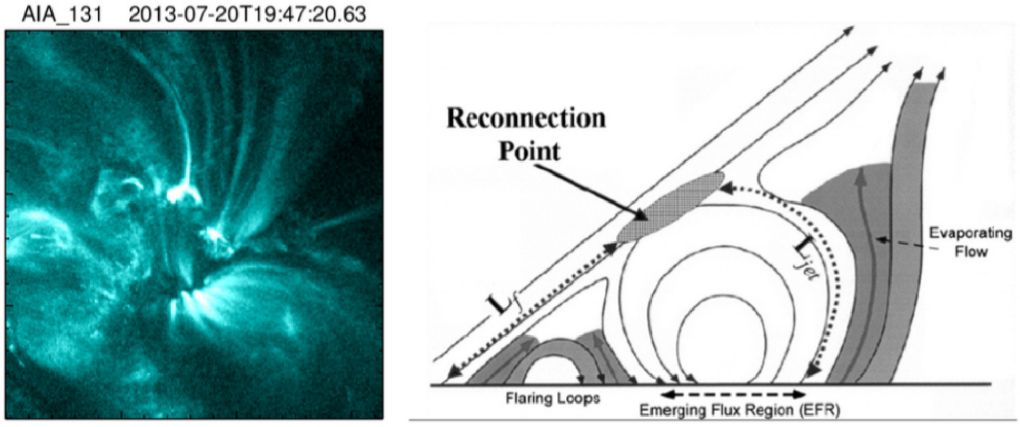

Figure 1.3: Right: Schematic depicting a coronal jet forming as a result of an emerging flux region in a region of open magnetic field. Left: coronal jet in AIA 131Å with narrow spire and dome-shaped base. Figure from [Shimojo et al., 1998]

[Shibata et al., 1992a], and chromopsheric spicules [Athay, 1976, Beckers, 1972, Sterling and Hollweg, 1988] are all thought to be formed from the sudden release of highly stressed magnetic fields. In each case, the key physical processes for producing these eruptions are changes in the magnetic field (flux emergence or cancellation), local enhancement of electric current in the corona (formation of a current sheet), and rapid dissipation of electric current (magnetic reconnection or wave-dissipation) that are responsible for causing shock heating, mass ejection, and particle acceleration. However, the underlying physical mechanisms responsible for initiating, driving, and influencing the evolution of eruptions, specifically coronal jets, is not completely understood. The following sections discuss jet physical properties, associated magnetic properties, their relationship to other phenomena.

1.3 Coronal Jets: Observations and Models

Several decades of coronal observations show that the changes in the morphology and concentration of magnetic fields in the photosphere are related to transient and eruptive events in the solar atmosphere across a range of scales. The process of jet formation and ac-

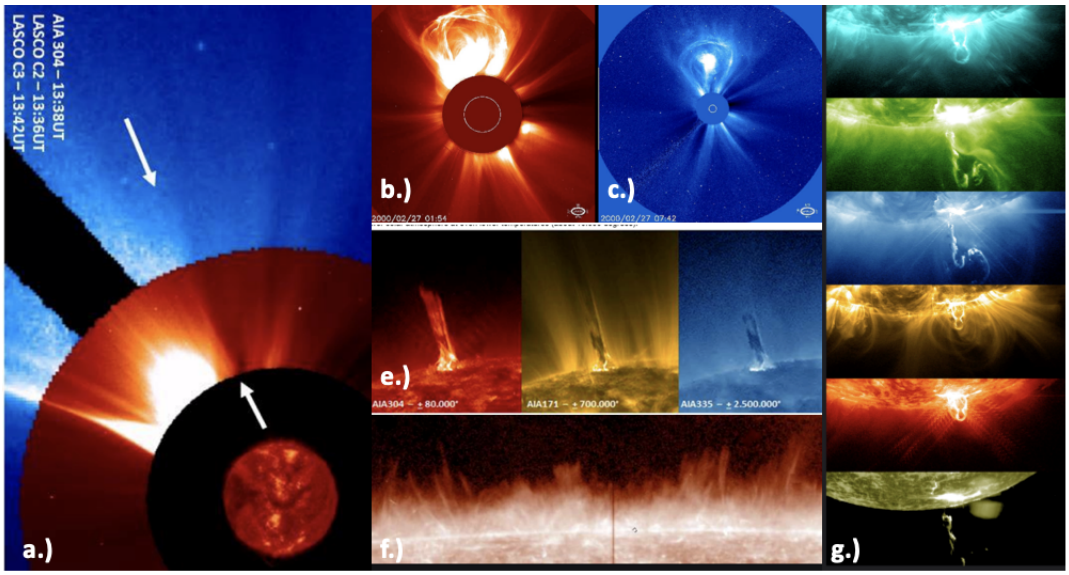

Figure 1.4: Magnetically driven eruptions in the solar atmosphere; spicules(a), coronal jets(b,d), coronal mass ejections(c), and solar flares(e).

celeration is similar to other transient explosive events in that the primary energy is thought to be free magnetic energy, generated and stored by magnetic fields which can then be dissipated in a number of complex ways [Shibata et al., 1992d, Shimojo et al., 1996]. The appearance of jets in EUV wavelengths is associated with changes in the underlying magnetic field, i.e. jets appear as a result of the cancellation, emergence or moving past opposite polarity magnetic flux regions, hinting at their magnetic origin [Shibata et al., 1992b, Moore et al., 2010]. Figure 1.5, from [Panesar et al., 2018], shows the evolution of an EUV jet in 193Å data from the Solar Dynamics Observatory's (SDO) Atmospheric Imaging Array (AIA), which erupts as opposite polarity magnetic flux elements cancel. While magnetic reconnection plays a role in jet formation, the relationship between reconnection and observed plasma parameters is not well understood. Furthermore, once the jet is formed, the plasma can be additionally heated and accelerated by secondary mechanisms throughout the transition region and corona. In the following Chapter, I discuss historical observations of coronal jets, their morphological features, their relationship to other coronal phenomena, and current jet models.

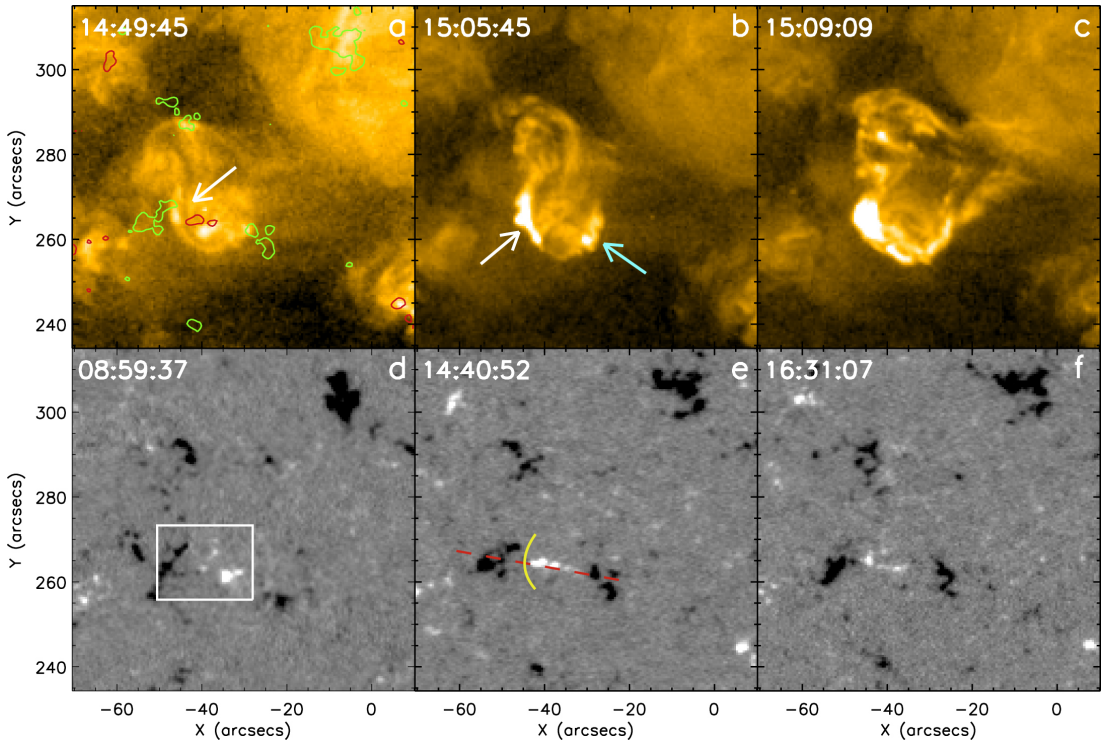

Figure 1.5: Jet evolution in the corona, is associated with changes in magnetic flux in the photosphere. The evolution of a coronal hole jet in EUV AIA193 Å and the corresponding to magnetic cancellation between positive (white) and negative (black) magnetic flux elements. evolution in the underlying magnetic field. Figure from Figure 1 in [Panesar et al., 2018]

1.3.1 Jet Observations

Coronal jets are energetic, small-scale eruptions of plasma typically characterized by a prominent spire, bright loop base, multi-thermal ejecta, and notable changes in underlying magnetic flux. The physical properties of jets have been defined depending on the wavelength band, temperature, and local environment. Therefore they are often grouped by wavelength range, (white-light, EUV and X-ray jets), local environment (active region, quiet sun, and coronal hole jets), or height in solar atmosphere (chromospheric, transition region, coronal jets). Figure 1.6, from Figure 5 in [Moore et al., 2018], shows the onset and evolution of a coronal jet observed in a polar coronal hole using SDO/AIA 193 Å data, corresponding to temperatures of $\sim$ 1.2 million K. The jet begins with a appearance of a small loop region (time 22:05:42 UT). A dense region of cool plasma, called a filament, can be seen rising from the jet base (22:08:06 UT). Filaments appear dark (as absorption) in EUV images because they have comparatively low temperature and high density and they absorb the background EUV emission. The filament later erupts along with the formation of the jet spire (22:11:18 UT). The jet reaches its peak (22:12:54 UT), with a characteristic culminated spire and bright base. In this case, this jet is considered to be a blow-out type, which are commonly observed to have filaments as discussed below.

Jets were first observed in X-ray images from Skylab [Withbroe, 1975], where they appeared as bright linear spires against the dark polar coronal holes. Large scale studies of X-ray jets were first done by [Shibata et al., 1992a, Strong et al., 1992], and [Shimojo et al., 1996] using the Soft X-ray Telescope (SXT) [Tsuneta et al., 1991] aboard Yokhoh [Ogawara et al., 1991]. Jets were found to be throughout the solar corona, appearing in coronal holes, the quiet sun, and on the periphery of active regions and over the solar cycle [Shibata et al., 1992a, Shimojo et al., 1996, Shibata et al., 1992d, Shimojo et al., 1998]. Advancements in EUV instruments allowed large, statistical studies using the Extreme ultraviolet Imaging Telescope (EIT) [Delaboudiniere et al., 1995] and Large Angle and Spectrometric Coronagraph(LASCO) [Brueckner et al., 1995] instruments aboard SOHO

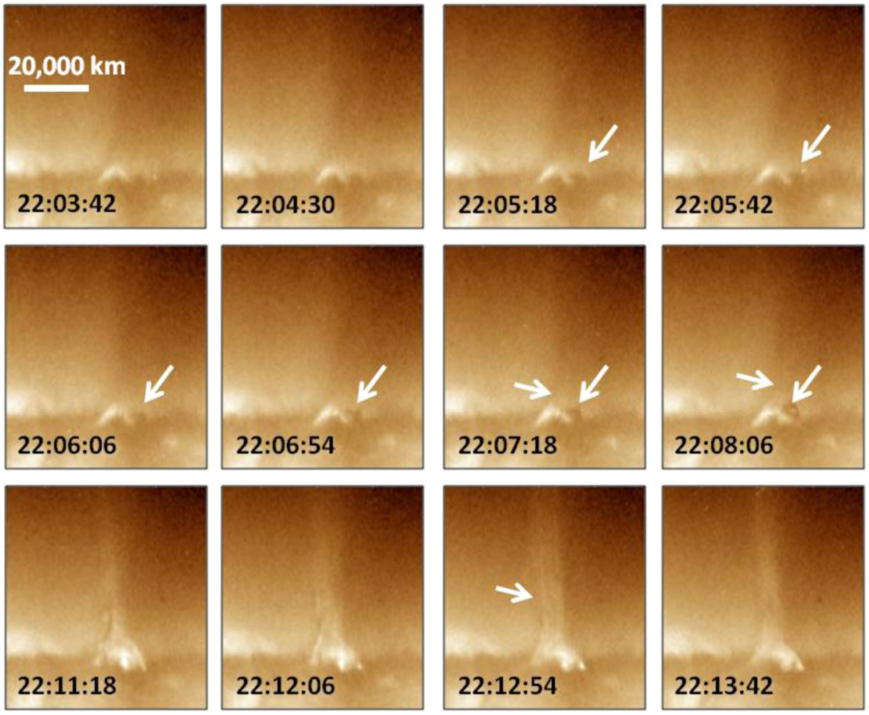

Figure 1.6: Onset and evolution of a coronal jet observed in AIA 193 Å. The jet begins with a appearance of a small loop region (time 22:05:42 UT), a dark filament can be seen rising from the jet base (22:08:06 UT) which later erupts. The jet reaches its peak (22:12:54) with a characteristic culminated spire and bright base. In this case, this jet is considered to be a blow-out type, which are commonly observed to have filaments. From Figure 5 in [Moore et al., 2018].

[Wang et al., 1998, Karovska, 1999, Wood et al., 1999], of primarily polar coronal hole jets. They were found are typically narrow with widths ranging from $1-4x10^4$ km. Jet spire lengths were also found to range from 10^2 to 10^4 km (up to several Mm). Using LASCO, [Wang et al., 1998] found that jets emanating from CHs can extend into the far corona, 3-6 Rs, with substantial mass $(1.5x10^5 cm^{-3})$ and velocities (250 km s^{-1}), fueling the idea that they could deposit substantial mass and energy into the solar wind The jet in Figure 3.1b shows an example of a coronal hole jet spire still intact in the extended corona. During solar maximum, jets also appear near and within ARs. These AR jets are estimated to have higher velocities $\sim$ 600 km/s, up to 800km/s, and appear brighter than coronal hole jets. EUV jet lifetimes range from 10^{-1} to 10^1 hr, and occur $\sim$ 4 times a day [Shibata et al., 1992b, Strong et al., 1992, Shimojo et al., 1996, 1998, Shibata and Magara, 2011].

EUV instruments like EIT [Domingo et al., 1995, Delaboudiniere et al., 1995], the Transition Region and Coronal Explorer (TRACE) [Handy et al., 1999], the Solar Terrestrial Relations Observatory (STEREO)[Kaiser et al., 2008] expanded the observations of jets in the chromosphere and transition region, using high resolutions far and near UV and EUV sensitive bands. Using TRACE, a narrow-band imager with high spatial and temporal resolution, [Alexander and Fletcher, 1999, Jiang et al., 2007, Sakao et al., 2007, Mulay et al., 2017] showed evidence that some jets are often accompanied by a cool component, $\sim .5-.9$MK, often visible in the transition region in EUV emission or in the chromosphere in Lymanα. The cool component is sometimes referred to as a surge [Canfield et al., 1996].

In the past decade, instruments of unprecedented spatial and temporal resolution such as those on Hinode [Kosugi et al., 2007] and the Solar Dynamics Observatory (SDO) [Pesnell et al., 2012], and the Interface Region Imaging Spectrometer (IRIS) [De Pontieu et al., 2014] have provided insight on the complex structure and frequency of coronal jets, and their relationship to other coronal phenomena. High-resolution observations have prompted the suggestion that many jets contain miniature filaments (cool plasma) and/or sigmoids (hot plasma) that erupt to generate the jet [Innes et al., 2009, Raouafi et al., 2010, Hong

et al., 2014, Sterling et al., 2010b, 2015]. These jets also exhibit helical motion or twist during the eruption [Cirtain et al., 2007, Savcheva et al., 2007, Shibata and Magara, 2011, Sterling et al., 2015, Kumar et al., 2018, Shen et al., 2011b]. Stereoscopic observations using STEREO, provide a 3D view of polar jets, confirming helical structure [Patsourakos et al., 2008].

Jet plasma parameters can vary widely. Jet electron temperatures have been found to range from 10^4K to 10^7 K. Similarly, the outflow speeds of jets also vary across bandpass. Outflow speeds can be from 100 to 10^3km/s, near the local Alfvén speed. Jets that occur inside of polar coronal holes are similar to those found in on-disk coronal holes[Nisticò et al., 2010]. Coronal hole jets average speeds of $\sim$ 200 km/s , duration of $\sim$ 30 minutes, and electron temperatures of 4 $-$5x10^6K [Nisticò et al., 2010]. Jets that occur near ARs are roughly a factor 3-6 spatially larger than CH jets and more than one order of magnitude more energetic than QS and CH jets, due to the accumulation of magnetic fluxes associated with the active region. SDO-AIA observations and Hinode Extreme ultraviolet Imaging Spectroscope (EIS) [Young et al., 2007] spectroscopic properties of fast recurring AR jet presented by [Mulay et al., 2016, 2017], estimations of electron temperatures $2x10^6$, and election densities of $1x10^{10}cm^{-3}$, which agree with prior measurements from 10^4K to 10^7K. Jets that originate near the center of the active region or in other closed-loop systems, are confined along the closed loops and often return in-part back to the surface [Hanaoka, 1996, Yang et al., 2012, Cheung et al., 2015, Li et al., 2017]. Conversely, jets that erupt on the AR periphery, near coronal holes, are launched into the open field [Mulay et al., 2016, Chandra, R. et al., 2017].

The energy produced by jets can be substantial. Several studies have observed impulsive solar energetic particle (SEP) events [Nitta et al., 2015, Innes et al., 2016, Glesener and Fleishman, 2018] type III radio bursts [Chen et al., 2018], hard X-rays, and jet-scaled CMEs emitting from active regions jets [Wang et al., 2002, Chifor et al., 2008, Chen et al., 2013].

Helical motions are commonly observed in blowout jets, particularly in ones with an observable filament. [Sterling et al., 2010b,a] suggests the motions are a result of small erupting filament, and that erupting filaments are the mechanism responsible for most (if not all) jets. However not all jets exhibit these motions. In a survey of 15 polar jets, [Moore et al., 2018], found that 6 of the jets were associated with the eruption of a small filament. In a statistical study of X-ray jets [Savcheva et al., 2007, Cirtain et al., 2007], the authors measured the transverse oscillations in jets, finding periods with helical motions of ~ 200 seconds, and a peak-to-peak magnitude of 8000 km, supporting the idea the transverse motions can create Alfvén waves along jet spires, resulting in spire velocities of ~ 800 km/s, close to the local Alfvén speed. Jets can re-occur multiple times in the same location, called homologous jets. [Panesar et al., 2016] analyzed a set of very energetic recurrent active region jets that are tied to mini-CMEs, and compared the eruptions of the CME triggering jets and the non-CME events.

Spectroscopic studies of jets are rare due to the sporadic nature of jets. [Savcheva et al., 2007] presented a statistical study of jets including the observation of transverse motions ~ 35 km/s along the spire. This indirectly hinted at the existence of Alfvénic waves that propagate along the newly reconnected field-lines. Results by [Kim et al., 2007] confirmed using line spectroscopy detecting non-thermal line broadening and Doppler velocities in jet outflows that are associated with traveling Alfvénic waves. Non-thermal broadening effects have been attributed to the presence of magnetic reconnection due to nanoflares[Cargill, 1996], chromospheric evaporation in coronal loops [Patsourakos and Klimchuk, 2006] and/or Alfvén wave shocks [Antolin et al., 2008], Alfvén wave turbulence [van Ballegooijen et al., 2011]. Nanoflare models predict non-thermal velocities of $20 - 36$ kms/s increasing with temperature indicate chromospheric evaporation, velocities near 25-35 km/s are associated with wave turbulence, and velocities of 100 km/s are associated with Alfvén wave shocks [Cargill, 1996, Patsourakos and Klimchuk, 2006, Antolin et al., 2008, van Ballegooijen et al., 2011], so the previous observations agree well with the

constraints predicted by the nanoflare model.

1.3.2 Relationship to Coronal Plumes

Coronal plumes are diffuse, long-lived linear features that appear in the polar coronal holes, and are prominent during solar minimum. Studies using EUV showed that the onsets of polar plumes are associated with jet eruptions [Innes et al., 2016, Raouafi and Stenborg, 2014]. The authors suggest a tendency for plumes to be dependent on the occurrence of transients like small-scale jets and that plumes tend to appear in the same regions after jets have emerged. Thus far the strongest connection appears to be the existence of tiny jet-lets observed within some plumes [Raouafi and Stenborg, 2014], but it is unclear whether all plumes are composed of many such events or whether a different mechanism is responsible for their enhanced density and flows.

1.3.3 Relationship to the Solar Wind

Using both white light and EUV observations, [Wang et al., 1998] found that jets that originated in polar coronal holes, regions of open magnetic flux, have spires that extend to 3.7 solar radii. Intact jets spires have also been observed as far as at 1AU using in-situ measurements [Wang and Sheeley, 2006, Crooker et al., 2012]. Their appearance at such great distances have lead to speculation that they could contribute mass and energy to the solar wind. In addition, the extended spires were found to have speeds of 400-1100 km/sec at the leading edge, but a reduced speed of 250 km/s near the center. [Wang et al., 1998] suggests this deceleration is due to drag forces from the jet interaction with the slower, ambient solar wind. Furthermore, [Bout et al., 2002] found that distances of 3-6 Rs, the density of the extended spires ($2 - 10^5 cm^3$) are up to 50 times the density of the ambient corona($0.3 - 1.5 \times 10^5 cm^3$). Using X-ray observations from Hinode-XRT, [Cirtain et al., 2007, Savcheva et al., 2007], showed that jets occur at much higher rates that previously observed, supporting the idea that they could contribute a substantial amount of energy and

mass into the solar wind.

1.3.4 Observational Evidence of Magnetic Reconnection

Coronal jets and other transient eruptions are thought to be the result of magnetic reconnection. Magnetic reconnection is the conversion of magnetic free energy, stored in highly stressed magnetic fields and released as kinetic energy, radiation, and particle acceleration [Priest et al., 2002]. Evidence of magnetic reconnection in jets, is based on analogous features that indicate reconnection geometry in larger events, like active region flares and CMEs [Tsuneta et al., 1992, Shibata et al., 1992a, Shibata, 1999]. These include X shaped loops, appearance of current sheet, null point, or seperatrix layer, plasmoid ejections and/or filaments, flows and shrinking loops. These features are pointed out in the observation of a flare in Figure 1.7. The X shaped loops (a), are indication of 3-D structure represented in Figure 1.7, where the field lines of the underlying cusp region close in response to reconnection, while the upper region opens and extends [Masuda et al., 1994, Tsuneta, 1996, Su et al., 2013, Gou et al., 2015].

At the magnetic null point (b), the magnetic field goes to 0, coronal resistivity is finite (not zero) and a region of strong currents forms in response to sharp gradients in the magnetic field, referred to as the current sheet. In the 2D model, the current sheet is thin and extends as a result of the topological evolution. In 3D, magnetic nulls and enhanced currents can be found anywhere the magnetic field changes rapidly. The topology is then represented by seperatrix layers, or quasi-seperatrix layers [Sui and Holman, 2003, Liu et al., 2013, Savage et al., 2010, Seaton et al., 2017, Warren et al., 2018], which separate the inner closed loop system from the upper region. Plasmoids (c) are sometimes observed after the initial flare (since it is often too bright). They are small magnetic islands formed as a result of MHD instabilities along the extended current sheet. Active region loops undergo dynamic changes during the flare, outflows(d) and shrinking loops(e) have been observed, as well as inflows(d) of plasma draining from the reconnection site [Shibata, 1995, McKen-

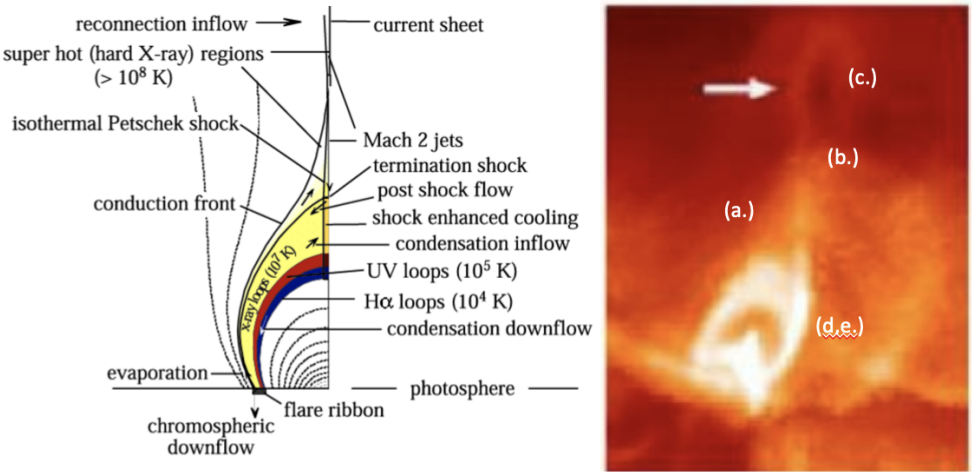

Figure 1.7: Signatures of magnetic reconnection in eruptions.(a) X-shaped loops (b) null-point-like features (c) plasmoid ejections, (d) plasma inflows/outflows,and (e)shrinking loops.Figures adopted from [Forbes and Acton, 1996](left) and [Martens, 2003](right)

zie, 1987, Reeves et al., 2008, 2015, McKenzie and Savage, 2009, Savage et al., 2010, 2012, Liu et al., 2013, Tian et al., 2014, Podgorny and Podgorny, 2020]. The 3-D configuration of the magnetic field and analysis of some of these features can be examined using coronal magnetic field extrapolations, specifically Non-linear Force Free Field (NLFFF) models discussed in Chapter 2.

Magnetic reconnection processes can occur in a slowly, changing in a quasi-steady way, [Parker, 1972, 1983, van Ballegooijen, 1985]), or sudden and violently, as in the processes associated with flares, CMEs, and coronal jets [Tsuneta et al., 1992, Shibata et al., 1992a, Shibata, 1999]. In these cases, potential driving mechanisms are often classified in categories of internal tether-cutting reconnection [Moore et al., 2018, Moore and Sterling, 2006], breakout (external tether-cutting) reconnection ,[Antiochos et al., 1999], and ideal magneto-hydrodynamic (MHD) instabilities [Forbes and Isenberg, 1991, Forbes and Malherbe, 1991, Low and Zhang, 2002, Török et al., 2004, Archontis and Török, 2008]. Before a filament eruption, a bundle of flux ropes are confined by an overarching arcade. A magnetic flux rope is a bundle of twisted helical field lines wrapped around a central

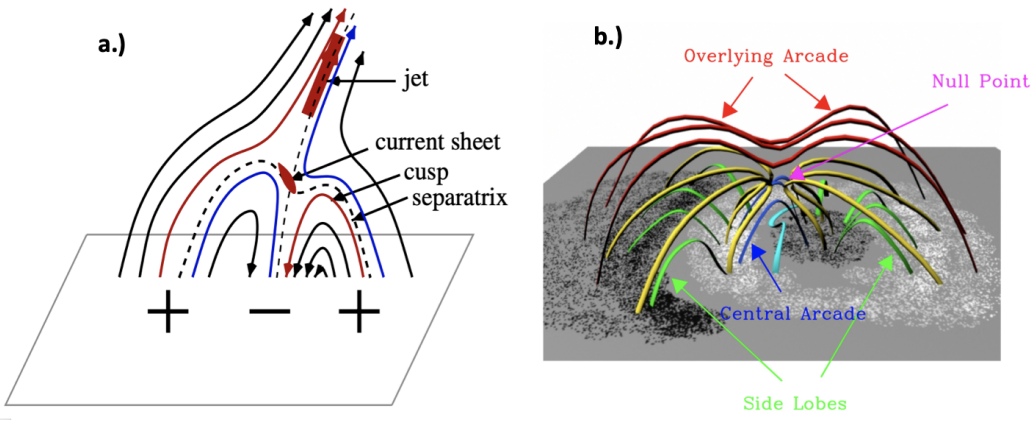

Figure 1.8: a) 3D topological features commonly observed. Figure from [Zhang et al., 2012]. The location of magnetic null, seperatrix layers, current sheet and resulting jet spire. b) Schematic of breakout reconnection from [Chen et al., 2016]. Breakout reconnection occurs when a underlying filament erupts through the overlying arcade.

axial field line. When the flux rope begins to rise reconnection can occur below the flux tube, referred to as tether-cutting reconnection, or between the flux tube and the overlying arcade,referred to breakout reconnection. When breakout reconnection occurs on the exterior of the cusp region (external reconnection), a complex multi-polar configuration forms. In between the overlying arcade, and the filament system, a magnetic null, or seperatrix-fan structure forms. The null and the surrounding separatrix-fan structure are locations in favor of current concentration and magnetic reconnection. Figure 1.8 shows a multi-polar geometry constructed to illustrate some of the key components of a magnetic-breakout setup. The cusp region, X-shaped structures, slowly rising lower arcade are reproduced in simulations [Lynch et al., 2008]. In breakout reconnection, the slow-rise, then sudden eruption of the flux rope is often attributed to an mechanical instability, called kink-mode. Kink-mode instabilities have also been employed to explain the long-lived steady state, then sudden eruption of prominences, CMEs, and the eruption of filaments in coronal jets.

Another manifestation of magnetic reconnection are plasma instabilities. A variety of thermal and MHD instabilities are commonly observed in coronal eruptions, particularly flares [Browning et al., 2008]. Of particular interest are the MHD instabilities observed

in current sheets because they could result in higher reconnection rates and intermittent reconnection, often referred to as bursty reconnection. For the application in this work, we focus the tearing mode, a finite resistive MHD instability. Resistive instabilities appear in in compressible, highly conductive (i.e. low resistivity) plasma,like long current sheets, if the magnetic field lines can move independently of the plasma due to the non-zero resistivity, i.e. if the plasma is not frozen in, and plasma β is > 1, converting magnetic energy into Ohmic heating. The tearing mode instability is the result of a long-waves moving along the electric field lines. They tear, or break up the current sheet, resulting in small plasmoids that appear as small dense regions in EUV and X-ray observations [Wei, 1968, Furth et al., 1963, Bhattacharjee et al., 2009]. Therefore, plasmoid instabilities are expected to occur in solar eruptions, which are driven by magnetic reconnection [Karpen et al., 2012, Shibata, 1999]. Plasmoids are sometimes observed in the long current sheet behind coronal mass ejections [McKenzie and Savage, 2009]. See Figure 1.8. The rare observations of plasmoids in jet spires support the idea that resistive instabilities are at play [Zhang and Ni, 2019, Zhang and Ji, 2014]. Plasmoids that result from instabilities have also been observed in some jet models [Wyper et al., 2019].

1.4 Leading Coronal Jet Models

X-ray and EUV jet are often loosely grouped by morphological features. They are considered to be either *standard* having a narrow spire, or *blowout*; having a broad spire and accompanying filament eruption [Shibata et al., 1992c, Moore et al., 2010]. In the section below, I discuss the umbrella of jet models and how they are applied to the formation of jets. The first two (standard and blowout) models are only representations of the formation process, not physical models.The last three mechanisms (magnetic reconnection, filament eruption, chromospheric evaporation) will be examined closely in this work. Each of these mechanisms may work independently or in tandem to accelerate plasma in jets. MHD models have been able to replicate many of the features presented in the schematics, but

have not produced an accepted, generalized model.

1.4.1 Standard and Blowout Jets

In the process described by [Moore et al., 2010], *standard* jets form when a bipolar magnetic flux region emerges into a mostly unipolar region of the opposite polarity. The ambient magnetic field lines reconnect with the field lines of the emerging flux element via *external* interchange reconnection, forming hot outflows. Standard jets have also been observed to be initiated in other transient photospheric processes, including magnetic flux cancellation [Panesar et al., 2016, 2018, Sterling et al., 2015, 2018], magnetic flux fly-by, flux sheer and/or twist. The defining characteristic of standard jets, is that they maintain a narrow pencil-like outflow regions over their lifetime.

Conversely, *blowout* jets are thought to occur as a result of *internal* reconnection. Work by [Moore et al., 2010, Sterling et al., 2010b, 2019] suggests blowout jets form as a result of small filament eruptions, similar to coronal mass ejections. In that case, mini-filaments form along a sheared polarity inversion line and internal reconnection occurs at the base of the jet, propelling both hot plasma and the cooler filament outward, often referred to as tether-cutting reconnection. Additional external reconnection can also occur on the outer loops of the jet and during the eruption. Blow-out jets are characterized by a broad-spire, and an accompanying cool component in the ejecta. Often blowout jets appear to have helical motions or twist, in the jet spire due to the highly twisted filament at its base. Although filaments have been observed in many jets, not all jets show evidence of a filament or twisting spire as discussed in section 1.3.1 above. However, the eruption of a twisted flux rope could explain observations of twist and/or unwinding motions visible in many blowout jets. In a survey of 15 polar jets, [Moore et al., 2018], found that 6 of the jets could be initiated breakout reconnection, and the eruption of a small filament. Finally, the filament schematic [Sterling et al., 2015], shown in Figure 1.9b, predicts that jets formed through filament eruption should produce a spire that drifts away from the jet's bright point

bright point. While the emerging-flux model,[Moore et al., 2018], shown in Figure 1.9a should result in the spire drifting toward the bright point. In a statistical study of X-ray jets, [Savcheva and van Ballegooijen, 2009] found that the drift is often away from the bright point, supporting the filament eruption model.

1.5 Potential Acceleration Mechanisms

Observations show that jets with similar initiation mechanisms can have a wide range of plasma parameters, non-uniform topological features, and can be found embedded in different coronal environments. Therefore finding a comprehensive explanation of coronal jet formation and acceleration is difficult. MHD models show that models can be accelerated from the tension released during magnetic reconnection, the gas pressure gradient formed during chromospheric evaporation, by the untwisting motion of the field lines, and/or by Alfvénic waves that transverse along newly reconnected field lines. In the sections following we will discuss each of these acceleration mechanisms, and observations features that can be used to distinguish them.

1.5.0.1 Acceleration Due Primarily to Magnetic Reconnection

In a jet where magnetic reconnection is the main accelerator, plasma is accelerated by the 'sling-shot' motion of tangled magnetic field lines relieving magnetic tension. Since the Alfvén velocity is directly proportional to the potential energy of the magnetic field, plasma velocities near the reconnection site are expected to be near or less than the Alfvén velocity. These jets would be similar to standard jets, modeled by [Yokoyama and Shibata, 1995, Miyagoshi and Yokoyama, 2003]. The authors found that if reconnection occurs in the low corona, the plasma flowing toward the reconnection point, in coronal temperatures near 1MK, and is further heated by the reconnection. Therefore, the jet spire should appear in X-rays ($>$ 2MK) with less emission in the chromospshere and transition region. In the framework where reconnection occurs in the transition region or chromosphere, cooler

sub-coronal temperature plasma can be ejected by the straightened magnetic field lines [Yokoyama and Shibata, 1995, Moore et al., 2010], demonstrating that cooler jets are the result of reconnection occurring in the transition region and/or chromosphere while for hotter X-ray jets, reconnection lies in the low corona. These model predicts are consistent with observations of a cool and hot component to blow-out jets [Shen et al., 2017, Zhang and Ni, 2019]. Since this effect involves very small scales (less than 1 km) it is not clear if it can be observed directly, however signatures like heating and bi-directional flows could indicate the location of the reconnection region. [Moore et al., 2010] suggested a magnetic configuration that consists of a highly sheared core field of the emerging flux, and an adjacent open field from the ambient corona, called interchange reconnection. Because the emerging field is highly twisted, tether cutting or breakout reconnection, can develop in addition to the initial interchange reconnection. The removal of the outer layer of the emerging fields via external reconnection, called breakout reconnection see Figure 1.9, is one possible mechanism that may lead to the rise of the sheared core and future blowout eruption. Breakout reconnection [Antiochos et al., 1999, Moore and Sterling, 2006, Karpen et al., 2012] may occur with or without the rising core field when the external reconnection point and current sheet forms. Multiple MHD models have been performed to simulate the physics of the reconnection jet in 2D [Heyvaerts et al., 1977, Yokoyama and Shibata, 1996a, Moreno-Insertis et al., 2008], however these models assume an ideal gas, with no radiation cooling, and no heat conduction. In this work we determine if magnetic tension is the primary acceleration mechanism in coronal jets. One way to determine if the release of magnetic tension is driving jet acceleration is to look for observational signatures of reconnection in the jet spire such as the plasmoids, retracting loops, flows, etc. and/or examine the coronal magnetic topology. If the release of magnetic tension is accelerating jet plasma, we also expect plasma at different temperatures to have a similar velocity, since magnetic tension would accelerate plasma of similar density equally.

1.5.0.2 Acceleration Due to Filament Eruptions

Twisting and unwinding motions are commonly seen in jets, particularly in ones with filaments [Liu et al., 2019, Shen et al., 2011a, Chen, 2012, Hong et al., 2013, Schmieder et al., 2013]. These helical motions have been observed to produce counter-clockwise, transverse velocities range from 40 km /s to 200 km/s [Shen et al., 2011a, Lui, 2009, Schmieder et al., 2013] and rotation speeds on the order of $\sim$ 7 minutes [Liu et al., 2009, Chen et al., 2012, Zhu et al., 2016]. and periods are on the order of 4 to 9 min. Transverse velocities are slightly lower than longitudinal velocities along the jet axis. The twisting motions are often explained by the release of accumulated magnetic helicity into the upper solar atmosphere due to the reconnection between a twisted bipole and open fields [Yokoyama and Shibata, 1996a,b]. In these cases, a twisted flux rope is embedded beneath the reconnection site before reconnection occurs. After reconnection, the field lines begin to straighten, accelerating the plasma by the release of magnetic tension referred to as the sling-shot effect. The newly reconnected field line are twisted at one end, and untwisted the other creating magnetic gradient along the open field lines. Plasma along the field line can be accelerated two ways. The untwisting motion could deposit additional energy via torque from the sling-shot effect or non-linear torsional Alfvén waves can propagate along the field lines and can deposit energy by compressing plasma as it propagates. This type of mechanism has been modeled by several authors including [Pariat et al., 2009, Rachmeler et al., 2010, Pariat et al., 2010, 2015a].

[Pariat et al., 2009, 2010] numerically simulated the formation of untwisting active region jets as a result of the continuous pumping of magnetic free energy and helicity into the corona from the photosphere, which is interpreted as upward propagation of torsional Alfvén waves at a speed of hundreds of km/sec. Transverse velocities were also successfully reproduced in numerical simulations of emerging closed field into ambient open field [Yokoyama and Shibata, 1996a]. [Wyper et al., 2019] developed a 3-D MHD simulation of blowout-helical jets near active regions. In those cases they found that these jets can

be formed via the combination of breakout reconnection and kinking of the erupting filament. Their model suggests that multiple mechanisms may be responsible for the eruption of coronal jets. The idea that jets could become unstable via MHD destabilization mechanisms, such as the kink instability [Raouafi et al., 2016] is also supported by observations [Zhu et al., 2017]. [Liu et al., 2019], established a lower limit for the number of twist required before small flux ropes become unstable. They found that coronal jets can reach a kink instability threshold of 1.3 turns. Other observational studies [Liu et al., 2019], also finds fluctuations in the current sheet and filament before the jet eruption. However the role of helicity in jet eruptions, is not firmly established. In active regions, models have been able to successfully model flare eruptions with and without the presence of helicity, suggesting that helicity may not be necessary for an eruption to occur. However these studies also show that helical active regions tend to erupt more frequently and with more energy [Nindos and Andrews, 2004, Nindos, 2009, Georgoulis et al., 2009, Pariat et al., 2015b].

[Wyper et al., 2019] developed a 3-D MHD simulation of jets on the periphery of active regions. These jets tend to be larger and more energetic because of the increased concentration of magnetic flux introduced by the active region. The authors reproduced the helical motion observed in jets by embedding filaments, supporting the idea that helical jets (of a comparable magnitude) are formed through the release of highly twisted filaments. If the acceleration of jet plasma is due to filament eruptions and in-turn torsional Alfvén waves, we expect to observed to presence of a filament and helical motions in jet spires. Furthermore, we except to observe velocities near the Alfvén speed and for plasma of different temperatures to have similar velocities. In this work, we examine the motion of jet inorder to determine if this type of mechanism is at work.

1.5.0.3 Acceleration Due to Chromospheric Evaporation

Chromospheric evaporation is often associated with flaring active regions, when magnetic reconnection in the corona heats and drives chromospheric material upward at veloc-

ities comparable to the local sound speed, set by the plasma temperature [Neupert, 1968, Antiochos and Sturrock, 1978, Acton et al., 1982]. Energy is imparted onto the chromosphere in the form of conduction fronts, accelerated energetic particles, and/or adiabatic compression by magnetic field lines. The pressure in the chromosphere and the corona are very different along the same magnetic field line, therefore the heated chromospheric plasma is then accelerated by the pressure gradient. In those cases, the most discriminating observations are enhanced blue shifts in hot spectroscopic lines and a notable increase in plasma velocity as a function of temperature. In order for chromospheric evaporation to occur the energy released in magnetic reconnection must be large enough to heat the cooler, more dense chromospheric plasma. In active regions, [Fisher et al., 1984, 1985] defined an upper limit to describe the relationship between free magnetic energy and velocity due to chromospheric evaporation. They predicted jet temperature-dependent velocities should remain less than $2.35C_s$, where C_s is the local sound speed. In addition, the velocities should be less than the Alfvén speed, since the temperature-dependent velocity is dominated by the gas pressure rather than the magnetic field tension. [Longcope et al., 2010] extended the work of [Fisher et al., 1984], by using a numerical model that incorporated plasma parameters such as temperature and density. The authors were able to determine a threshold for explosive reconnection to occur, and thus allow chromospheric evaporation to occur. The authors developed an analytic model that describes the kinetic, thermal and non-thermal energies expected for flares, establishing a relationship between thermal energy flux, explosive reconnection and kinetic energy. The threshold for chromospheric evaporation occurs when explosive reconnection occurs, i.e when unit flux per area input into the corona is greater than the energy required to heat dense chromospheric plasma. Large jets often have energies that exceed this threshold, allowing explosive reconnection to occur. Therefore, coronal jets could also exhibit evidence of chromospheric evaporation when magnetic reconnection occurs. In [Matsui et al., 2012], the authors investigated a jet observed by multi-wavelength spectroscopic and imaging observations. [Matsui et al.,

2012] found velocity increased as a function of temperature for an EUV (1MK − 8MK) jet, within the upper limit set by Fisher, $2.35C_s$. The velocity of the cooler plasma, ($\sim$ logT 4.9) showed a enhanced blue shift, and velocity well above the threshold for explosive chromospheric evaporation. The authors concluded that magnetic reconnection was responsible for accelerating the cool component of the jet, while chromospheric evaporation was responsible for accelerating the hot and warm plasma.

2.5 and 2D hydrodynamic models of chromospheric evaporation in active regions predict that chromospheric evaporation is initiated sequentially in overlying loops as the loop footpoints mover further apart, resulting in soft X-ray emission [Yokoyama, 1998, Yokoyama and Shibata, 2001, 1995]. These models also show that the upward motion of the reconnection point and the increasing loop foot point separation. These are parameters that can be compared to observations as discussed in Chapter 5. However, few existing numerical studies include thermal conduction, which is necessary for producing the evaporation. Since the flow velocity is dependent upon pressure, and therefore temperature, a straight forward way to determine if chromospheric reconnection plays a role in the acceleration of jet plasma is to look for a correlation between temperature and velocity. In this study, we use a novel technique to investigate the acceleration mechanism in six coronal jets by examining their temperature as a function of velocity as discussed in Chapter 2.

1.6 Summary and Motivation

Coronal jets are energetic eruptions, identified by a culminated spire, bright loop base, multi-thermal ejecta, and notable changes in underlying magnetic flux including magnetic emergence, cancellation, or the close motion of opposite polarity bipoles [Shibata et al., 1992b, Shimojo et al., 1996, 1998]. Coronal jets observed using EUV and X-ray instruments have been found to have velocities have been found to have velocities from 100 -800 km/s, spire lengths up to $3R_s$, and occur frequently making them candidates for depositing mass and energy into the solar wind [Shibata et al., 1992b,c, Savcheva et al., 2007,

Cirtain et al., 2007, Filippov et al., 2015, Moreno-Insertis et al., 2008] X-ray and EUV jet are often loosely grouped by morphological features as either *standard*; having a narrow spire, or *blowout*; having a broad spire and accompanying filament eruption [Shibata et al., 1992c, Moore et al., 2010]. Although jets have been observed for decades, a consensus on their formation and the acceleration in their plasma spires has not been found. Magnetic reconnection is widely accepted to be responsible for jets, however the process is complex. Understanding the underling magnetic field and topology is necessary for understanding jet formation, however few models explore the effect of different initiation mechanisms or perform magnetic field extrapolations to determine the 3D magnetic field structure. Of these studies, the results have been contradictory. [Young and Muglach, 2014a,b] report converging motions and flux cancellation in the magnetograms at the base of the jet while [Liu et al., 2011] demonstrated the emergence of flux associated with a blowout jet. Furthermore, most of these models rely on a magnetic flux cancellation as the photospheric driver, when recent studies show that magnetic cancellation is often observed, and may account for most jets [Sterling et al., 2019, Podgorny and Podgorny, 2020, Panesar et al., 2016].

The variety of jet initiators and properties make the ability to determine the formation process difficult. This is further complicated by the wide range of jet plasma parameters, topological features, and the environments in which they are embedded. Furthermore, once the jet is initiated, the plasma can be additionally heated and accelerated by secondary mechanisms throughout the transition region and corona. Three mechanisms have been proposed, the acceleration due to magnetic tension, the energy enhancements associated with a twisted-erupting flux rope, and the secondary effect of chromospheric evaporation driven by a pressure gradient. MHD models of these mechanisms produce predictions that can be compared to observations. First, the magnetic tension model predicts plasma velocities near the local Alfvén speed, since the acceleration is caused by the release of magnetic field, similar to standard jets [Yokoyama and Shibata, 1995, Miyagoshi and Yokoyama,

2003]. Erupting filament models, predict a break-out reconnection topology and plasma velocities that are similar across temperature. Finally, since the flow velocity in the evaporation model is dependent upon pressure, and therefore temperature, a straight forward way to determine if chromospheric reconnection plays a role in the acceleration of jet plasma is to look for a correlation between temperature and velocity as applied in [Matsui et al., 2012]. The topology of blow-out and standard jets can also be examined by determining if reconnection occurs externally only (standard jet) or both internally and externally (blowout jet). It is possible that all effects play a role during the formation and acceleration of a jet, with different relative importance, and/or during the different phases of the jet. The specific contribution from the three mechanisms may also depend on the type of jet and specific magnetic configuration and its evolution. What is needed is thorough investigation of coronal jets through both observations and analysis of the magnetic topology, on a case-by-case basis to determine which mechanisms are, or are not, contributing to jet formation.

The aim of body of work is to examine acceleration mechanisms and magnetic topological evolution of in coronal jets using a 2-step approach. First we use a novel technique to investigate the acceleration mechanism in six coronal jets by examining their temperature as a function of velocity. Using observations from Hinode's X-ray Telescope (XRT), Solar Dynamics Observatory's Atmospheric Imaging Array (SDO-AIA), and Interface Region Imaging Spectrograph (IRIS), we capture the plane of sky velocities along the jet spire. When available, we use IRIS spectroscopic observations of Si IV line profiles to calculate Doppler velocities and non-thermal line broadening. We construct differential emission measures (DEMs) as a proxy for temperature, and determine if the jets show evidence for chromospheric evaporation. We look for evidence of twist and/or erupting filaments by constructing time-distance plots perpendicular to the jet spire.

To investigate the magnetic evolution of the coronal jet, we use the NLFFF, with the flux insertion method using the Coronal Modeling System, NLFFF implementation software

[van Ballegooijen, 2004]. Using the 3D magnetic field topology, we locate the null, or quasi-seperatrix regions that are most likely to be the site of magnetic reconnection and particle acceleration. We use the evolution of the field to determine which locations are most relevant to the erupt, thus eliminating potential jet models. The results of this analysis will access the predictions of these competing jet models and examine the possibility that multiple acceleration mechanism can be present in jet formation.

Chapter 2 discusses the analysis methods including calculation of temperature, velocity and emission measure, as well as the NLFFF model setup and extrapolation procedures. In Chapter 3, I discuss the observations of six coronal jets, their coronal and magnetic evolution, and the appearance of helical motions in their spire. In Chapter 4, I present the results of our observational analysis. Chapter 5, discusses the results of the topological models for a subset of jets. Finally, Chapter 6 summarizes these results, interpretation and future work.

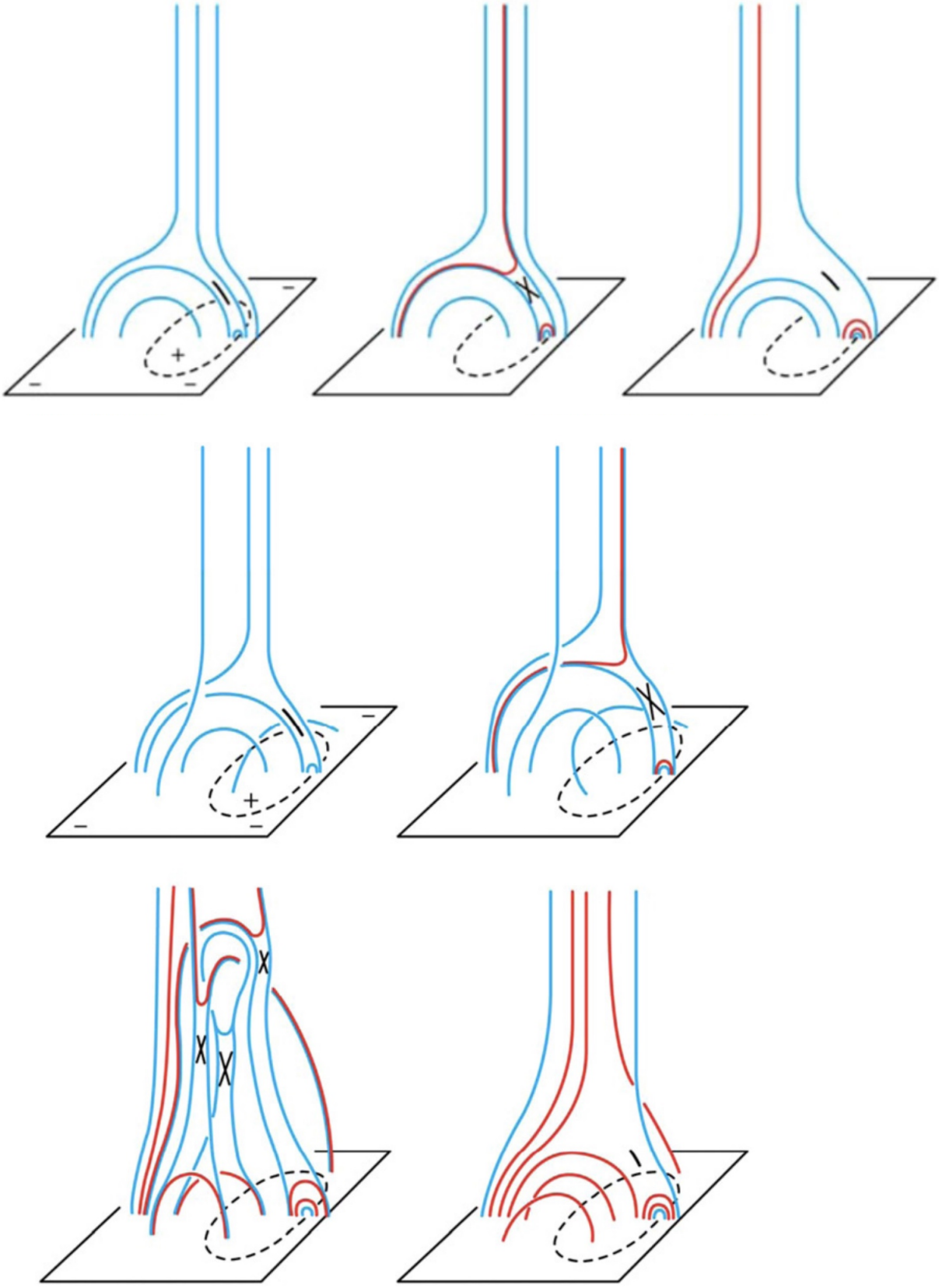

Figure 1.9: Top: Standard Jet Model Schematic: The ambient, open, magnetic field lines reconnect with the closed field of the emerging flux elements. Bottom: Blowout Jet Schematic: Blowout jets are thought to form as a result of both internal and external reconnection. Figures from [Moore et al., 2010]

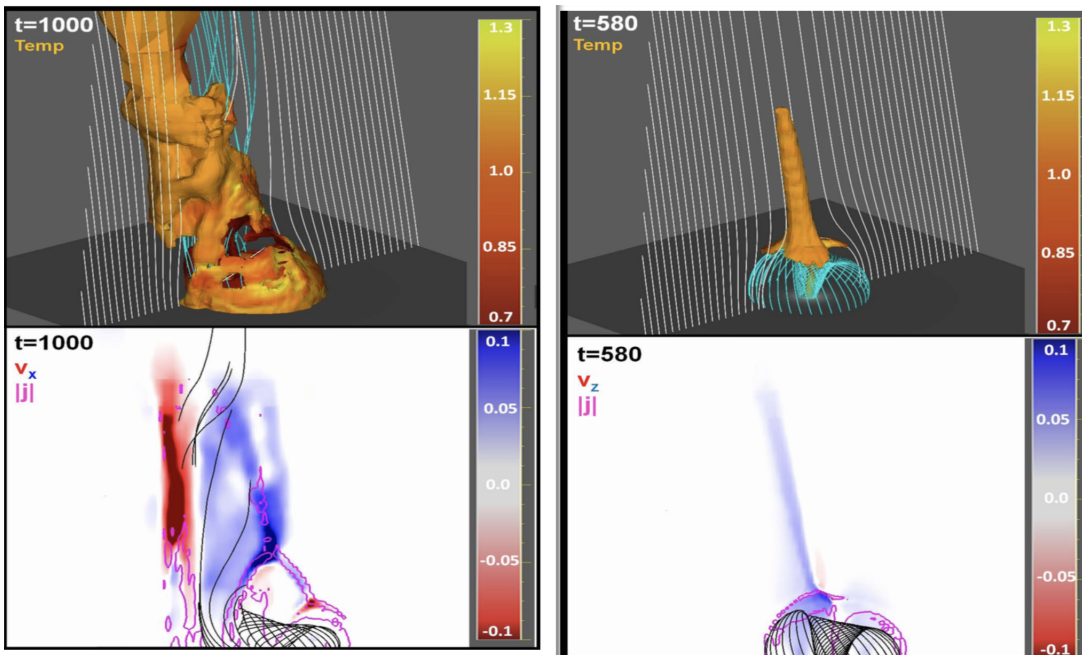

Figure 1.10: Figures from [Pariat et al., 2015a]. 2.5D models predict jets can be accelerated via torsional Alfvén waves that propagate due to twist in the magnetic field (left) and/or gas pressure driven, chromospheric evaporation(right). Model of the untwisting jet predict Doppler shifted velocities, and velocities approaching the Alfvén speed. Models of the evaporation jet predict temperature-dependent velocities less than 2.5 time local sound speed,Cs, with or without twisted flux rope.

Chapter 2

Methodology

The aim of this research is to examine possible acceleration mechanisms in coronal jets using a combination of multi-wavelength observations and magnetic topological modeling. In this chapter, I describe the analysis methods and instruments used to investigate the acceleration mechanisms in six coronal jets. In Section 1, I describe a novel approach to investigate chromospheric evaporation. In section 2, I describe the Coronal Modeling System (CMS) and the Flux Insertion Method.

2.1 Examining Chromospheric Evaporation in Jets

To determine if jets show evidence of chromospheric evaporation, we calculate the plane of sky velocity as a function of temperature for each of the jets. Using observations from Hinode's X-ray Telescope (XRT), Solar Dynamics Observatory's Atmospheric Imaging Array (SDO-AIA), and the Interface Region Imaging Spectrograph (IRIS), we capture the plane of sky velocities along the jet spire. When available, we use IRIS spectroscopic observations of Si IV line profiles to calculate Doppler velocities and non-thermal line broadening. We construct differential emission measures (DEMs) as a proxy for temperature, and determine if the jets show evidence of temperature-dependent velocity, indicating chromospheric evaporation. Below I describe the instruments used in this analysis.

2.1.1 Instrumentation and Data Reduction

2.1.1.1 SDO's Atmospheric Imaging Array (AIA)

Solar Dynamics Observatory's [Pesnell et al., 2012], Atmospheric Imaging Array [Lemen et al., 2011, Boerner et al., 2012] provides continuous observations of the full solar disk

with 0.6 arcsec per pixel resolution. AIA is capable of imaging each channel at a 12 second cadence with a 4096×4096 pixel CCD [Boerner et al., 2012]. Each CCD is divided into four 2048x2048 quadrants, with 16-megapixel charge couple devices (CCDs), which are read out separately and simultaneously at a 2 Mpix/sec rate. In this study we use six AIA channels, sensitive to coronal temperatures from $\sim$ logT 5.5 to 7.0 K (10^5 K to 10^7 K). The AIA 304Å channel was not included in DEM calculations because it images optically thick plasma, while DEM analysis requires optically thin emission. We process each of the SDO images using standard routines found in the SolarSoft software library [Handy et al., 1999], such as aia_prep.pro, which removes bad pixels, corrects CCD vignetting and flat−fielding, normalizes images by the exposure time and ensures each of the images are aligned channel [Freeland and Handy, 1998]. Typically SDO-AIA images are aligned at on sub-pixel level, however in some cases, some images were manually shifted to ensure sub-pixel alignment. Once we confirm alignment, we use the six channels along with the Fe XVIII component of the 94Å channel to calculate the plane of sky velocity and the differential emission measure (see section 3.2.1).

Each AIA EUV channel is dominated by emission from Fe ions, and the channels are centered around the following wavelengths: 94 Å (Fe X, Fe XIV, Fe XVIII), 131 Å (Fe VIII, Fe XXI), 171 Å (Fe IX), 193 Å (Fe XII, Ca XVII, Fe XXIV), 211 Å (Fe XIV), and 335 Å (Fe XVI) [O'Dwyer et al., 2010], which are sensitive to temperatures from .5MK−8 MK,[Del Zanna et al., 2015]. In Table 2.1.1.1 , we list the Fe ionization states that dominate each channel, the corresponding temperature plasma, and field of view for each instrument used in this analysis. Figure 2.1 shows an AIA image in each wavelength and the corresponding peak temperature.

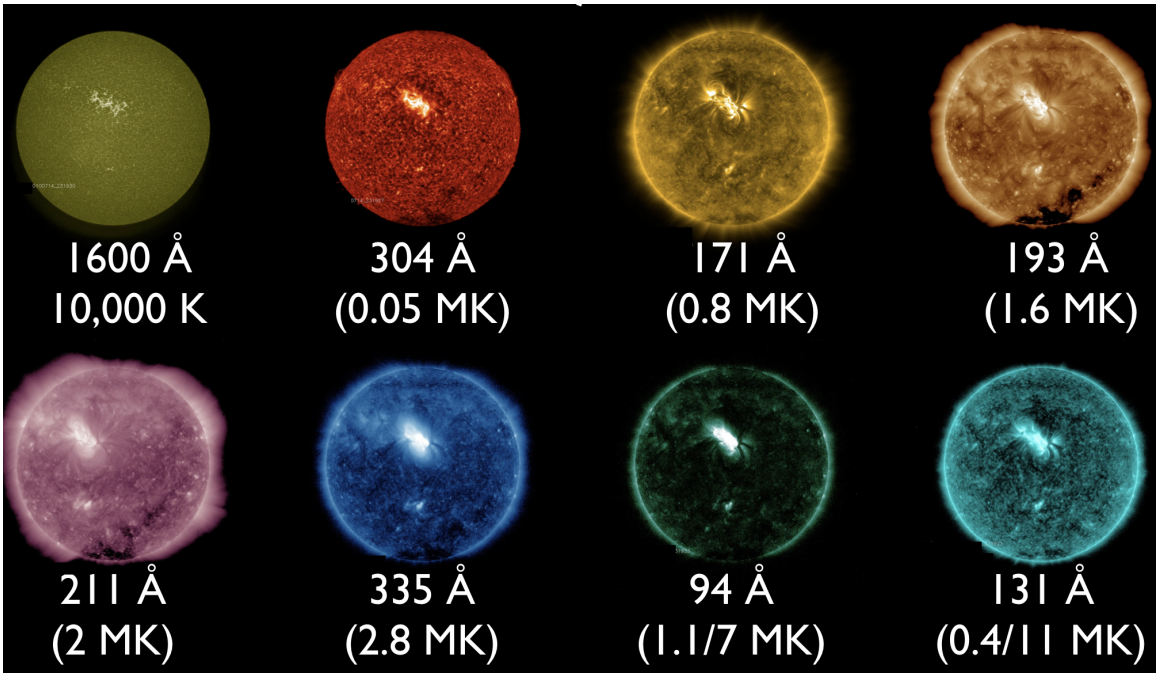

Figure 2.1: SDO/AIA channels and corresponding peak temperature from temperature response function observed in each channel. Figure courtesy of K.Reeves.

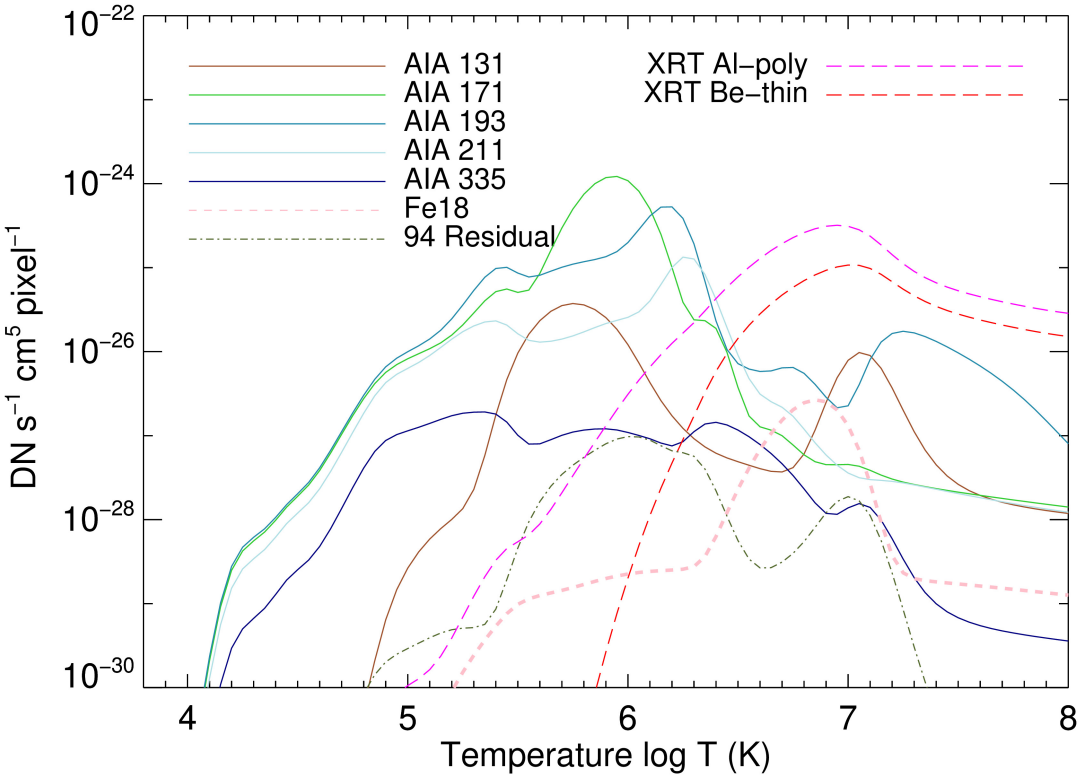

Figure 2.2: Temperature response functions of AIA and XRT channels.

Table 2.1: Summary of Instrument Specifications

Instrument/Channel	**Dominate ions**	**Temperature Sensitivity(logT)**	**Spatial Resolution**	**Region**
AIA/94Å	Fe X, Fe XIV, Fe XVIII	5.9− 6.8	0.6”	corona
AIA/131Å	Fe VIII, Fe XXI	5.6 − 7.0	0.6”	TR , flare
AIA/171Å	Fe IX	5.8-6.0	0.6”	QS,upper TR
AIA/193Å	Fe XII, Fe XXIV, Ca XVII	6.2, 7.3	0.6”	corona
AIA/211Å	Fe XIV	6.3	0.6”	AR corona
AIA/335Å	Fe XVI	6.4	0.6”	AR corona
AIA/304Å	He II	4.7	0.6”	chromosphere
XRT/Al-poly	Fe XVIII,NeIX,OVIII	6.6,6.2,6.4	1.0”	AR, QS
XRT/Be-thin	Fe XVII,MgXI,NeIX	6.6,6.5,6.2	1.0”	AR,flare
IRIS/SJI 1400Å	Si IV	3.7−5.2	0.166”	chromosphere, TR
IRIS/SJI 1330Å	CII	3.77−7.0	0.166”	chromosphere, TR
IRIS/SG 1331.56−1358.40Å	CII,Si IV,Mg	3.7−7.0	0.33” x 175”	chromosphere, TR
IRIS/SG 1390−1406.79Å	Si IV,Mg,CII	6.0−6.2	0.33” x 175”	chromosphere, TR

Instruments used in this study, primary ions, and corresponding temperature sensitivity [Lemen et al., 2011, O´Dwyer, B. et al., 2014, Wülser et al., 2018].

2.1.1.2 Separation of Fe XVIII component of 94Å channel

The AIA 94Å channel is sensitive to temperatures from logT 5.5- logT 7.0 [Boerner et al., 2012], with response peaks at logT 6.0 and logT 7.0. Figure 2.2 shows the temperature response functions of AIA and XRT channels. In order to calculate the velocity of the only the hot emission, dominated by the Fe XVIII line, see Table 2.1.1.1, we separate the Fe XVIII component of the AIA 94Å channel line from the remaining emission using the method of [Warren et al., 2012]. This method has been applied to active region loops and coronal jets. The relevance in this case is to determine if the emission in Fe XVIII, has a higher velocity than the velocity of the cooler component. We perform this step for all of the jets in this study. The AIA 131Å temperature response is also peaked at both a cool and hot temperature, but there is currently not a way to separate the hot and cool components in observational data.

2.1.1.3 SDO-Helioseismic and Magnetic Imager (HMI)

The Helioseismic and Magnetic Imager [Scherrer et al., 2012] onboard SDO, provides line-of-sight magnetograms at a 12 second cadence. We use LOS magnetograms to examine the underlying magnetic field of each of the jets and determine if the jet formed as a result of flux cancellation, emergence, proximity to an opposite polarity flux element, and/or a combination of effects. From the magnetograms we determine if the underlying magnetic flux is associated with emerging flux, canceling flux, a combination of both or neither. A full disk magnetogram and an AIA 193 Å image for one of the jets in this study are shown in Figure 2.3.

2.1.1.4 Hinode/X-ray Telescope (XRT)

The X-ray Telescope (XRT) [Golub et al., 2007] onboard HINODE [Kosugi et al., 2007] is a grazing incidence X-ray imager, equipped with a 2048$\times$2048 CCD with 1.0286 arcsec pixel resolution in eight X-ray channels, with a broad-band response between 1 and 200

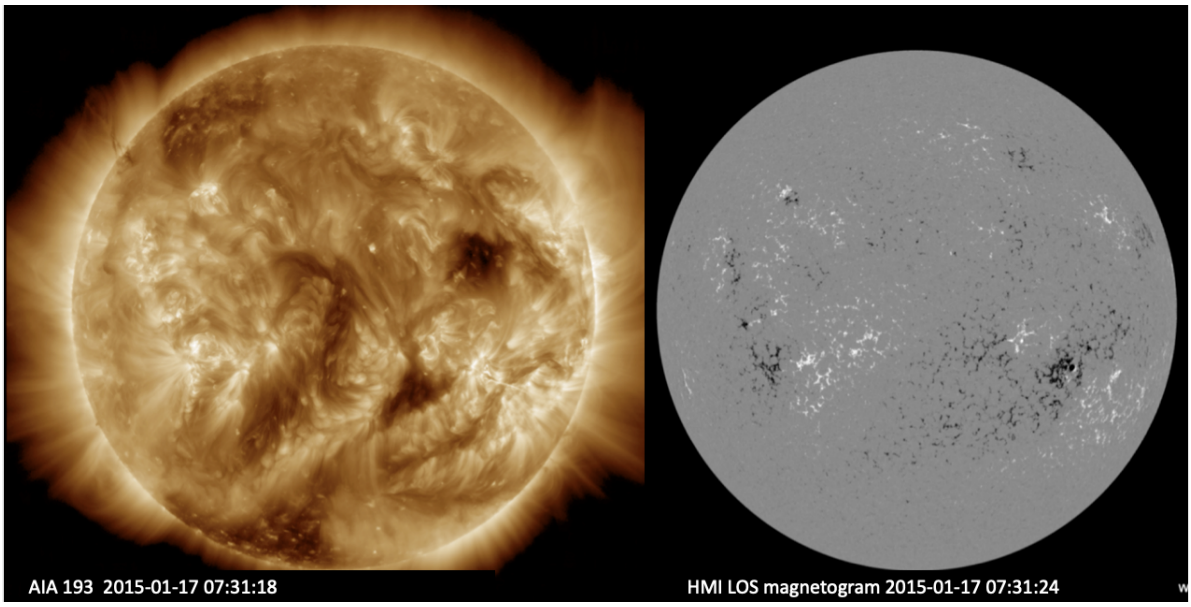

Figure 2.3: AIA 193Å and corresponding HMI line-of-sight (LOS) magnetogram.

Å. The cadence of XRT observations can vary depending on the observing program and interruptions from satellite safety operations. The XRT images were processed using the standard software `xrtprep.pro`, which removes high frequency noise, normalizes by the exposure time, and corrects for vignetting [Kobelski et al., 2014] and we use temperature response functions according to the calibration of [Narukage et al., 2011, 2014]. When available we use Aluminum-poly (Al-poly) and Thin-Beryllium (Be-thin) channels, which are sensitive to temperatures greater than 2MK, to calculate plane of sky velocity and the derive the differential emission measures.

2.1.1.5 Interface Region Imaging Spectrometer (IRIS)

The Interface Region Imaging Spectrometer [De Pontieu et al., 2014] is equipped with both a slit-jaw imager and a spectrometer, that are sensitive to plasma in the far and near UV. The IRIS Slit Jaw Imager provides spectra in four different pass-bands (C II 1330 $+-$ 1.0, Si IV 1400$+-$ 1.0, Mg II k 2796$+-$1.0, and Mg II wing 2830 Å) with up to a two second cadence and 0.33 arc-sec resolution. We use slit-jaw images from the 1330Å and 1400Å channels, when available, to calculate the line of sight velocity of two jets analyzed

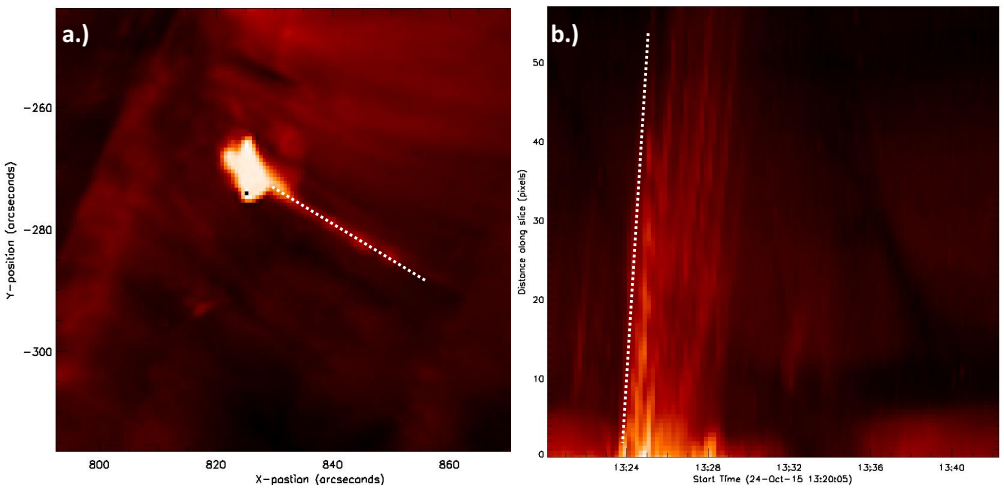

Figure 2.4: Example of the plane of sky velocity. Left:We select points along the spire of the jet. This artificial 'slit' is taken for each time-step, creating the stack-plot. Right: The velocity is determined by fitting a line to the leading edge of emission in the stack-plot (white line)

in this study. We use level 2 data which has been dark corrected, flat-fielded, de-spiked, re-oriented and geometric and wavelength calibrated. One of the jets has high cadence raster observations in at the full spectral resolution (26 mÅ).

2.1.2 Calculating Plane of Sky Velocity

To calculate the plane of sky velocity we create stack-plots (time-distance plots) of intensity verses time for an artificial slice along the spire of the jet similar to methods used in [Savcheva et al., 2007] and [Mulay et al., 2017]. We select the jet spire, above the base, to the end of the jet. We interpolate 100 points in between the two endpoints, creating a line of 100 segments. We determine the intensity along the slice, for each of the images in the data cube, and create a intensity stack plot. We can then select the line of sight velocity by fitting a straight line to stackplot. The final velocity is the slope of the line. We show an example of this process in Figure 2.4. In cases where the spire of a jet is broad, such as blow-out jets, we select several lines along the direction of motion and add all of the lines to determine the average bulk velocity. The spire of some jets, are curved and not easily

approximated using straight line. For these jets, we select 15 points along the jet spire and interpolate the along the spire using a 2 dimensional fit. We then calculate the distance along the spire at each increment and create a time-distance plot using the intensity versus distance. We repeat this process with XRT Al-poly and Be-thin, and IRIS 1330 and 1400Å images when data is available. To calculate the error we simply choose 3 lines within the pixels along the brightest portion of the jet an calculate the standard deviation of the three values.

2.1.3 Differential Emission Measure and Emission Measure Weighted Temperature

Both AIA and XRT are broad band channels, i.e the temperature response function is sensitive to a range of temperatures, see Figure 2.2, thus we can employ a differential emission measure method to determine plasma temperature. A DEM represents the distribution of plasma, along a line of sight, as a function of temperature; assuming the emission in optically thin and in thermodynamic and ionization equilibrium. The DEM uses a linear combination of the temperature responses convolved with the observed intensity to determine the amount of plasma of a given temperature along the line of sight. The DEM is a set of functions that satisfy the equation:

$$Ii(x) = \int DEM(T,x)Gi(T)dT(cm^5K^-1) \tag{2.1}$$

where Ii is the measured intensity for a given channel, and G is the 'gaunt factor' or contribution factor calculated from the temperature response function for each of the filters and the instrument response(sensitivity). The gaunt factor folds solar elemental abundances and given plasma temperature and density, and calculates how material at a given temperature emits radiation, i.e. solar emissivity. Atomic abundance information for the instrument response was calculated using Chianti atomic database, version 8.0.7 [Del Zanna et al., 2015, Dere et al., 2019]. The most recent version is 9.0 [Dere et al., 2019].

Figure 2.2 shows the temperature response functions of the EUV channels of AIA, i.e the sensitivity of each channel to plasma at a given temperature. We use the DEM solver package, xrt_dem_iterative2, available in SolarSoft [Weber et al., 2004] to calculate DEM along the spire, similar to work by [Weber et al., 2004, Schmelz et al., 2009a, 2010, Winebarger et al., 2011] for active region loops. Here we provide a brief summary of the DEM algorithm. For more details see [Weber et al., 2004, Golub et al., 2004, Cheng et al., 2012]. The routine calculates the DEM by guessing an initial DEM (creating a synthetic DEM), folding it throughout the temperature response functions of each of the observed channels to generate predicted emission. The calculated fluxes are compared to the observed fluxes and the goodness of fit (χ^2) is calculated. This process is repeated to minimize χ^2 using mpfit, a routine that preforms a Levenberg-Marquardt least squares minimization. In each iteration the observed fluxes are varied within the observational error, and the new DEM is used as input for the next iteration. The program uses Monte Carlo iterations over the range of the observational error to calculate the variation in the DEM. The range of solutions are shown in blue in Figure 2.5.

The xrt_dem_interative2.pro software package requires user input for the XRT and AIA temperature response functions. XRT filter responses were calculated using the XRT standard SolarSoft software (make_xrt_temp_resp) and elemental abundances from the Chianti database [Del Zanna et al., 2015, Dere et al., 2019]. The AIA temperature response functions were calculated using aia_get_response.pro. These routines account for the time-dependent contamination of the XRT and AIA CCD. By imputing the date, the program calculates estimated degradation of XRT (see [Narukage et al., 2011, Urayama et al., 2008]) and AIA ([Boerner et al., 2014]). We calculate the response function of the Fe XVIII component of AIA 94 Å as described in Section 2.1.1.2. We then subtract the Fe XVIII component from the original temperature response, to capture the cool or residual response function that we will call 94c. Calculating the DEM is not without challenges. The DEM solutions derived from xrt_dem_interative2.pro are not well constrained in high temper-

atures (>7.5 MK), because AIA is not sensitive to those temperatures. In those cases DEMs may overestimate the amount of high temperature plasma [Schmelz et al., 2009b, Winebarger et al., 2011]. Here when possible, we use additional data from Hinode-XRT to constrain the DEM.

Once the DEM is calculated, other parameters can be estimated, such as plasma density, thermal X-ray flux, thermal energy, and emission measure (EM)-weighted temperatures. Here we describe the calculation of emission measure weighted temperature, commonly used as a proxy for density.

Integrating DEM over a particular range of temperatures, produces the emission measure,which is used as a proxy for density:

$$EM = \int DEM(T)dT \tag{2.2}$$

and emission measure weighted average temperature:

$$T = \int_T DEM(T)TdT/EM \tag{2.3}$$

If we assume the filling factor of 1, we can derive density as $n = \sqrt{\frac{EM}{h}}$, where h is the depth of the column of plasma along the line of sight.

2.1.3.1 Error Calculation of Intensity

To calculate the error in intensity for each of the channels we use the method of [Gehrels et al., 1986]. The $\sqrt{DN}$ is commonly used to calculate the error in intensity [Weber et al., 2004, Schmelz et al., 2009a, 2010, Winebarger et al., 2011], but in this case several channels contained faint emission, only a small percentage higher than the background emission. Thus we use the following equation to calculate error in intensity.

$$\sigma DN = 1 + \sqrt{DN_i + 0.75} \tag{2.4}$$

This equation approximates the Poisson statistics for low counts but converges to $\sqrt{DN}$ for high counts. We apply this method to the six AIA channels including the modified Fe XVIII and 94c from 94Å channel and XRT data when available.

2.1.3.2 Assigning Temperature per Channel

Using the temperature response function, emission, and DEM we can determine the distribution of temperatures, in each channel, and determine which temperature is primarily contributing to the observed emission in each channel. Figure 2.5-Figure 2.8, show examples of this process. Figure 2.5 shows the DEM for Jet 1, observed 2015-10-24. The DEM solution (black solid line) peaks near logT 5.5 and 6.5. The blue lines are Monte Carlo iterations within the boundaries of the input error as discussed in Section 2.1.3. Using the temperature response function for each filter, we can determine the contribution of each temperature bin, to the total intensity. Figure 2.6 , shows percentage contributed to emission in AIA channels 131, 211,171 Å respectively. We indicate the contribution factor (percentage each temperature bin contributes to the total) by the density of vertical tick-marks, similar to a rugplot, shown at the bottom of the plots. In this example, for Jet 1, we find the highest percentage in the 131Å channel is near temperature of $\sim$ logT 5.4, therefore there is a high density of tickmarks near logT 5.4. We refer to the temperature bin with the highest percent, as Tprime. In this case, for channel 131Å Tprime is logT 5.4. There are four cases for which Tprime is ambiguous, two caused by the distribution of the temperature response function, and 2 caused by the calculated distribution of temperatures. Case(1): The temperature response for 131Å channels, is peaked near both cool and hot temperatures. See Figure 2.2. Therefore, for some jets, the contribution distribution in the 131Å channel is bi-modal because of this effect. Case(2): The temperature response function is broad i.e. the channels is equally sensitive to a wide range of temperatures. In this example, AIA 335Å is not dominated strongly by one particular temperature. Thus when emission is folded into the temperature response function, we often get a broad range of

temperatures for Tprime. In these cases Tprime is taken with caution. Case (3): In some channels, the jet emission is dominated equally by a cool and warm components, such as 211Å channel in Figure 2.7. This situation would result in a concentration of tickmarks near both temperatures, therefore it is difficult to select Tprime. Case(4): The percent contribution is distributed across temperature. For example, contribution percentage the 171Å channel in Figure 2.8 is distributed across many temperatures, even though the temperature response function of 171Å is strongly peaked near LogT $= 6.0$. In each of these cases, we examine the effect of these possible temperatures on our interpretation. To select Tprime we consider the jet observations. If the jet has both a fast moving hot component and a slow moving cool component, these components would overlap in a stack-plot used to calculate POS velocity. It would be difficult to spatially separate the slow moving component. Therefore, we are most likely calculating the velocity of the fast moving component. In these cases, we select the hotter component of Tprime, since it most likely represents the temperature of the plasma for which we have measured a velocity. Using this method, we can determine the velocity in each channel and determine primary contributing temperature bin, thus measuring the velocity as a function of temperature using imaging data. We discuss the results of this analysis in Section 3.2.1.

2.1.4 Intensity, Doppler Velocity and Non-Thermal Line Broadening

Spectral lines can broaden, increase in width in excess of the full-width-half-max (FWHM) of the theoretical line, because of instrumental effects, chaotic motions along the line of sight, or multi-thermal plasma along the line of sight. The analysis of spectroscopic line profiles can provide information on the distribution of electron temperatures, the direction of motion and flow velocities, and measure of turbulent motion or turbulent (small scale/unresolved) flows moving in multiple directions. The presence of multi-thermal plasma along the line of sight could also lead to line broadening, so the DEM is used determine if it is isothermal. IRIS does not have an absolute wavelength because there is not no calibra-

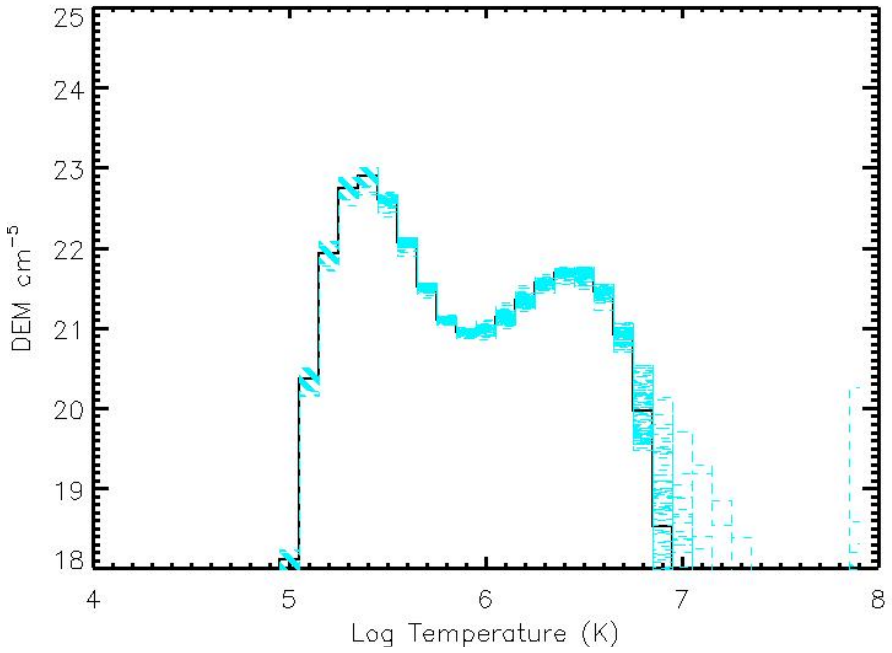

Figure 2.5: DEM of Jet1 Observed 2015-10-24

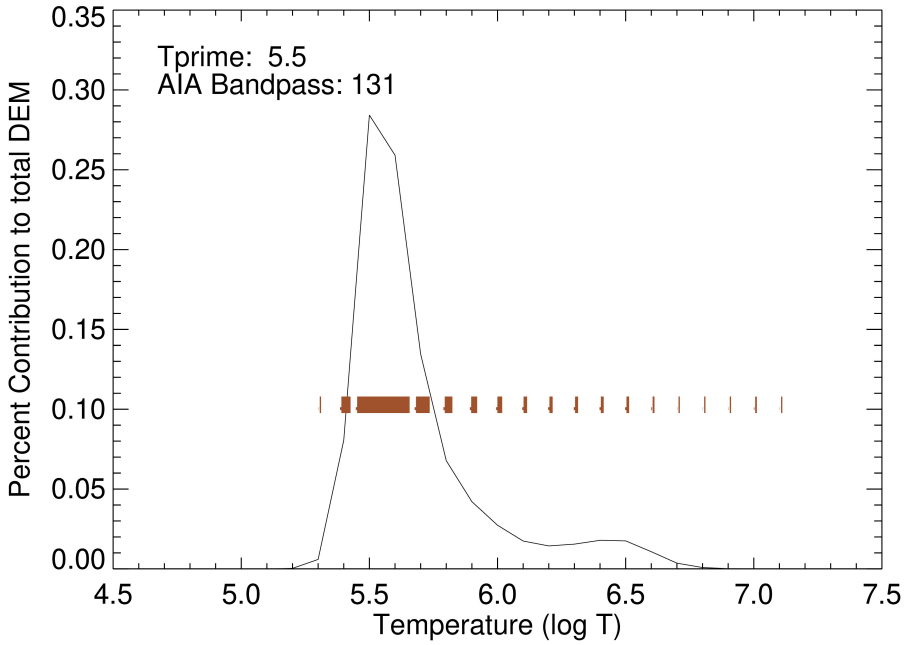

Figure 2.6: AIA131Å Percent Contribution to Total DEM

tion lamp on−board (See IRIS technical notes 20). We use level 2 data with corrected vignetting and calibrate the data using the standard solarsoft IRIS autofit routines. We take and additional step to calibrate the rest wavelength of the Si IV line by averaging over a

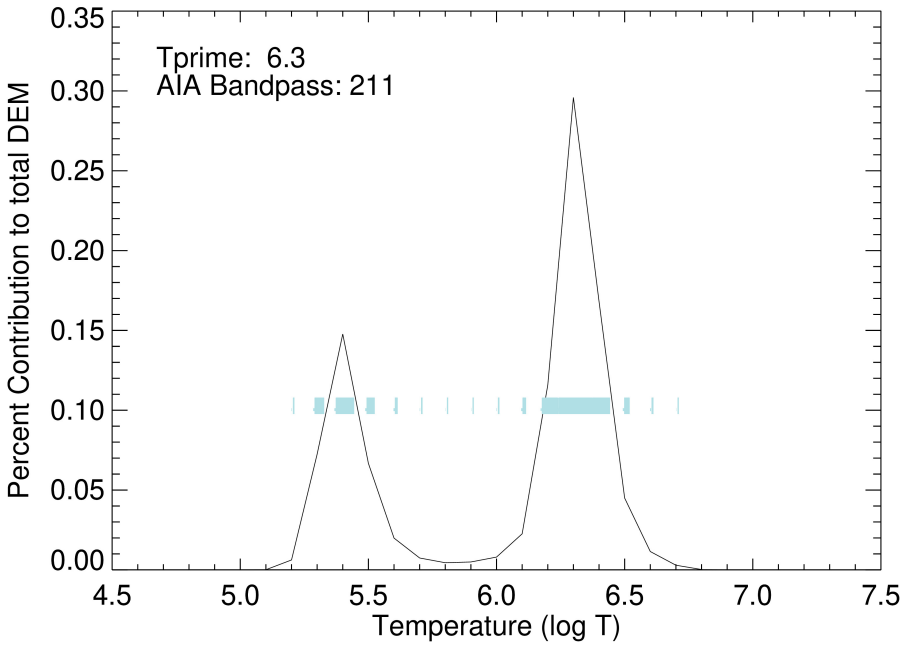

Figure 2.7: AIA211Å Percent Contribution to Total DEM

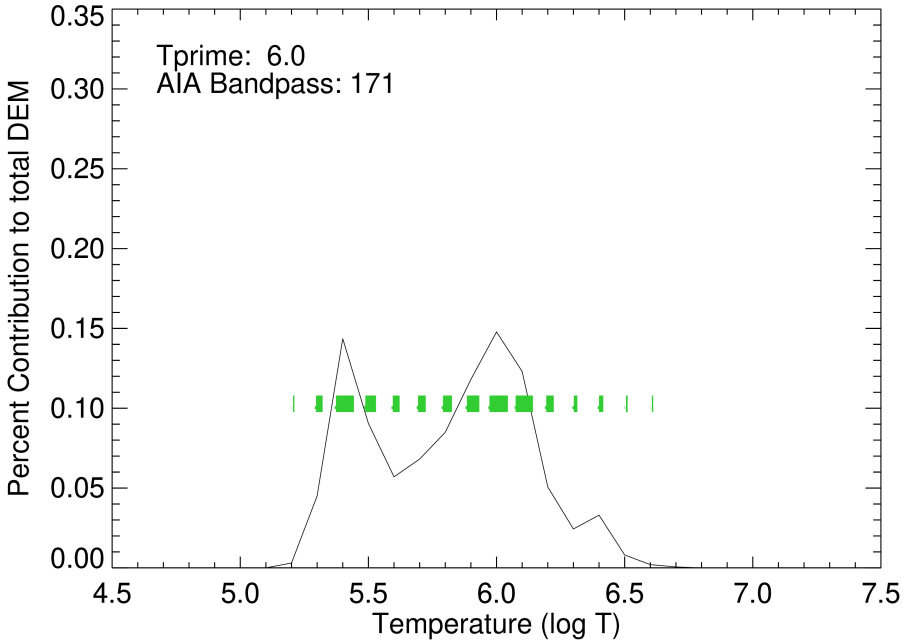

Figure 2.8: AIA171Å Percent Contribution to Total DEM

Figure 2.9: Example calculation of Tprime for Jet: The temperatures contributing the minimum, median and maximum emission.

quiet region along and across the raster.

2.2 Examining Rotation in Jets

Jets have often been found to be accompanied by small filament eruptions [Sterling et al., 2015, Savcheva et al., 2007, Sterling et al., 2018]. However, it is unclear if the eruption of the filament initiates the jet via internal tether-cutting reconnection, or if the eruption of the jet allows the filament to escape along the newly opened magnetic field lines after external reconnection has occurred. Blowout jets have been explained as the result of a strongly sheared field, and filament undergoing tether-cutting reconnection, releasing a twisted filed and flux rope into the corona. In the tether-cutting scenario, if a filament eruption initiates jet eruption, we expect to see evidence of the twisted filament and/or helical motion of the field erupt with jet as has been shown by 3D MHD models [Pariat et al., 2015b, Wyper et al., 2019, Iijima and Yokoyama, 2017] and observations [Mulay et al., 2017, Filippov et al., 2015, Joshi et al., 2018]. Some studies have also shown that kink instability could play a role in the eruption of the inner filament. In this section we investigate if there is a presence of a filament, and if the resulting jet exhibits any helical motion. If helical motion is present, torsional Alfvén waves could also be contributing to the acceleration of jet plasma [Pariat et al., 2015b]. The amount of twist present in the filament to determine if twist and resulting torsional Alfvén waves could contribute to jet acceleration. Ideally, we would use stereoscopic data which allow us to view the jet from multiple angles. However for the purpose of this research, identifying twist through line-of-sight images is sufficient. The aim is only to note the presence of helical motion and/or a filament that could be contributing to the acceleration of the jet. We use the lack of twist to eliminate potential acceleration mechanisms. i.e. if helical motion is present then there is a possibility that the jet plasma is accelerated by internal reconnection and consequently torsional Alfvén waves. If no evidence of twist is present, then we conclude that the jet is not being accelerated by torsional Alfvén waves induced by a twisted field and internal

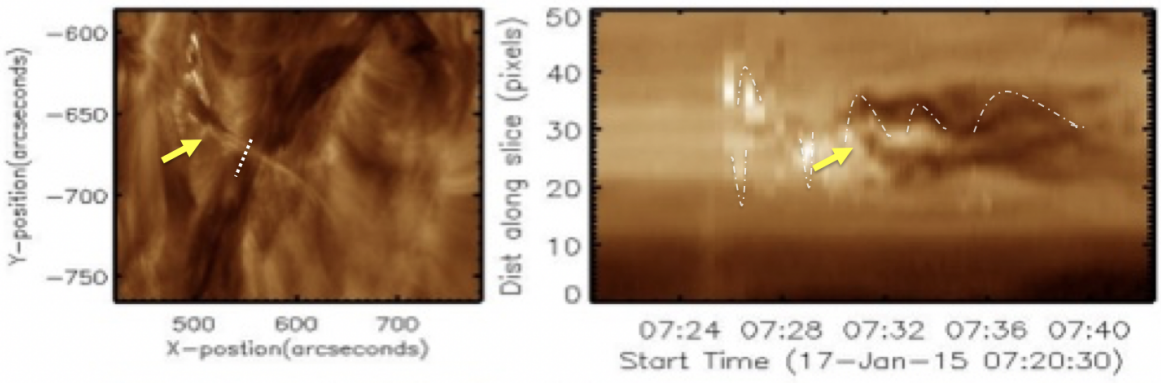

Figure 2.10: Left: SDO/AIA 193Å image of jet observed 2015-01-17 at 07:32:42 UT. White line indicates a vertical cut that was taken to make the distance-time plots on right.

tether-cutting reconnection. Since an erupting filament is often associated with twisted jets, we expect to find evidence of twist and evidence of an erupting filament, within the same jets. To observe helical motion, we create a time-distance plots of each of the jets in this study using AIA 193Å images. Figure 2.10 shows the result of this analysis. The images on the right show the location of the vertical slice used to generate the images on the right. The slices are taken perpendicular to the longitudinal motion of spire, shown by the dotted white line in the images in the left panel.

The white line in Figure 2.10, shows the orientation of the slice. When filaments are present, they appear as dark regions in the spire and are noted by yellow arrows. Helical motions are highlighted by curved or diagonal, white-dotted lines. The presence of helical motion perpendicular to the longitudinal motion of spire appears as repeating diagonal or sinusoidal motions in time-distance plots (depending on the number of twists). If both the upward and downward motion is captured, the time-distance plots will show symmetric inclinations and declination. We note that coronal dimmings can also appear as dark regions in EUV, and have been observed in jets[Lee et al., 2013]. However, dimming are associated with the evacuation of plasma near the jet base and/or along coronal loops, not along the spire, therefore EUV images are appropriate for this study. Filaments can be seen erupting within the jet spire and/or entangled with the spire eruption. If there is not twist, but there is

evidence of a filament, we expect that the eruption of the filament is is not directly related to the acceleration of the jet spire.

2.3 Determining the Likely Sites of Reconnection

Coronal eruptions are driven by the magnetic reconnection in the coronal magnetic field. Since the corona field is not observable, often magnetic field extrapolations based on photospheric magnetic field are used. These extrapolations can then be examined to investigate the evolution of the coronal field, commonly referred to as magnetic topological analysis. Topological changes in the magnetic field are very useful in determining where and how the corona evolves. The combination of MHD simulations and magnetic field extrapolations of active regions have established that the primary regions where reconnection is most likely to occur are also associated with the regions most likely contain a current sheet and/or regions of enhanced current density Demoulin et al. [1993, 1994], Priest et al. [1989], magnetic null points. In 3D, null regions manifest as seperatrix surfaces, quasi-seperatrix layers (QSL), and separator field lines Priest et al. [1989]. Each of these regions separate the field into different connectivity domains with the magnetic field vanishing at the intersection, i.e magnetic field lines across seperatrix surfaces are discontinuous, in turn creating regions of enhanced current density and current sheets. Thus, the severity of this change is a measure of the strength of QSLs. In the sections below, we discuss how NLFFF models and QSL visualization tools can be applied to coronal jets to understand topological changes during the eruption.

2.3.1 Role of Non-linear Force Free Topological Models

Deriving the strength and direction of the 3D magnetic field of the corona is essential for identifying the location of magnetic reconnection and the topology that supports it. A straightforward way, would involve directly measuring the magnetic field of the corona, however current direct measurements are rare and insufficient to create a 3D picture. The

magnetic field of the corona is weak, only measuring 1 to 10 Gauss, except right above solar active regions where it reaches $\sim$ 300 - 800 Gauss [Kuhn and Stein, 1996, Lin and Forbes, 2000]. New instruments such as Daniel K. Inouye Solar Telescope (DKIST) [Schmidt et al., 2016], plan to address part of this problem by measuring magnetic fields of the chromosphere and the corona. Currently, the most accurate measure of the magnetic field is derived from the photosphere, where the Zeeman effect [Harvey, 1969] is applied to detect a frequency-modulated polarization signal, sensitive to the strength and direction of the magnetic field. From these measurements, we can use topological models to derive the coronal magnetic field. Generally, these methods belong to four classes in increasing level of sophistication: potential field extrapolations [Demoulin et al., 1993], linear force-free extrapolation [Wang et al., 2000, Baker et al., 2009], non-linear force-free field (NLFFF) models from LOS magnetograms [Wiegelmann, 2008, Wiegelmann and Sakurai, 2012, van Ballegooijen and Cranmer, 2010] and NLFFF extrapolations from vector magnetograms [Schrijver et al., 2008]. Each of these methods assume that Lorentz forces are negligible, that the field evolves slowly through a series of quasi-equilibrium states. This approximation applies for any slowly evolving low-$Beta$ plasma where the magnetic field pressure dominates the gas pressure, the gravitational forces, and kinematic plasma properties. Each of these models calculates magnetic topological features that can be compared to observations and MHD models, including coronal null points, the seperatrix surface,and the quasi-seperatrix layer (QSL) surrounding the flux rope. Below we describe the role of NLFFF models in describing the magnetic topology of coronal jets.

2.3.2 Justification of NLFFF Models

The solar corona is composed of magnetized plasma with large electrical conductivity. Therefore the vector magnetic field, **B**, the electric field, **E**, the electric current density, **j**, and the plasma velocity,**v**, can be described in terms of magneto-hydrodynamic equations (MHD), where particle interactions are ignored and the magnetized plasma is

considered a continuous, 'flux-frozen', and force-free fluid [Priest et al., 1994]. The flux frozen and force-free conditions are derived from the induction equation and equation of motion, which govern the coupled relationship between **B** and j for an evolving magnetic field. Specifically, the electrical conductivity of the magnetic field is given by Maxwell's equation:

$$\nabla \times \mathbf{E} = -\frac{\partial \mathbf{B}}{\partial t} \tag{2.5}$$

In addition, the plasma experiences the Lorentz force, $(j \times \mathbf{B})$. The current density, j, is related to **E** by Ohm's Law, $j = E/\sigma$, where σ is electrical conductivity. The induction equation can then be written as:

$$\frac{\partial \mathbf{B}}{\partial t} = \nabla \times (v \times \mathbf{B}) - \frac{1}{\mu\sigma}\nabla \times (\nabla \times \mathbf{B}) \tag{2.6}$$

where μ , is the magnetic permeability.

In the lower corona, the magnetic field pressure is typically is orders of magnitude higher than the gas pressure, and the length scale of particle interaction is much lower than the Reynolds number. Thus, the plasma is 'flux-frozen' and confined to move along the magnetic field lines [Alfvén, 1942]. Therefore the magnetic pressure dominates plasma motion, and other forces, other than the magnetic tension it exerts on itself, can be ignored and the Lorentz force $j \times \mathbf{B} = 0$. This condition is called 'force free' and applies describes a magnetic field in which the magnetic pressure and magnetic tension forces are in equilibrium, and gravity and other forces are negligible. The force-free state results in two consequences. First, the first term in the induction equation goes to 0, and it reduces to:

$$\frac{\partial \mathbf{B}}{\partial t} = \eta \nabla^2 \mathbf{B} \tag{2.7}$$

where η is the magnetic diffusivity, $\frac{1}{\mu\sigma}$. Second, the magnetostatic state is described by a

simplified equation of motion:

$$0 = -\nabla p + \mathbf{j} \times \mathbf{B} \tag{2.8}$$

where $j = \frac{1}{\mu 0} \nabla \times \mathbf{B}$, and $\nabla \cdot \mathbf{B} = 0$. Finally, the magnetic field, $\mathbf{B}$, and the current density, $\mathbf{j}$, are related by Ampre's Law:

$$\nabla \times \mathbf{B} = \mu 0 \mathbf{j} \tag{2.9}$$

where, $\mu 0$ is the permeability of vacuum. Since the Lorentz force is zero, the current density and the magnetic field must be parallel. So, they can be written as:

$$\mu 0 \mathbf{j} = \alpha \mathbf{B} \tag{2.10}$$

where α is called the force-free function. Ampere's law can then be written in the following form:

$$\nabla \times \mathbf{B} = \alpha \mathbf{B} \tag{2.11}$$

Hence, the electric currents must flow parallel or anti-parallel to the field lines $\mathbf{B}_{||}\mathbf{J}$ and $\mathbf{B} \sim$ J with a proportionality parameter $\alpha(r)$, where $(r) = \alpha B(r)$, shows how α changes as a function of distance r. If α is set to zero, then this describes force-free potential field models [Demoulin et al., 1993]. If α is constant across the field, then this describes linear force-free, non-potential field models [Wang et al., 2000, Baker et al., 2009]. If α is allowed to vary from field line to field line, then this describes the non-linear, force free approach [Wiegelmann, 2008, Wiegelmann and Sakurai, 2012, van Ballegooijen and Cranmer, 2010].

Potential and linear force-free models are popular because they are mathematically simplistic and only require line of sight magnetograms, as opposed to extrapolation methods, which can use vector magnetograms. However, potential field and linear force-free models assume that the magnetic field is uniform across the region, and potential field models assume that there is no free magnetic energy in the system. Thus, these are not applicable for

eruptions that are thought to be caused by the sudden release of stored free energy in the form of strong electrical currents such as coronal jets.

A different approach is to use a non-linear force-free magnetic model, where α changes as a function of distance. A key difference in NLFFF models is that the mean large-scale magnetic field remains force-free, except in regions where a non-potential, current-carrying field is introduced in the form of a flux rope. This deviation from the force-free, potential field condition allows the magnetic field to store and release magnetic energy and it is more representative of the topology of coronal eruptions, where the magnetic topology suddenly changes from storage to energy release. NLFFF models they have been applied to jets previously, with conflicting results. [Chandra, R. et al., 2017], examined the topological features of blowout jets and found evidence of a bald-patch topology, that could be responsible for jet shape and formation. While in [Thalmann et al., 2013] breakout reconnection in conjunction with kink-instabilities were responsible for jet eruption. Although, these studies conflict, they show that NLFFF models can be useful tools to determine the magnetic topology in coronal jets. One key difference in the previously discussed NLFFF models is their approach to dissipating magnetic flux elements and release stored magnetic energy. The magnetic field of the corona is anchored to the photosphere, and ultimately the convection zone, where turbulent random motions slowly disperse the field. In the photosphere this motion manifests as the slow decay of active regions, and weakening of flux concentrations. In the corona, where the field is 'frozen-in' the random motions result in entangled field lines, and small-scale reconnection events, called nano-flares. Over time, the large scale field is restructured, and regions of concentrated flux are diffused. Filaments are observed to slowly rise in response the the weakened field, until a critical point is reached leading to rapid eruption. This behavior is most often studied in filament eruptions, including those associated with active regions (sigmoids), large scale prominence, and CME initiation. This deviation from the force-free, potential field condition allows the NLFFF models to extrapolate a magnetic field to store and release magnetic energy, more

representative of the topology of coronal eruptions, where the magnetic topology suddenly changes from storage to energy release.

In magneto-relaxation models, diffusion is simulated by the continual evolution of the magnetic field through a series of steps in NLFFF equilibrium, using the evolved photospheric boundary and iterating the magnetic induction equation at each step. One advantage of this method is that the field retains a 'memory', and allows for continuous evolution of current density and free magnetic energy, rather than recalculating the field from the photoshpere at each step, as in other NLFFF models. In addition, magneto-frictional models are computationally faster, allowing us to explore several different magnetic configurations to best match observations. Finally, these models are data-driven; the lower boundary condition is a magnetogram, the inserted filament is matched by observations, and the test of the final model is the fit of the coronal magnetic field with observation, in this case of jet spires and domes. NLFFF models using magneto-frictional relaxation have been successfully applied to active region sigmoids[Savcheva et al., 2012b, 2015, 2012a, Mackay et al., 2011], filament eruptions [Karna et al., 2019], and the quiet sun [Meyer et al., 2013]. Applications of NLFFF models with magneto-frictional relaxation to jets are rare [Cheung et al., 2015]. Recently [Chen et al., 2018] applied a NLFFF model using flux insertion and magneto-frictional relaxation to a large coronal jet observed at the periphery of an active region and traced the source of semi-relativistic electron beams to the null region predicted by the model. We discuss the analysis of this jet in Chapter 3. In this work we examine coronal jets using a non-linear force free model, with magneto-frictional relaxation using SDO/AIA LOS magnetograms as the lower boundary condition. These models allow comparatively quick 3-D models of the structure of the coronal magnetic field, for an instant in time. These models use magnetograms as input and so are able to match particular observations. In the research presented here, we use the Coronal Modeling System (CMS) and Non-Linear Force Free model,with the flux insertion method to map the 3D structure of the magnetic field for jets analysed in this study.

2.3.3 The Coronal Modeling System

The Coronal Modeling System (CMS) is a Non-linear Force Free Field developed by Aad van Ballegooijen [van Ballegooijen et al., 2011, van Ballegooijen and Cranmer, 2010], that constructs the topological magnetic field of the corona using the flux-rope insertion method with magneto-frictional relaxation discussed in detail by [van Ballegooijen, 2004, van Ballegooijen et al., 2007, Bobra et al., 2008, Su et al., 2013, Savcheva et al., 2012a]. This method involves inserting a weakly twisted flux rope into a potential field and then allowing the field to relax to a force-free state through magneto-frictional relaxation. The models are constrained by HMI LOS magnetograms as the lower photospheric boundary conditions, and AIA observations of the jet spire and dome. Advantages of this method are that it only requires LOS magnetograms (as opposed to vector magnetograms), it is constrained by data rather than idealized sources, and is computationally quick (compared to MHD simulations), thus allowing a range of magnetic topologies to be explored. We note that CMS also has a capacity to construct a topological model using vector magnetograms, but they are not necessary for this work. Each NLFFF model computes magnetic energy, free energy, potential energy and relative magnetic helicity. In this section we summarize the process of constructing the topological model using the flux rope insertion method. See [Bobra et al., 2008] for a more detailed description of the model. Figure 2.11 illustrates each step of the process.

1.) Calculate a global potential field and a local potential field. The process begins with inputting a full-disk HMI line-of-sight magnetogram and synoptic carrington magnetogram that captures the 27 day solar rotation. The code extracts the magnetic map from the observed magnetograms. Step a in Figure 2.11 At each point the global radial field is computed, $B_r = B_{\|} \,/\, \cos\theta$, where $B_{\|}$ is the LOS magnetic field and θ is the heliocentric angle. This formula is accurate (a) when the observed field is radial on the Sun, and (b) when we observe away from solar limb, and preferably near disk center. The formula is not accurate in sunspot penumbrae away from disk center because the magnetic field in the penumbra

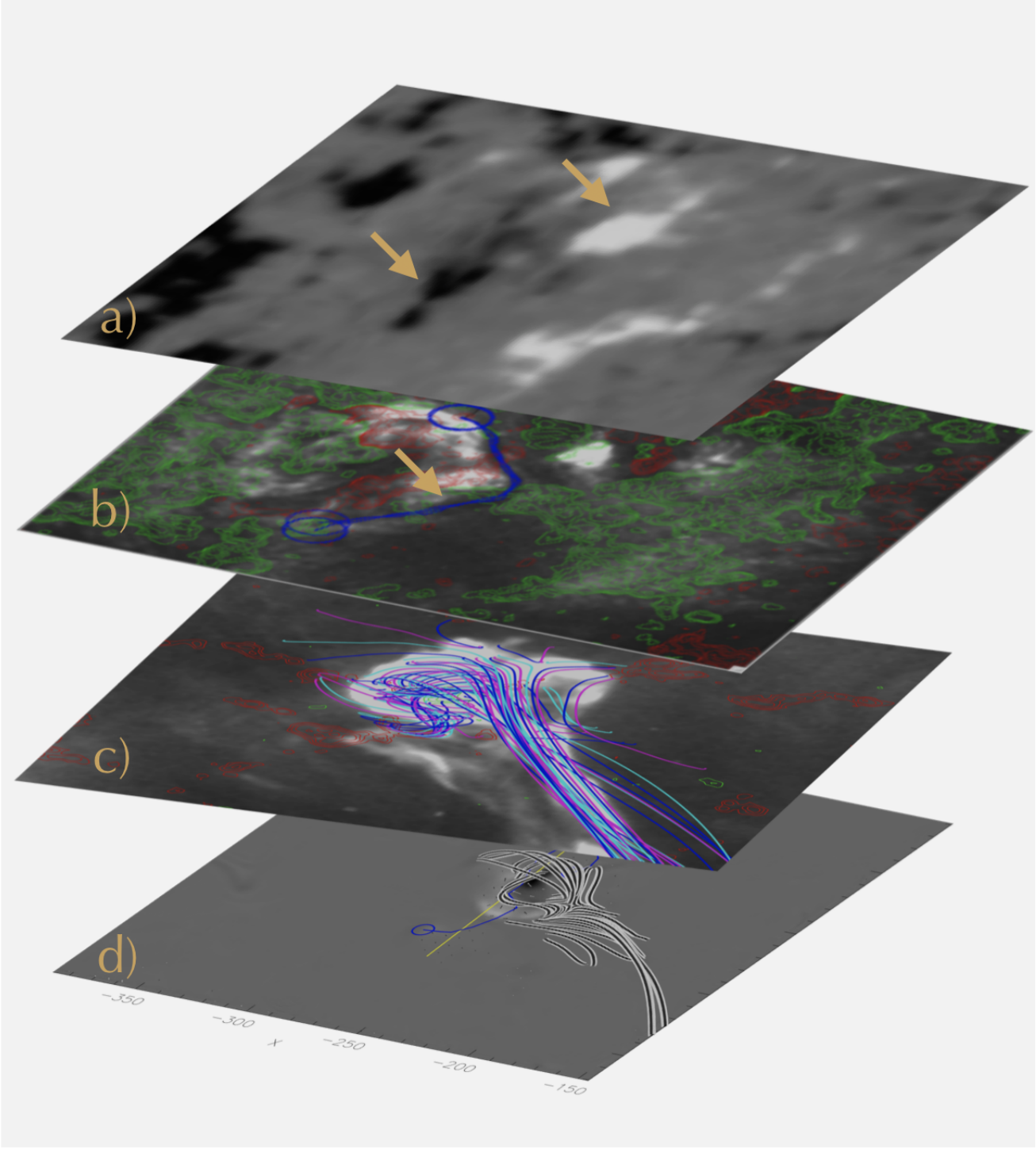

Figure 2.11: Steps in generating NLFFF model with flux insertion

has a strong horizontal component. The LOS magnetic field is not as accurate near the limb, due to limb effects. Next, a region of interest is selected (a 3D wedge from the solar

surface to $\sim 2R_{\odot}$) and the high resolution potential field is calculated, thus dividing the map into 2 parts; the high resolution (HRES) region within the selected region of interest, and low-resolution (LRES) outside of the region of interest. The region of interest is analysed using a smaller grid, thus higher resolution, while the distant regions use smaller grids (lower resolution). The potential field in the LRES region is computed from the Carrington magnetogram, with the the full disk HMI magnetogram inserted as the lower boundary. The potential feild is calculated in spherical coordinates by: $B_o = B_{mr}(\frac{R_{\odot}}{r})^2\mathbf{r} - \nabla(\frac{\partial\Psi}{\partial r})$ where $B_m r$ is the open-ended radial component of the field, $R_{\odot}$ is the solar radius, $\frac{\partial\Psi}{\partial r}$ describes the change in magnetic flux vector components as a function of spatial coordinates (distance). The HRES area contains currents, while the more distant region is a current free, potential-field. The result is a map of the magnetic field where B_0 matches the radial field in the photosphere and $\frac{\partial\Psi}{\partial r}$ at the open ended radial field. The calculation is done is such a way that the normal component of magnetic field at the side boundaries of the HIRES domain is continuous across these side boundaries.

2) Insert Flux rope Next we select the flux rope path and specify its parameters. Step b in Figure 2.11 shows the path of the selected flux rope (blue line). The flux-rope path is manually selected using AIA 304 and AIA 193 Å images as a guide. In EUV the flux rope appears as dark S or J shaped feature, that lies in between the positive and negative polarity flux (called the polarity inversion line). We manually draw the path of the flux rope, from positive to negative polarity flux at small height above the photosphere. The exact path of the flux rope is not needed, we can adjust the path of the flux rope if the extrapolation does not match observations. The flux rope is given a set of axial (flux that runs along the path,ϕ in Mx) and poloidal flux (closed field lines that run around the flux rope per unit length in Mx per unit length cm $^{-1}$) based on the strength of the magnetic flux at the base of the jet. We run a grid of axial and poliodal fluxes beginning with $/sim$ 20 percent of the positive magnetic flux. Typical values of axial and poloidal flux are 1E20, and 1E5, respectively. Flux ropes are known to have a sinistral (S-shaped with left helical twist)

or dextral(inverse S twist and right helical twist) direction of the magnetic field along the channel, with respect to the positive polarity [Martin, 1998]. Therefore we identify the flux rope as positive or negative axial flux depending on the direction of the twist. At the two ends of the path, the tube is anchored in the photosphere and helicity is concentrated in the center of the flux tube rather than the ends.

3) Relax the model using Non-linear Force Free topological model The next step is to relax the field into a force-free equilibrium state using a process called magneto-frictional relaxation [Yang et al., 1986, van Ballegooijen, 2004]. Magneto-frictional relaxation is the processes by which the magnetic field is evolved by the induction equation, slowly or quasi-steadily at a velocity proportional to the Lorentz force. As in the passages above, plasma in the coronal is low-β and considered 'frozen in', and force-free. However ,the filament, when in motion, experiences a small frictional force with respect to the ambient corona described by the velocity,v, $v = F/v$, where F is the Lorentz force, and v is the co-efficient of friction. Therefore by imposing this small force, magneto-friction acts to incrementally dissipate magnetic energy, allowing the filament to move upward. Essentially, magneto-friction has the effect of expanding the flux rope until its magnetic pressure balances the magnetic tension applied by the surrounding potential arcade for each step in the iteration. Thus the magnetic field at each step is described as:

$$\frac{\partial \mathbf{B}}{\partial t} = -\nabla \times \mathbf{E} \tag{2.12}$$

where $\mathbf{E} = -v \times \mathbf{B} + \eta \mathbf{j}$. An additional term, hyper-diffusion is added to the induction equation to describe the relationship between the stressed non-potential, flux rope and the diffusion rate of magneto-frictional diffusion. Without hyperdiffusion, when helicity increases, the Lorentz force would result increasingly larger frictional forces, and larger upward motions of the filament. Instead, hyperdiffusion works to dissipate the increased helicity at the boundaries of the HRES region, allowing helicity to be conserved, and allowing the field to evolve in steps of in quasi-equilibrium. The MF method assumes plasma

velocity to be proportional to the Lorentz force, so that the field evolves toward a nonlinear force-free state. Thus the magnetic field can be written as a combination of both diffusion mechanisms:

$$\frac{\partial \mathbf{B}}{\partial t} = \nabla \times (v \times \mathbf{B}) - \eta_i \nabla \times \mathbf{B} + \frac{B}{B^2} \nabla \dot{(} \eta_h B^2 \nabla \alpha) \tag{2.13}$$

where η_h is the hyper-diffusion [Boozer, 1986, Bhattacharjee and Kwok, 1986], and both hyper and regular diffusion are constant in space. During the relaxation process, the bottom boundary is fixed as defined by the LoS magnetogram, the side boundaries are fixed as defined by the potential-field values of the low- resolution full-Sun potential-field extrapolation, and the top boundary is open. Other than the fixed boundaries, magnetic fields are allowed to vary throughout the wedge volume. The cell size is increased in the HRES region, and reduced in the LRES region to increase computational speed. In the photosphere, the grid size is $\sim 1.5x10^{-3} R_{\odot}$ or 1 megameter. In this study we use 90,000 iterations of increasing grid size to relax the model into a force-free state. Magneto-frictional evolution has two possible outcomes: either the flux rope settles into a force-free state (called stable model), or the field expands indefinitely and never reaches a force-free state , i.e an 'eruption' occurs (unstable model) [Bobra et al., 2008, Su et al., 2013]. This is not an eruption in the same sense of 3D MHD models, where magnetic energy is released as thermal and kinetic energy. Instead, an eruption means the flux rope is no longer in equilibrium with the surrounding region, i.e. the loss of equilibrium occurs when the forces due to the axial and poloidal fluxes become larger than downward magnetic force of the overlying field. During the flux insertion process, we first create a stable model, in which the topological features are matched but the forces due to the torordial and axial fluxes are less than the overlying field. Once a stable model is found, we increase the axial flux until an unstable model is created.

4.) Match the result with Observations For each jet we construct a grid of NLFFF models with different axial and poliodal fluxes until we determine which model matches observational properties,.i.e. the jet spire and dome direction and location. This process

involves mapping the field lines of the model and matching them with observations in AIA images. CMS uses a three-dimensional visualization tool that displays field lines in projection onto the plane of the sky. First, the image is aligned with the model using the limb of the Sun. Then we hand select field lines that best represent topological features in AIA observations. In Figure 2.11c, we have selected field lines where we expect to find evidence of reconnection between the ambient corona and the jet loop system. We select lines along the jet spire, near the jet base, and near the interface region between the jet and ambient corona. We can see that the spire length direction and cusp is well matched by the topological model.

5.) Compare best-fit model to data Once we have found a best fit model, we can use the 3D topological features to identify regions of concentrated current density, and topological features like magnetic nulls , seperatrix layers and quasi-seperatrix layers. Figure 2.11d shows an cut of the current distribution in the SZ plane of the jet. We can identify the magnetic null as the region where the magnetic field converges and goes to 0, highlighted by the yellow arrow.

Finally, we record the parameters of the filament, magnetic energy, free energy, potential energy and relative magnetic helicity. These parameters can then be compared to predictions from MHD simulations and observations.

2.3.4 Quasi-Seperatrix Layer Visualization Tool

CMS outputs a 3D topological model of the magnetic structure of the jet. From there, we then can examine a proxy for the squashing factor, Q [Titov, 2007] in the magnetic field. Q, describes regions of sharp discontinuities in the magnetic field and is calculated by calculating the derivative of magnetic field for bundles of magnetic field lines where each domain is bound by a 3D seperatrix or quasi-seperatrix layer(s) [Priest et al., 1994, Demoulin et al., 1993, 1994], which separates the null point from the outer open magnetic field lines, and the inner closed loops. The QSL calculation is a useful proxy to investigate

the electric field in regions of enhanced current density where current sheets are expected to develop [Aulanier et al., 2005]. Work by [Janvier et al., 2016, Chintzoglou et al., 2017] compared the regions of enhanced current density calculated by QSLs, with those of calculated by MHD model of an active region. They showed that QSLs can accurately give the locations of magnetic nulls and separatrices in evolving magnetic topology. [Tassev and Savcheva, 2017] developed software capable of calculating calculating Q in three dimensions, given a 3D sampling of magnetic field measurements spherical or Cartesian coordinates. This model has also been successfully applied to sigmoidal active regions [Savcheva et al., 2012a] and filament cavities [Karna et al., 2019].

Chapter 3

Results: Evidence for Chromospheric Evaporation in Coronal Jets

3.1 Description and Evolution of Jets

A straight forward way to determine if chromospheric reconnection plays a role in the acceleration of jet plasma is to look for a correlation between temperature and velocity. In this study, we use a novel technique to investigate the acceleration mechanism in six coronal jets. Using observations from Hinode's X-ray Telescope (XRT), Solar Dynamics Observatory's Atmospheric Imaging Array (SDO-AIA), and the Interface Region Imaging Spectrograph (IRIS), we capture the plane of sky velocities along the jet spire. When available, we use IRIS spectroscopic observations of Si IV line profiles to calculate Doppler velocities and non-thermal line broadening. We construct differential emission measures (DEMs) as a proxy for temperature, and determine if the jets show evidence for chromospheric evaporation. We also look for evidence of twist and/or erupting filaments in order to eliminate acceleration mechanisms. We present evidence of a temperature-dependent velocity in at least 2 jets with velocities ranging from 200-500 km/s, consistent with chromospheric evaporation.

We observed six coronal jets using imaging data primarily from SDO-AIA. When available we include observations from Hinode-XRT, and IRIS slit-jaw and spectroscopic data. Four of the jets are observed using both XRT and SDO images, two use only SDO AIA data, and two jets are analyzed using XRT, AIA, and IRIS data. We have selected jets that are distinct from the background, with a spire that is easily identifiable in EUV and X-ray images, with visible foot points, and a high enough image cadence to calculate the plane of sky velocity. We do not include small jet-like eruptions, surges, and eruptions in AIA 304Å that do not have an EUV counterpart. In the section below, we describe the instruments used in this study, data preparation, and jet observations. Figure 3.1 shows images

of six jets observed in the SDO/AIA 193Å channel on or near the time of peak emission. Jet 2 is a quiet sun jet. All other jets occur in the periphery of active regions.

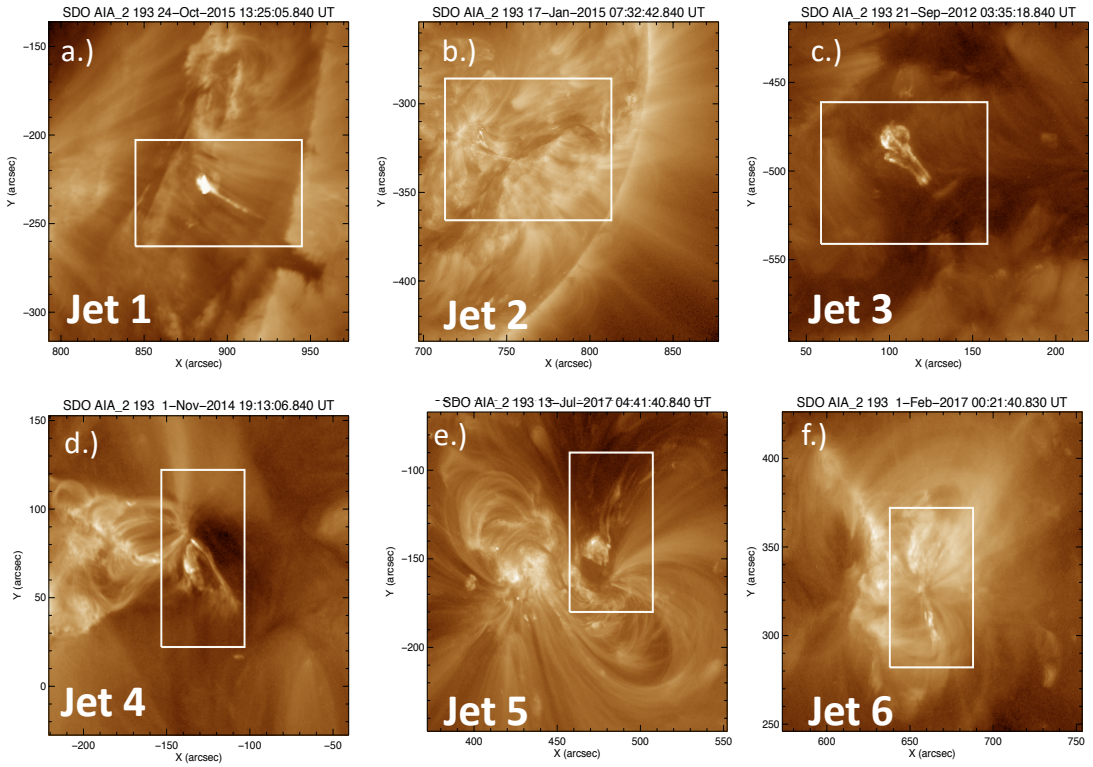

Figure 3.1: Six jets observed in the SDO/AIA 193Å channel on or near their time of peak emission. Jets 1,2,4-6 occur on the periphery of active region. Jet 3 appears in a quiet region.

Below, we discuss the coronal evolution of each of the jets in this study. There are six jets, all observed with AIA, two with additional observations with XRT, two with additional IRIS slit jaw imager, two with IRIS spectrometer data. These observations are summarized in Table 3.1. We describe the coronal evolution, and the evolution of the filament when ob-

Jets Observed in this Study

Jet Number, Type, Region	Peak Time	Instruments Utilized
Jet 1. Standard, AR	2015-10-24 13:25 UT	AIA,XRT,IRIS
Jet 2. Blowout, AR	2015-01-17 07:32 UT	AIA, IRIS
Jet 3. Blowout, QR	2012-09-21 03:35 UT	AIA
Jet 4. Blowout, AR	2014-11-01 19:05 UT	AIA
Jet 5.Standard, AR	2017-07-13 08:33 UT	AIA,XRT,IRIS
Jet 6. Standard, AR	2017-02-01 00:21 UT	AIA, IRIS

Table 3.1: Jets observed in this Study. Jets are listed by type, embedded region, date and time near peak of eruption, and instruments used in analysis.

served. We have calculated the plane-of-sky (POS) velocity using the procedure described in Section 3.2.1. To examine if there is evidence of twist, we follow the procedure described in Section 2.2. The aim of this body of work is to examine possible acceleration mechanisms in coronal jets using multi-wavelength observations. To determine if jets show evidence of chromospheric evaporation, we calculate the plane of sky velocity as a function of temperature for each of the jets. Both AIA and XRT are broad band channels, i.e the temperature response function is sensitive to a range of temperatures, see Figure 2.2, thus we can employ a differential emission measure technique to determine plasma temperature.

3.1.1 Jet 1 Observed 2015-10-24 13:25 UT

Jet 1 shown in Figure 3.1a develops near the center of of an active region (NOAA 12434) $\sim$13:25 UT. It has a narrow pencil-like spire in EUV, therefore we consider this jet to be 'standard'. It is also accompanied by an eruption of cool, dense narrow jet-like spire in 304Å. The jet was observed in XRT Al/Poly and Be-thin channels (using 2.5 min cadence), IRIS 1400 slit-jaw imager, and the AIA EUV channels. The eruption duration is $\sim$ 30 minutes from (13:20-13:30 UT) and peak POS velocity to be $\sim$ 550 km/s.

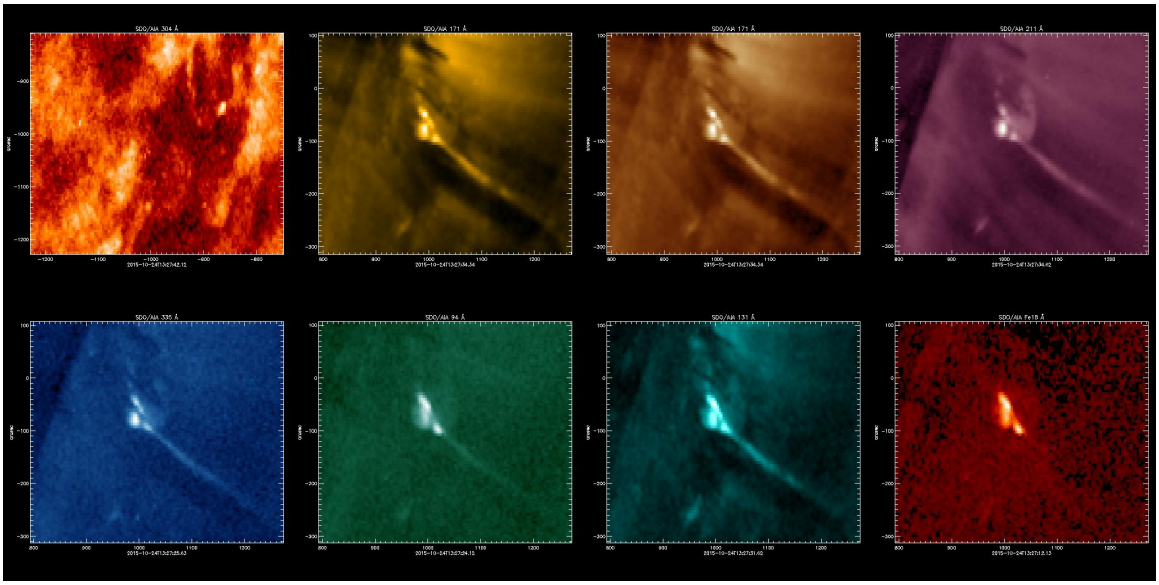

Figure 3.2: Jet 1 Observed 2015-10-24 in AIA channels.

3.1.2 Jet 2 Observed 2015-01-17 07:32 UT

Jet 2 shown in Figure 3.1b develops starting at $\sim$ 07:32 UT between two large compact negative flux regions in an active region in the south west limb of the solar disk, preceded by several smaller eruptions. The jet can be classified as 'blowout', since it has a wide curtain-like spire in EUV, and a similar eruption in UV (SDO 304Å). The jet spire has a helical motion and a visible filament that lies along the polarity inversion line of the lower positive flux region. This filament erupts at the same time of the jet. Later, we develop a non-linear force free model of this region and discuss the impact of the filament on the jet trajectory.

3.1.3 Jet 3 Observed 2012-09-21 03:35 UT

Jet 3 shown in Figure 3.1c develops in the quiet sun $\sim$ 07:31 UT. This jet has a broad spire and an accompanying eruption and emission in AIA 304 Å. No active regions, bright points or plumes were present, however the region is the site of strong disorganized magnetic flux. After the eruption, material can be seen falling back onto the disk on nearby

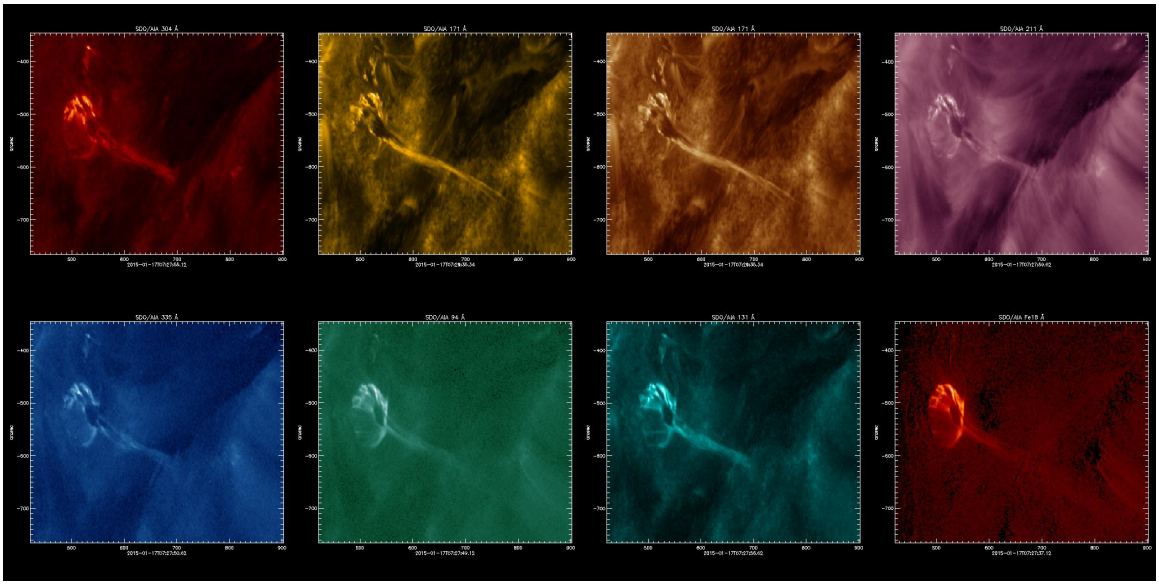

Figure 3.3: Jet 2 Observed 2015-01-17 in AIA channels.

field lines. Minutes before the eruption, positive polarity flux can bee seen moving towards a smaller negative polarity region. The negative flux appears to cancel, becoming more compact and circular shaped. The eruption occurs when the two opposite polarity (and now more compact) regions become close to each other, resulting in an s-shaped eruption and twisted jet spire. Jet 3's duration is about 10 minutes from (03:34-3:44). After the eruption, a smaller bipolar region remains and the positive polarity flux continues to cancel while the negative flux appears to become more compact.

3.1.4 Jet 4 on 2014-11-01 00:21 UT

Jet 4 shown in Figure 3.1d develops on the southern periphery of AR12203 near disk center $\sim$ 19:01 UT. The AR lies between two other small active regions that interact frequently. The region erupts several times for a few hours, we focus on the eruption beginning $\sim$ 1901-19:17 UT that results in a bright narrow spire on the outer boundary of the bubble of the ejecta.

At the time of the eruption there appear to be two filaments present, a small one on the right along the boundary, and a larger filament to the left. The eruption is circular and broad,

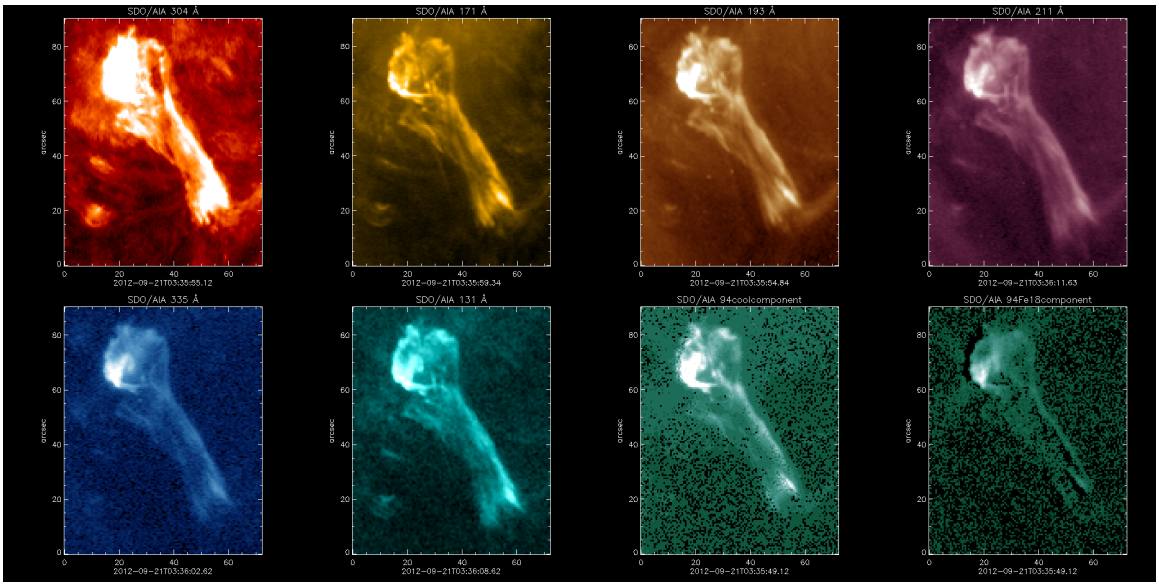

Figure 3.4: Jet 3 Observed 2012-09-21 in AIA channels.

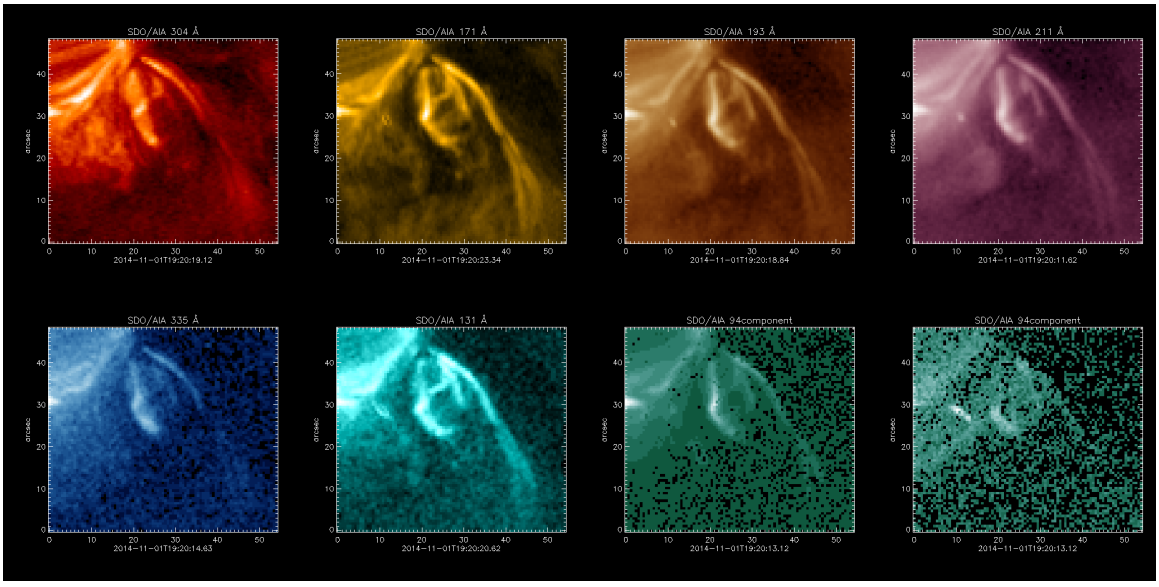

Figure 3.5: Jet 4 Observed 2014-11-01 in AIA channels.

rather than the narrow spire typically seen in jets, with several parts moving at different velocities (we discuss the calculation of velocity in Section 3.2.1).This eruption is most effectively classified as a blowout jet, since it resembles a small CME, with corresponding eruptions in AIA 304 Å. This eruption is associated with Type III radio bursts and semi-relativistic particles [Chen et al., 2018].

The region where the jet develops is on the boundary of the negative flux region, and diffuse positive flux regions. Before the eruption a small bipolar region emerges between the negative and positive regions, resulting in a small eruption that appears to destabilize the lower region, culminating in a circular eruption that encompasses the lower portion of the active region. Magnetically the jet appears to originate from positive polarity flux emerging between two regions of negative polarity. Later eruptions appear to be due to the continual emergence and cancellation of this flux. The eruption's lifetime is $\sim$ 20 minutes from (19:01-19:20 UT).

3.1.5 Jet 5 2017-07-13 08:33 UT

Jets 5 in shown in Figure 3.1e erupts within AR12665, a large sigmoidal active region. The jet emanates from a region with re-occurring jets that erupt several times over a two day period. This jet and the other re-occurring jets are all standard, with a characteristic bright point at their base. The spire of the jets is narrow and at the peak of eruption the material appears to follow the magnetic field lines, back downward towards the disk. Jet observations were taken using SDO at a 12 second cadence and Hinode Be-Thin at an 8 sec cadence during a high data rate campaign. The eruption's lifetime is $\sim$ 20 minutes from (19:01-19:20). Magnetically, the jet we focus on erupts over a bipolar region. The jet appears to be the result of magnetic flux cancellation between small regions of opposite polarity flux and is one of several other jets emanating from the same active region. Over the course of the eruption, the positive polarity flux is eroded, leaving a small amount, which is responsible for the appearance of bright point in EUV.

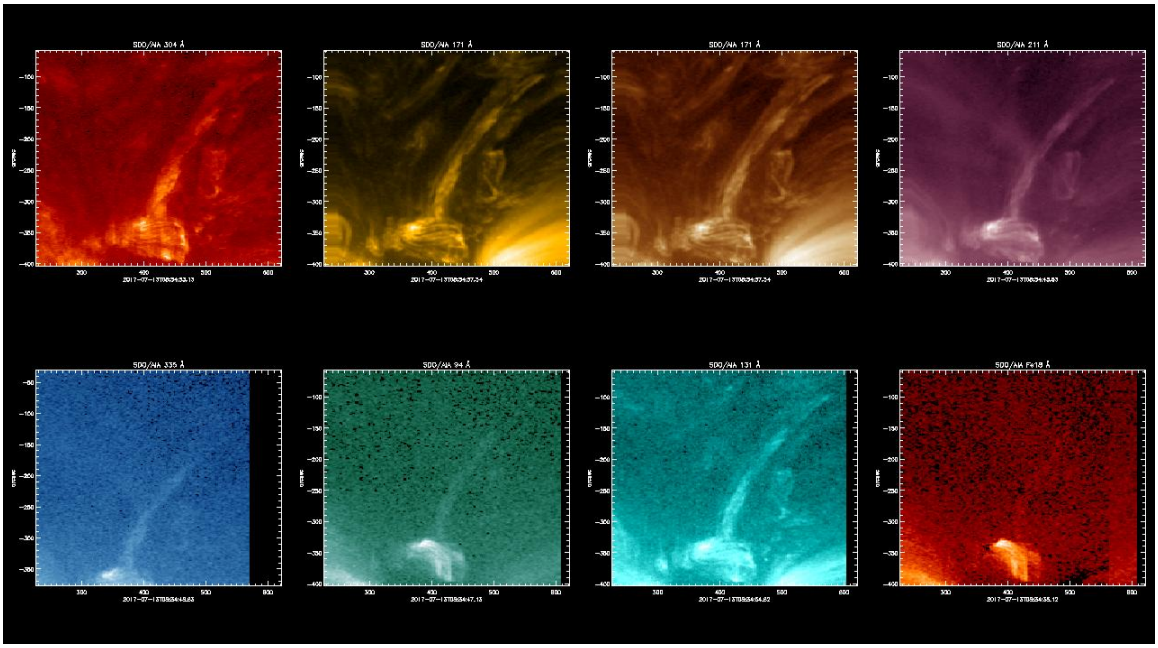

Figure 3.6: Jet 5 Observed 2017-07-13 in AIA channels.

3.1.6 Jet 6 2017-02-01 00:21 UT

Jet 6, shown in Figure 3.1f erupts near the southwestern region of the a small, unnamed active region. A filament can also be seen erupting near the jet, but it is very small, so it is not clear if the eruption of the filament is the catalyst for the jet's eruption or if a re-configuration of the magnetic topology is responsible for both jet and filament initiation. The erupted plasma has a broad structure. We consider this jet a blowout jet, but it could also be classified as a small surge. This eruption was observed by IRIS spectrometer and the raster slit aligns with the jet spire. Therefore we can calculate the plane of sky velocity, Doppler velocity and non-thermal broadening for the jet spire. See Section 4. The jet erupts when negative flux emerges into near the base of the active region.

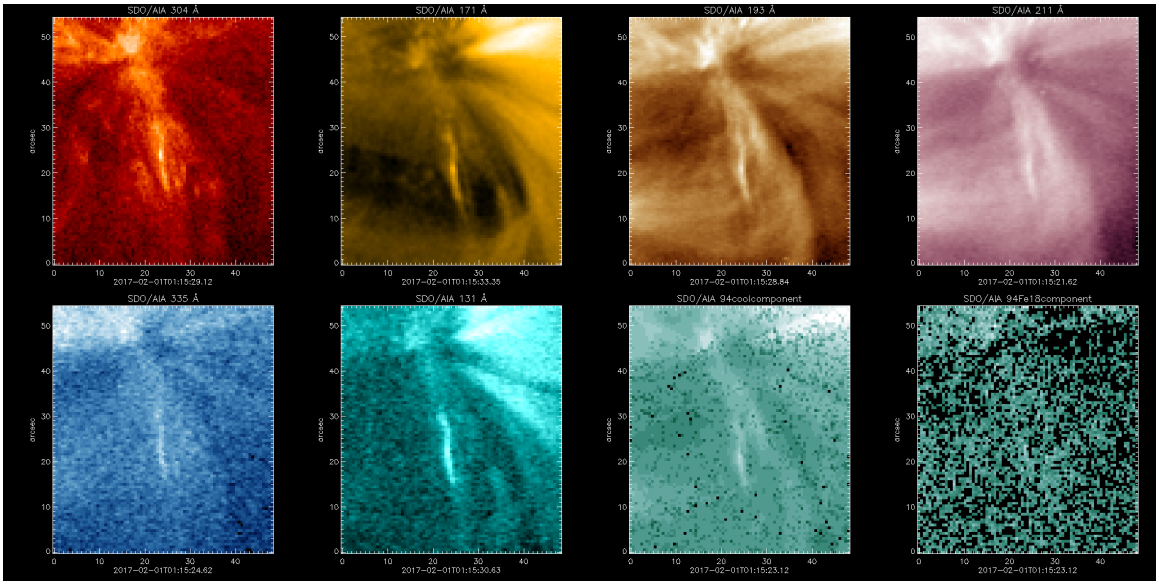

Figure 3.7: Jet 6 Observed 2017-02-01 in AIA channels.

3.2 Examining Chromospheric Evaporation in Jets

3.2.1 Results of Temperature vs Velocity Analysis

In Figures 3.8 - 3.13 we plot the line of sight velocity as a function of temperature for the six jets in this study. The plane of sky (POS) velocity is calculated using the stack plot method (described in section 2.1.2) and the temperature distribution for each channel, Tprime, is calculated from the DEM. POS velocity is calculated for the following channels; IRIS slit-jaw 1400 and 1330 Å, AIA-131,171,193,211,335, and 94Å channel separated into the Fe XVIII and 'cool' residual components, and XRT channels, Al-poly and Be-thin. The channels included in the DEM analysis are the AIA-EUV channels and XRT-X-ray channels when available. The IRIS 1330 and 1400 Å channels contain emission from both optically thick and optically thin plasma. We are not able to separate these components at this time, so these channels are not included in the DEM calculation. Instead, Tprime is taken as the peak formation temperatures for the spectroscopic lines that are the main contributors to the emission in the slit jaw channels. For the 1330 Å channel the primary contributor is C II, at a peak formation temperature of LogT 4.6, and for the 1400 Å channel

the primary contributor is Si IV at LogT 4.8.

In the Figures below we also plot the sound speed (dotted black curve) and 2.35 $\times$ the sound speed (dashed black curve). [Fisher et al., 1985] estimated the maximum temperature expected if plasma is accelerated due to chromospheric evaporation in active region flares, which was found to be 2.35Cs. [Matsui et al., 2012] found a similar trend when applied to one observation of a coronal jet with the Hinode/EIS spectrometer. In this work, if the plasma velocity increases as a function of temperature and lies within 2.35Cs limit, we interpret this as evidence of chromospheric evaporation. In each plot, the error in velocity in indicated by vertical lines at the largest temperature contributor, Tprime, in each channel. All of the jets in this study are observed using AIA but do not always have XRT or IRIS observations. The observations used for each jet, are described in Table 1. In the following section, we will refer to the channels used to calculate velocity *Vchannels*, and refer to the channels used to calculate DEM as *Tchannels*.

Figure 3.8 shows velocity vs temperature for Jet 1, observed 2015-10-24T12:54. The velocity is calculated using the 6 AIA-EUV channels, Al-poly, Bethin, IRIS-slit jaw. The velocity in the hot channels (Bethin, Alpoly, Fe XVIII, 211Å) and the cool channels (171,193 Å) both follow an increasing temperature-dependent trend. In the 335Å channel (dark blue), the temperature contribution seems to be bimodal, i.e. a large number of tick-marks near logT 5.3 and logT 6.2. Still, the upward trend is apparent, and the velocities for the majority of the channels lies within the bounds of the local sound speed and upper limit of 2.35Cs. If we assume the plasma temperature of the IRIS 1330 Å channel is the formation temperature of CII (logT 4.3), then the trend is extended to cooler temperatures. We interpret this result to indicate the presence of chromospheric evaporation as predicted by [Fisher et al., 1985].

Figure 3.9 shows velocity vs temperature for Jet 2, observed 2015-01-17T07:20UT. The Fe XVIII component of this jet had very low signal, therefore we were not able to reliably calculate the velocity. The other AIA channels appear to be very similar across velocity.

The 193 Å channel (teal) has a Tprime value of 6.3 and a speed of 350 km/s but the 94c (dark green) and 335 A channels both have hotter values of Tprime, but lower speeds. Therefore, we conclude that chromospheric evaporation is not responsible the acceleration in this jet.

Figure 3.10 shows velocity vs temperature for Jet 3, observed 2012-09-21T03:30. Jet 3 was a blowout jet, accompanied by a large filament eruption and the eruption of large amounts of chromospheric plasma. In this jet, the POS velocity in all channels is similar at $\sim$300 km/s, though there is a slight increase as a function of temperature in the 171, 193, 211, and 94c Å channels. The temperature and velocity appear to show an inverse relationship in some channels (94c and Fe18). Therefore, we conclude that chromospheric evaporation may be responsible for the cooler channels, but not the warmer channels. In several channels, there appears to be a two primary components, near logT 5.2 and logT 6.8. The Fe XVIII temperature is notably higher than the other jets, even though the primary velocity is similar. The apparent increase in velocity as a function of temperature for the cooler channels, along with the slower speed for the Fe18 channel indicates that there is a cool component driven by chromospheric evaporation, and a hot component driven by the motion of the magnetic field, as in **?**.

Figure 3.11 shows velocity vs temperature for Jet 4,observed 2015-11-01. This jet was part of a complicated structure that erupted near an active region and contained a large erupting CME-like mass and filament. The velocities do not follow an apparent temperature dependent trend. There is not a large spread in temperature, and the velocities of the hottest plasma are slower than expected for chromospheric evaporation. Therefore, we conclude that CE is not contributing to the acceleration of this jet. We discuss this possibility of twist as an primary accelerator in section 1.5.0.1.

Figure 3.12 shows velocity vs temperature for Jet 5, observed 2017-06-13. This jet was one of several re-occurring jets from a large active region. The velocity and temperature to follow a trend characteristic of chromospheric evaporation. The velocity of several AIA

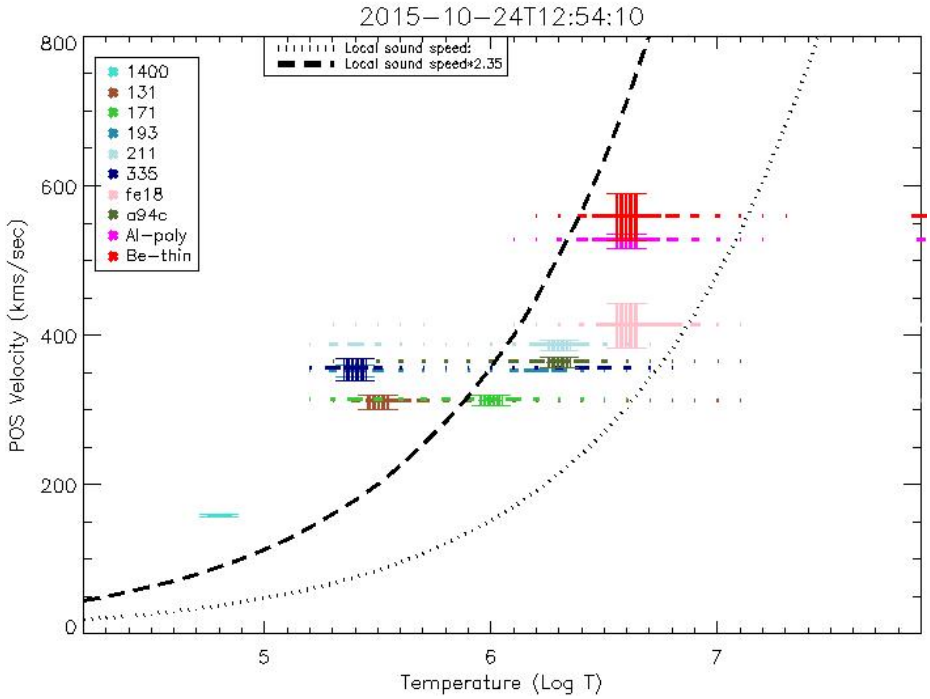

Figure 3.8: Plane of sky velocity as a function of temperature for Jet 1, corresponding to Figure 3.1a.

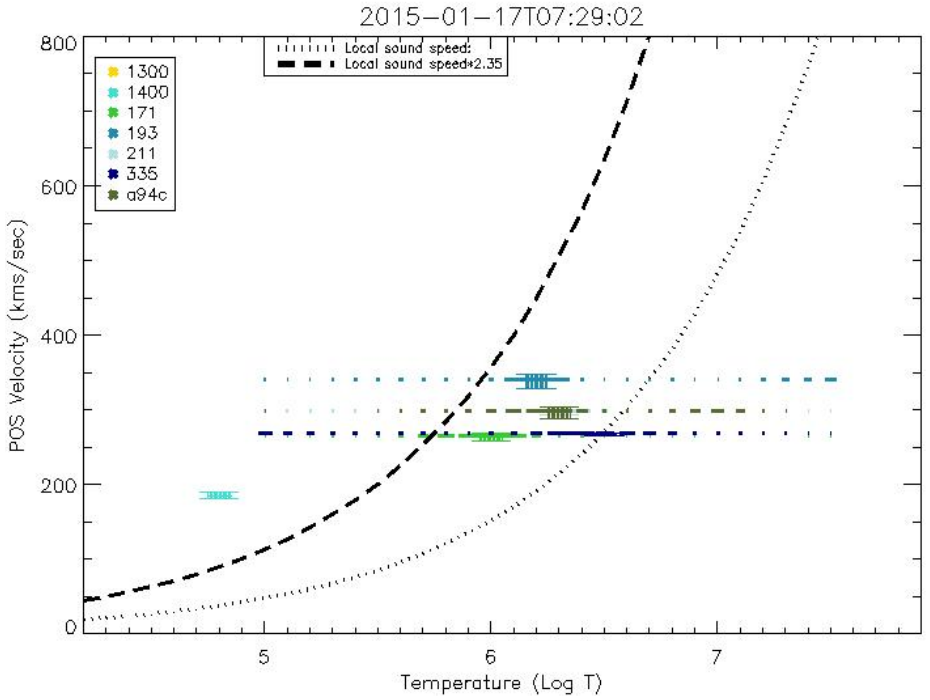

Figure 3.9: Plane of sky velocity as a function of temperature for Jet 2, corresponding to Figure 3.1b.

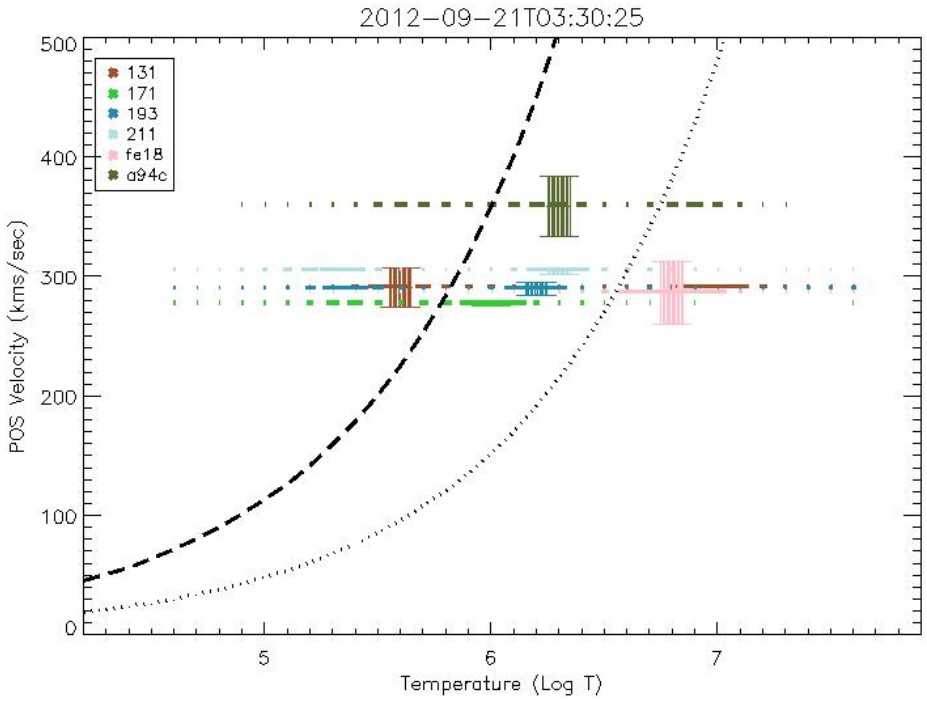

Figure 3.10: Plane of sky velocity as a function of temperature for Jet 3, corresponding to Figure 3.1c.

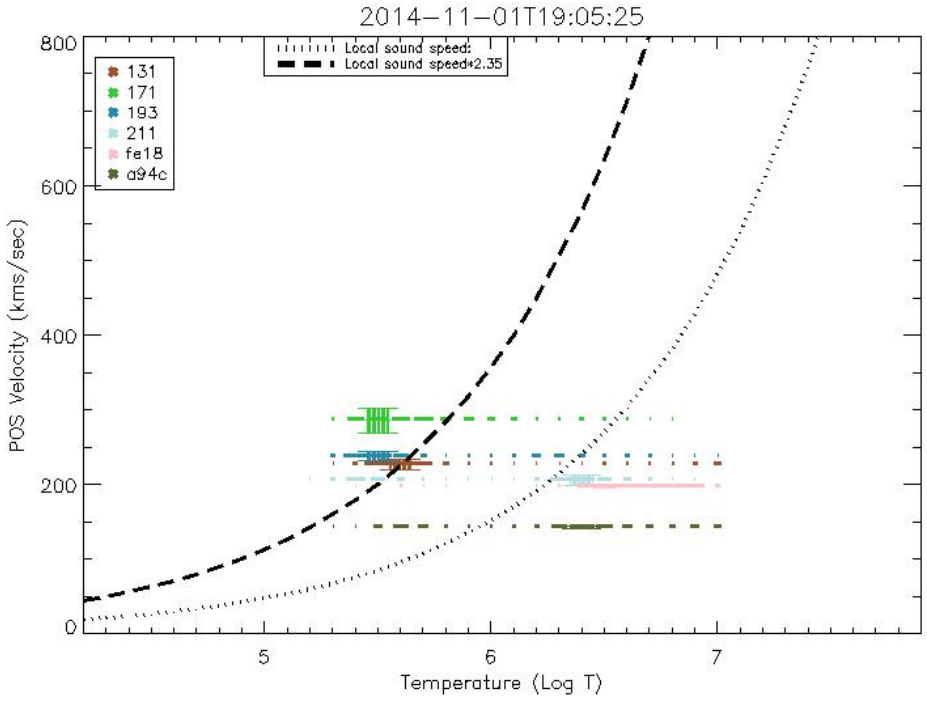

Figure 3.11: Plane of sky velocity as a function of temperature for Jet 4, corresponding to Figure 3.1d.

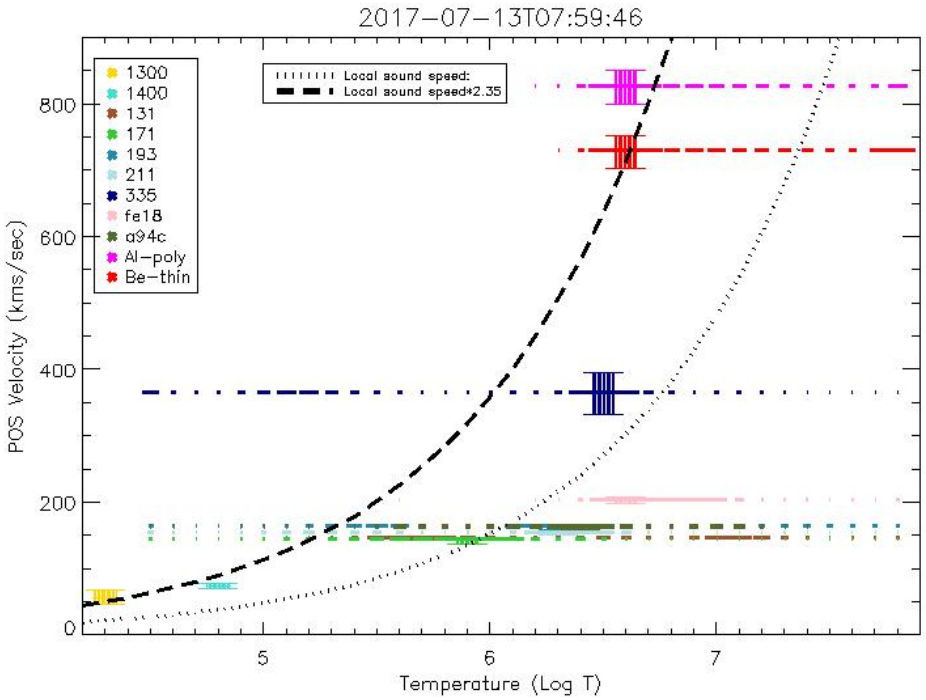

Figure 3.12: Plane of sky velocity as a function of temperature for Jet 5, corresponding to Figure 3.1e.

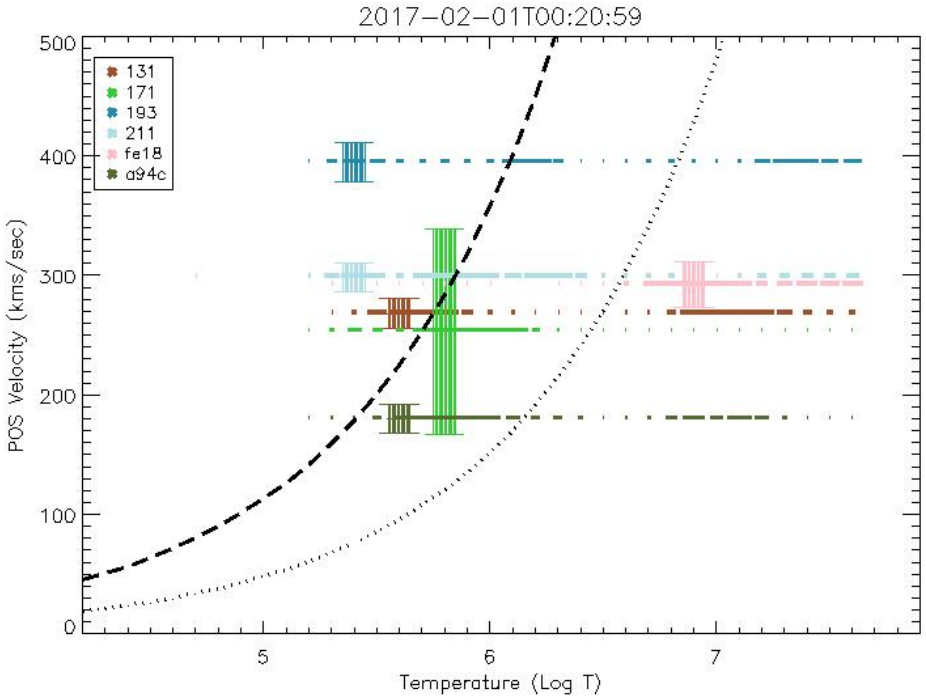

Figure 3.13: Plane of sky velocity as a function of temperature for Jet 6, corresponding to Figure 3.1f.

channels (171,193, 211, 131, Fe XVIII, 94C) are very similar but do show an temperature dependency. The velocity for channels IRIS 1330, 1400 and AIA 171 and 335 Å shown in yellow, light blue, respectively, are increasing in a trend very similar to what is expected for chromospheric evaporation. The X-ray velocities lie on the cusp of the upper limit for chromospheric evaporation, but also show a temperature dependence. Therefore for this jet, we conclude that chromospheric evaporation is primarily responsible for the jet's acceleration. However, because some of the cooler channels lie outside of the bounds predicted by CE, additional considerations may be in order.

Figure 3.13 shows velocity vs temperature for Jet 6,observed 2017-02-01. Most channels in this jet appear to have a equal contribution of cool and warm plasma. Some channels (171,193,94c) are increasing as a function of Tprime, these trends may indicate a hot-fast component, and slow-cool component, similar to jets discussed in [Shimojo et al., 1998], where magnetic magnetic tension accelerates most of the jet plasma, while CE plays a small-role in the jet acceleration.

3.3 Examining Rotation in Jets

3.3.1 Results of Perpendicular Motion

To observe helical motion, we create a time-distance plots of each of the jets in this study using AIA 193Å images. Figure 2.10 shows the result of this analysis. The images on the right show the location of the vertical slice used to generate the images on the right.The white arrow in Figure 2.10a, shows the orientation of the slice. When filaments are present, they appear as dark regions in the spire and are noted by yellow arrows. Helical motions are highlighted by curved or diagonal, white-dotted lines. The presence of helical motion perpendicular to the longitudinal motion of spire, appear as repeating diagonal or sinusoidal motions in time-distance plots (depending on the number of twists). If both the upward and downward motion is captured, the time-distance plots will show symmetric inclinations

and declination. We note that coronal dimmings can also appear as dark regions in EUV, and have been observed in jets [Lee et al., 2013]. However, dimmings are associated with the evacuation of plasma near the jet base and/or along coronal loops, not along the spire, therefore EUV images are appropriate for this study. Filaments can be seen erupting within the jet spire and/or entangled with the spire eruption.

In Jet 1, shown in Figure 3.14a, a filament erupts alongside the jet, but does not erupt within the jet. This region was the site of several large oscillating spicules that erupted independently of the jet eruption. No filament can been seen erupting along the jet spire. There does not appear to be any helical motion visible along the spire. There is evidence of repetitive motion in the jet spire as indicated by up and down motion in intensity in Figure 3.14. We interpret these regions to be plasmoid ejections, indicative of magnetic reconnection as discussed in Chapter 1. The plasmoids can also be seen in the EUV image as enhanced circular regions in the the spire. Plasmoid observations in jets are rare. Their presence in this jet (and not in any of the others in this study) may indicate the sling-shot effect from magnetic reconnection plays a major role in its acceleration.

Jet 2, shown in Figure 3.14b,a large erupting filament and helical motions are clearly visible. The jet is highly twisted, and appears to unravel as it erupts. Two similar bright regions appear from above ($\sim$ 40pixels) and below ($\sim$ 15 pixels) the jet axis, noted by white dotted lines. The upper region appears $\sim$ 1 second after the lower region, but has a very similar appearance. Later several sinusoidal motions can be seen in the jet spire. Oscillations have been studied in jet spires [Chandrashekhar et al., 2014, Zhelyazkov et al., 2017]. We are not able to determine if these motions are associated with oscillations, however these motions are much faster than previous studies, with periods of tens of seconds rather than 5 minutes [Savcheva et al., 2007, Chandrashekhar et al., 2014]. For this study, the most relevant observation is the initial helical motion of the jet, entangled with the filament.

Jet 3 shown in Figure 3.15c, also shows the presence of an erupting filament and large

scale unwinding motion. The filament erupts in the upper portion of the jet. The oscillatory motions of bright region captures the large-scale, counter-clockwise twist in the jet spire. The filament can be seen in the right panel (white lines). A filament eruption and helical motion can also be seen in Jet 4, Figure 3.15d.Within the two bright edges of the jet, we find evidence of sinusoidal motions (white dotted lines on right panel). We also see two very similar regions that appear opposite of each other 1 minute apart, similar to Jet 2. In this case we can trace what appears to be the motion of the filament (dark region, white-dotted lines). After two periods ($\sim$ 5 minutes after start of eruption), the same dark regions appear as bright regions, $\sim$ 19:17 and 19:20. We interpret this as evidence of the filament being heated in the process of the eruption. Filaments have often been observed being heated during CME eruptions [Green et al., 2007], and jets may produce a similar event. In this case, it is possible that the heating of the filament is associated with the acceleration of the jet spire.

Jet 5, shown in Figure 3.16e, also shows oscillatory motion along the spire, and the appearance of an erupting filament. In this case, the untwisting motion on the lower edge of the jet is disrupted, but the upward and downward motion of material is visible on the upper edge of the jet. This jet occurs in very dynamic active region with several erupting jets, a so-called 'jet geyser' [Paraschiv and Donea, 2019]. The region before the jet eruption is complicated and a twisting filament and ambient corona is also visible before the eruption 8:09-08:20 UT. This eruption appears to follow the background field, erupting and twisting in a similar way.

Jet 6, shown in Figure 2.10f, also involves the eruption of a filament eruption along the lower edge of the jet. As the jet erupts a dark, curved loop appears nearby. The loops are possibly being evacuated by the eruption of the jet or other processes nearby. In this case, the dark region in the upper portion of the jet can be traced to the base of the loop, therefore it is most likely a coronal dimming. However, the lower dark region, is a filament and is visible in IRIS 1400 images. Interestingly the filament appears to be twisted but the jet

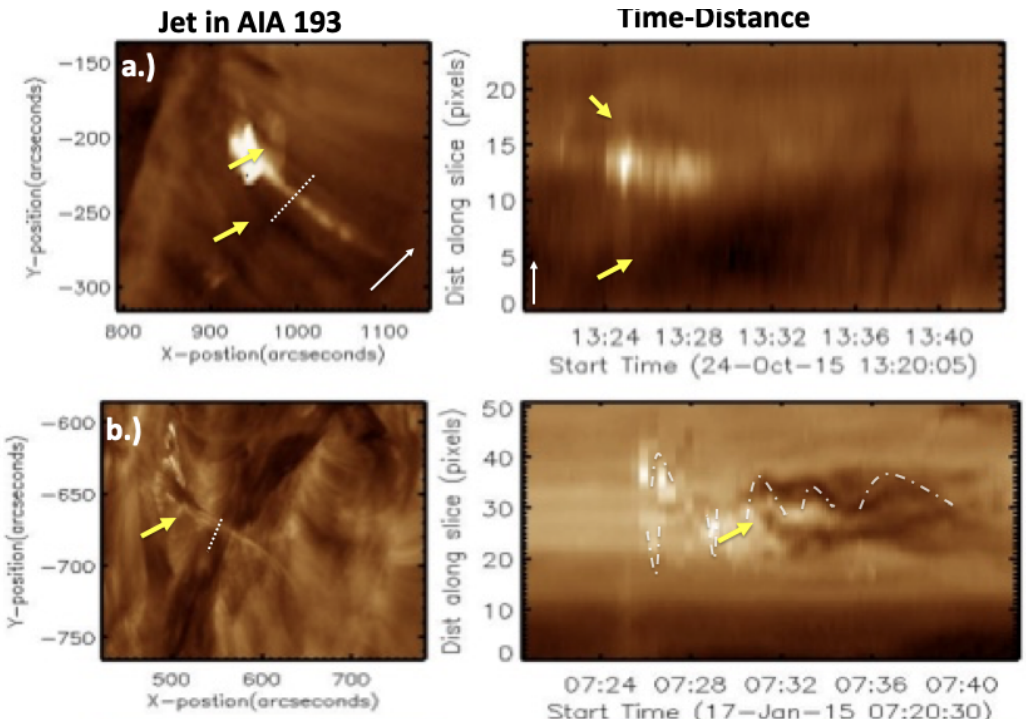

Figure 3.14: Figure a-b (Left):Jets 1-2 in SDO/AIA 193Å/. White dotted line indicates a vertical cut that was taken to make the distance-time plots on right. Right: Time-Distance plots of Jets 1-2 in AIA 193Å. The direction of slice is indicated by the white arrow. Jets 2 is associated with a filament eruption (pointed out by yellow arrow in both images). White dotted lines indicate regions of curvature associated with unwinding. Jets 2 shows twisting motion, while Jets 1 shows no twist. Jet 1 is not associated with a visible filament.

spire does not appear to have any twisting motion. Therefore, we do not think the motion of the filament is imparting energy into the jet acceleration.

In summary, Jets 2,3,4 and 5 show evidence of both twist and filaments in agreement of the filament eruption models presented by [Sterling et al., 2010b, Pariat et al., 2015b]. Jets 1 and 6 show no evidence of twist. Jet 1 is not twisted, nor associated with a visible filament, while Jet 6 shows evidence of an erupting filament, but it is not highly twisted. In these two cases, even when a filament is present, they do not appear to impart energy onto the erupting jets. However, it is possible that the filaments in these jets are too small to have an observable effect. The oscillatory motions found here have periods ranging from $\sim$ 30 seconds to 2 minutes, which is considerably higher than other reports on timescales of

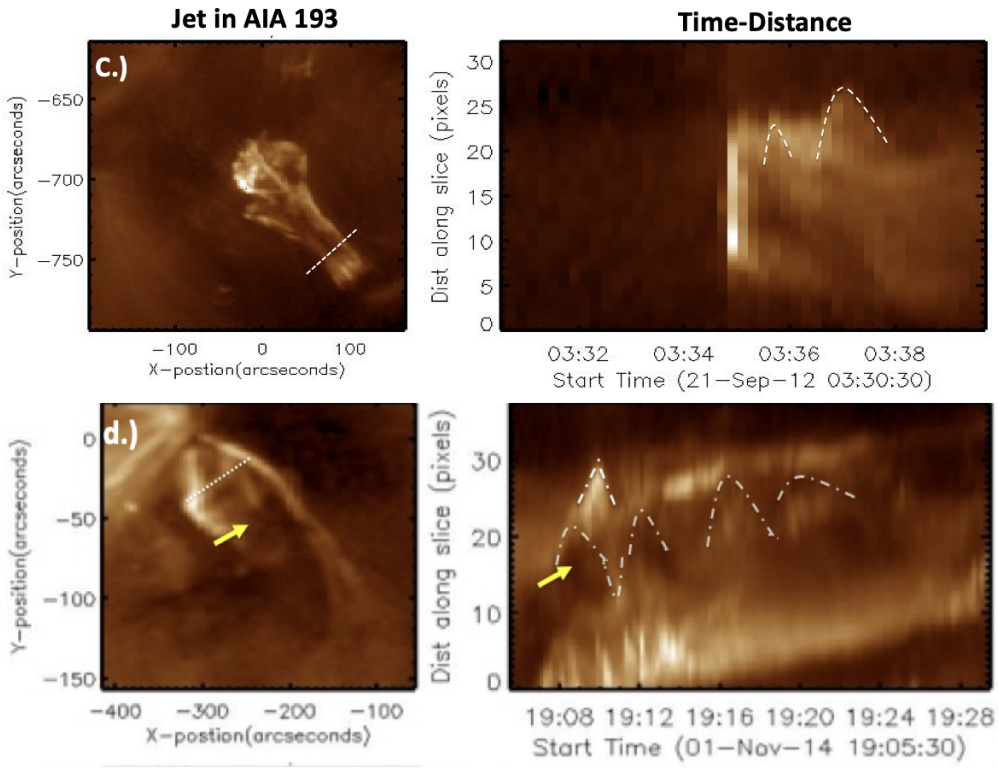

Figure 3.15: Figure c-d (Left):Jets 3-4 in SDO/AIA 193Å/. White dotted line indicates a vertical cut that was taken to make the distance-time plots on right. Right: Time-Distance plots of Jets 3-4 in AIA 193Å. Jets 3,4 are associated with a filament eruption (pointed out by yellow arrow in both images). White dotted lines indicate regions of curvature associated with unwinding. Jets 3,4 show twisting motion.

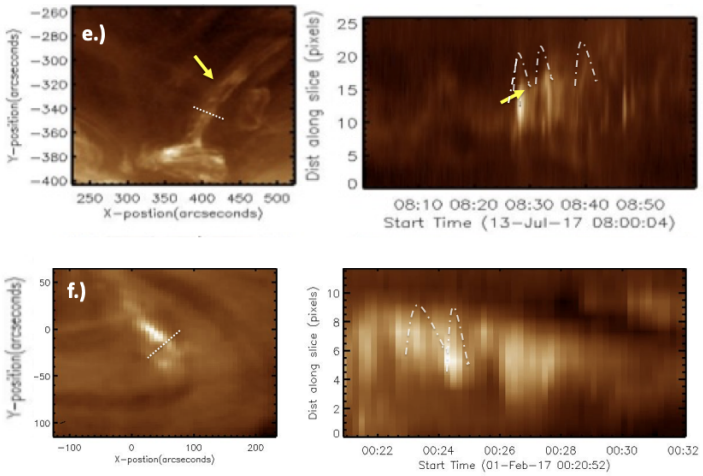

Figure 3.16: Figure e-f (Left):Jets 5-6 in SDO/AIA 193Å/. White dotted line indicates a vertical cut that was taken to make the distance-time plots on right. Right: Time-Distance plots of Jets 5-6 in AIA 193Å/. The direction of slice is indicated by the white arrow. Jets 5,6 are associated with a filament eruption (pointed out by yellow arrow in both images). White dotted lines indicate regions of curvature associated with unwinding. Jets 5,6 show twisting motion.

5 minutes or more. If torsional Alfvén waves are contributing to the acceleration of these jets, then they may explain the high period oscillations, since the periods here are similar to those of Alfven waves traveling in jet spires in 3D MHD models Pariat et al. [2009].

3.4 Spectroscopic Analysis of Two Jets

Non-thermal line broadening in spectroscopic lines has been also attributed to the presence of magnetic reconnection due to nanoflares[Cargill, 1996], chromospheric evaporation in coronal loops [Patsourakos et al., 2008], Alfvén wave shocks [Antolin et al., 2008], and/or Alfvén wave turbulence [van Ballegooijen et al., 2011].

[Savcheva et al., 2007] presented a statistical study of jets including the observation of transverse motions $\sim$ 35 km/s along the spire. This indirectly hinted at the existence of Alfvénic waves that propagate along the newly reconnected field-lines. Results by [Kim et al., 2007] used line spectroscopy to detect non-thermal line broadening and Doppler velocities in jet outflows and confirmed that they are associated with traveling Alfvénic

waves. Two jets in this study have IRIS spectroscopic raster observations. During observations of Jet 1, on 2015-10-24, the IRIS slit moves across the jet dome and base of the spire. In the observation of Jet 5, observed 2017-02-01, the IRIS slit lies directly over the jet spire. Therefore we are able to calculate the non-thermal line broadening, plane of sky velocity, and Doppler velocity for these two jets. See Figures 3.17 and 3.18 .

We use level 2 data with corrected vignetting and calibrate the data using the standard SolarSoft IRIS autofit routines. We take and additional step to calibrate the rest wavelength of the Si IV line by averaging over a quiet region along and across the raster.

Figure 3.17 shows the square root of intensity (a), Doppler velocity (b) and non-thermal line width (c) for Jet 1,in IRIS Si IV 1402.7 Å line. The jet spire is visible (outlined in the yellow dotted box) in each of the images. We find 10-15 km/s red-shifted Doppler velocities along the jet spire. See 3.17b. In this case we expect to see red-shifted plasma because the jet erupts on the limb, and the ejecta moves away from the observer, towards the outer limb along the line of sight. The upper jet footpoint, we find larger Doppler velocities of $\sim$ 20 km/s. The yellow arrow in Figure 3.17b points to regions with velocities up to 45 km/s. Some of these pixels also appear as enhanced emission in 3.17a, but the highest velocities are comparatively dim. Since we only have IRIS spectroscopic observations, we cannot verify that these flows are temperature dependent. We do not evidence of twist in the spire of the jet. If twist is present we expect blue-shifted and red-shifted plasma of the same magnitude, to lie along the spire as shown in the model in Figure 1.10 bottom. The blue-shifted material near the jet spire is a small inconsequential filament. In Figure 3.17c, we find enhancements in non-thermal width $\sim$ 55-90 km near the base of the jet spire (pointed out by yellow arrow), and at the jet footpoints. Two pixels at the base of the spire are black, indicating they were not able to be fit using the default single gaussian. We have fit these pixels using a double gaussian. However the error in these calculations need more work, so they are not included here. Even so, the remaining pixels show large enhancements in Non-Thermal Width, intensity and Doppler velocity. We interpret these

enhancements to be evidence of reconnection taking place at the base of the spire.

Figure 3.18 shows the log intensity (a), Doppler Velocity (b) and Non-thermal line width (c) for Jet 6, observed 2017-02-01, in the Si IV line at 1402.7 Å. The jet spire is highlighted by the yellow-dotted box in each of the figures. In Figure 3.18b, the negative Doppler shifted plasma (blue) in the jet spire $\sim$ 90-100 km/s, appears to originate near a region of enhanced emission in 3.18a, and non-thermal line width (3.18c). These 2 point-like regions of only a few pixels (pointed out by white arrow) show large enhancements in non-thermal width$\sim$ 90 km, similar to Jet 1. We interpret this correlation to indicate reconnection occurring near the base of the spire. The blue-shifted spire in 3.18b, indicates outward moving velocities of about the same speed as the red-shifted pixels. Alongside the spire, we find evidence of red-shifted plasma of $\sim$ 27 km/s. As mentioned earlier, if helical motion is present, we expect to see re-shifted and blue-shifted material of the same magnitude. It is not clear if the red-shifted flows are indicating twist since they are considerably slower. Interestingly, we see large velocities opposite of the jet spire near the jet base that are also correlated with enhancements in non-thermal width. These regions may be evidence of bifurcating flows moving away from the reconnection region, supporting the idea that the pixels (pointed out by arrows) are near the reconnection region.

3.5 Summary of Observational Analysis

In this study we investigate the acceleration mechanisms of 6 coronal jets. The aim of this body of work is to identify acceleration mechanisms of coronal jets using observations of plasma properties, magnetic field evolution and physical properties of twist (or lack thereof). We look for evidence of chromospheric evaporation, using the plane of sky velocity as a function of temperature, and compare the velocity to the local sound speed. We also look for evidence of filaments and twist, that could imply the presence of filament eruptions and resulting torsional Alfvén waves. When possible we use spectroscopic data to determine if there is evidence of bi-directional flows and/or reconnection from the appear-

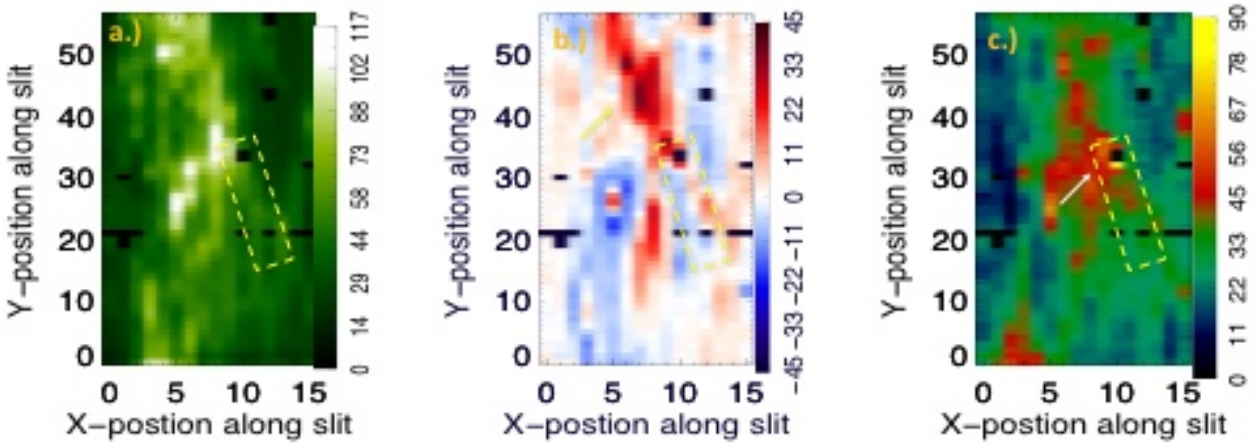

Figure 3.17: Square root of the Intensity, Doppler Velocity, Non-Thermal Width calculated from IRIS spectrometer for jet observed 2015-10-24, Jet 1.

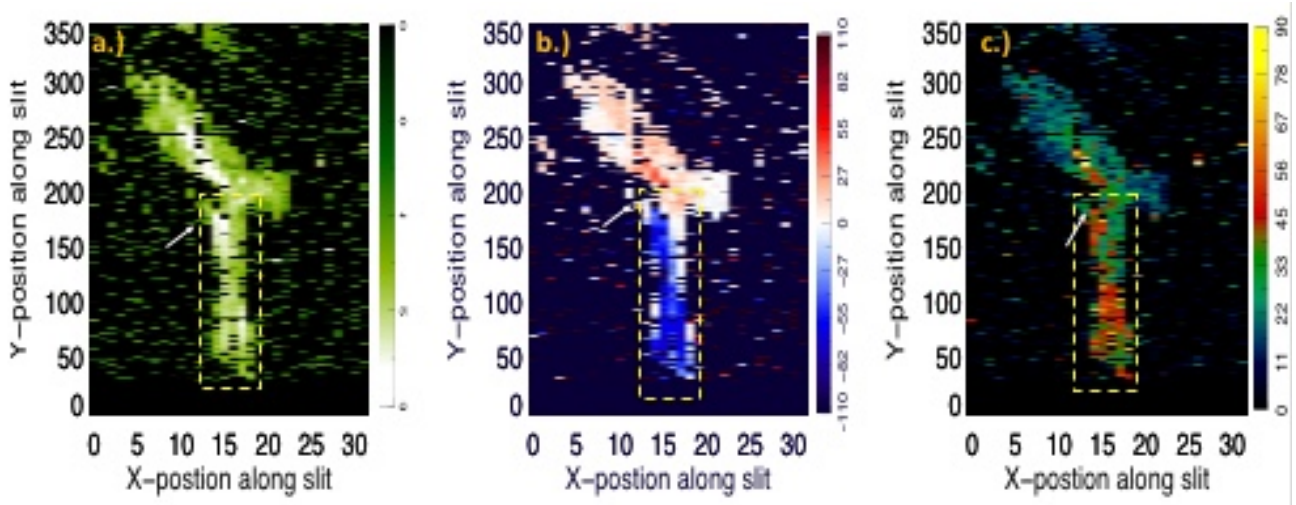

Figure 3.18: Log of the Intensity, Doppler Velocity, Non-Thermal Width calculated from IRIS spectrometer for jet observed 2017-02-01, Jet 6.

ance of non-thermal broadening. We find that four of the jets have a temperature dependent velocities within the limits 3.5Cs $>$ velocity $>$ Cs consistent with chromospheric evaporation. We summarize the results for each jet below. Jet 1 is a standard jet with a simple spire. It showed no evidence of a filament, nor evidence of twist in both time-distance plots and spectroscopic observations. However, this jet does show a clear temperature-dependent velocity. We interpret this relationship to be clear evidence of chromospheric evaporation. Because the temperature dependent velocity is clear, with no evidence of twist, chromopsheric evaporation may be the primary accelerator of this jet. Jet 2 exhibits evidence of a filament eruption, and twisted motion along the jet spire, therefore torsional Alfvén waves may be contributing to the acceleration of the jet spire, particularly since this jet did not show strong evidence of CE. The cooler channels in Jet 3 show some temperature dependence, however this trend does not extend to the warmer temperatures since warm channels have velocities consistent across all temperature bins ($\sim$350km/s). These two separate trends suggest that chromospheric evaporation may be a contributor to the acceleration of the cooler components of this jet, but not the warmer plasma. This jet also contained an erupting filament, possibly related to its acceleration. Jets 4 and 5 both show evidence of an erupting filament and twisting/unwinding motions. The a temperature-dependent velocity relationship is not observed. Jet 6 shows a temperature-dependent velocity consistent with chromospheric evaporation, although the trend is not as clear as Jet 1. The velocities of warm plasma are similar, but does show a temperature dependence. The presence of chromospheric evaporation is confirmed for Jets 6, using IRIS spectroscopic observations which indicate no twist in the spire outflow and the possible presence of a reconnection site at the base of the jet. Overall, we find that 2 of the jets have temperature-dependent velocities (Jet 1 and 6) and velocities from 200- 500 km/s consistent with chromospheric evaporation. Figure 2.4. Using IRIS spectroscopic observations we have confirmed the presence of upflows (blue shifted) and downflows(red-shifted) bifurcating near the reconnecting point at the base of the Jet 1 and Jet 6. We interpret these flows to be spectroscopic evidence

of chromospheric evaporation, although additional mechanisms may also contribute. Jets 2-5 all exhibit helical motions along the jet spire, indicating twist, possibly induced by the erupting filaments. We expect torsional Alfvén waves or other mechanisms to be factors in the acceleration of these jets.

Chapter 4

Defining Likely Sites of Reconnection

4.0.1 Results of NLFFF Model

In this work, we complete a through topological analysis of four coronal jets using the Coronal Modeling System (CMS), a non-linear force free topological model visualization tool. As described in Chapter 2, section 2.3, we employ a NLFFF with flux insertion and magneto-frictional diffusion method to model the eruption of Jets 1-4 from Figure 3.1. We calculate the magnetic field using a HMI LOS magnetogram shortly before the eruption. We draw a filament along the magnetic inversion line using AIA 304 and 193 Å images as guide. We run a series of models and compare the topology generated by CMS to features observed in AIA images, such as the jet spire, base and active region loops to find the best fit. For Jet 4, we also compare the magnetic topological evolution to the thermal evolution using the emission measure weighted temperature. For Jets 3 and 4 we have also calculated the Q, or the squashing factor, using a visualization tool developed by [Tassev and Savcheva, 2017]. The squashing factor defines regions where the gradient in the magnetic field is steep, corresponding to enhanced current density. Often these regions are the magnetic null, seperatrix layers, or quasi-seperatrix layers, i.e. regions where magnetic reconnection is likely to occur. In the sections below, we discuss the results of the 3D NLFFF topological model for Jets 1-4.

4.0.2 Topological Model of Jet 1 Observed 10-24-2015

Figure 4.1 shows the result of the 3D topological model for the jet observed 2015-10-24, referred to as Jet 1. This jet was observed on the limb, near the center of an active region. The magnetic structure is simple, thus the spire was modeled using a potential field

model. In this case the potential field matched the jet spire and base, so the flux insertion method was not necessary. Figure 4.1 shows the potential field extrapolation of the jet in 3D view where contours outline regions of field $+/-100$ G (a,b) and 2D view(c). The jet erupts when a negative polarity (green) region emerges, then cancels with a positive(red) polarity flux region, characteristic of the standard jet model presented by [Shibata et al., 1992c, Moore et al., 2010]. Select magnetic field lines (blue and purple lines) show the coronal topology and direction of the jet spire. The total energy $5x10^32$ ergs.

Figure 4.2 shows the SZ cut of the yellow line in 4.1.c. The magnetic field lines (black) trace the jet shape and spire direction at the intersection of negative and positive flux regions and are shown converging to trace the location of the only suspected null point at ~ 5 height units, corresponding to 5.4 Mm above the photosphere. We note that although a potential field model fits this jet best, there must be free magnetic energy in the field in order for the eruption to occur via magnetic reconnection. In addition, it is possible that a filament is present, but too small to be detected. However, since the magnetic model fits the observed jet spire, we expect that the eruption of the filament is not crucial to the formation of the jet and that external reconnection between the jet cusp and ambient corona, is the most likely catalyst in this eruption. In summary, this jet was found to have a simple, magnetic topology with only one magnetic null region, characteristic of the standard jet schematic. The potential field extrapolation was completed and discussed by Natalia Soto [Soto et al., 2016], a summer REU student.

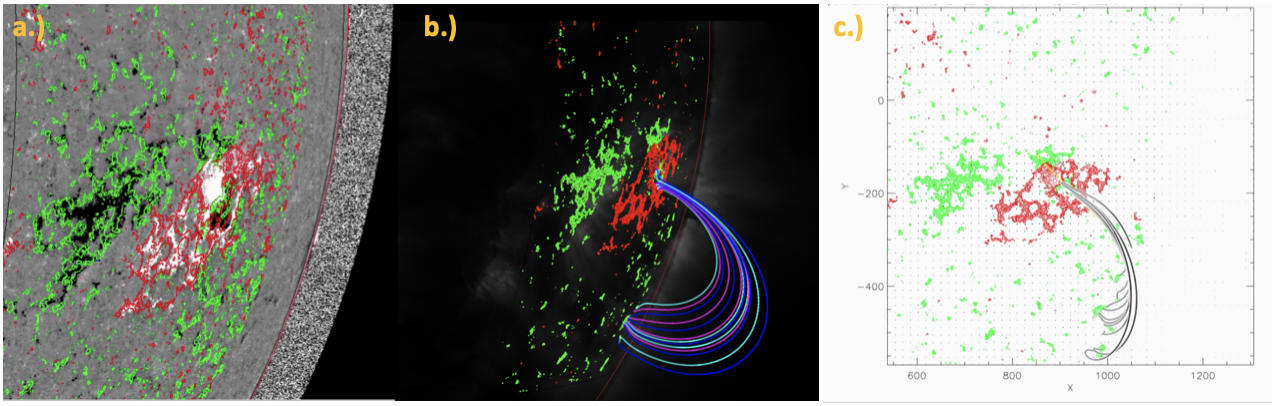

Figure 4.1: Potential Field model of jet Observed 2015-10-24 (Jet 1) in 3D view where contours outline regions of flux $+/-100$ G (a,b) and 2D view(c). The jet erupts when a negative polarity (green) region emerges, then cancels with a positive(red) polarity flux region, characteristic of the standard jet model presented by [Shibata et al., 1992c, Moore et al., 2010]. Select magnetic field lines (blue and purple lines) show the coronal topology and direction of the jet spire.

.

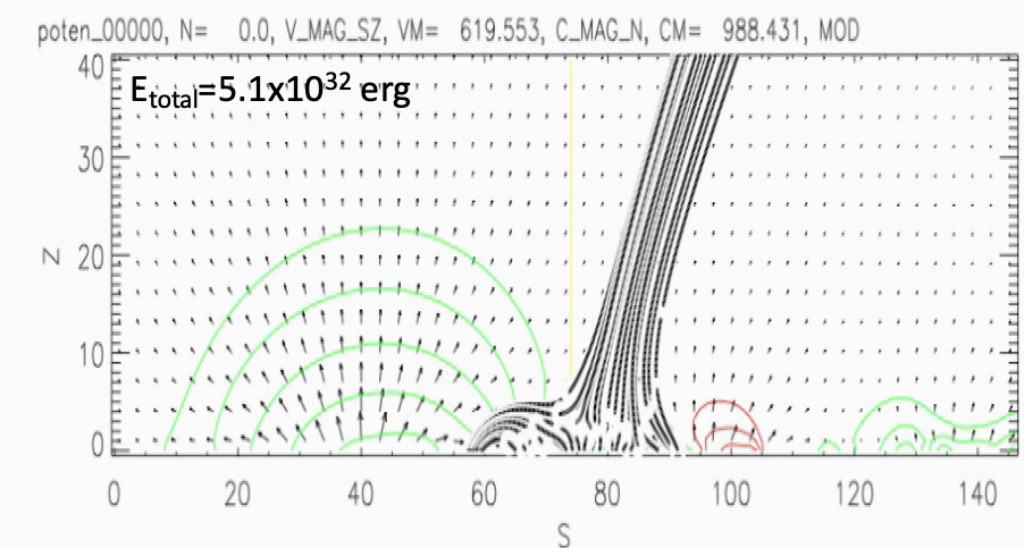

Figure 4.2: Potential field model of jet observed 2015-10-24 (Jet 1) in the SZ plane. The magnetic field lines (black) trace the jet shape and spire direction at the intersection of negative and positive flux regions. Total potential energy for the region is $\sim 5.1\text{x}10^{32}$ ergs.

4.0.3 Topological Model of Jet 2, Observed 2015-01-17

Figure 4.3 shows the NLFFF topological model of the jet observed 2015-01-17 (referred to as Jet 2) with selected field lines. The jet forms in a complex eruption when a small positive (red) polarity region cancels with negative (green) magnetic flux. The jet eruption is affected by 3 filaments; a small one to the upper left (top arrow, labeled F1), the main filament(middle arrow, labeled F2), and a large filament that lies below the AR (labeled F3), pointed out by yellow arrows in Figure 4.4. Selected field lines of the large filament are shown in purple and blue lines in Figure 4.3b-d, tightly wound prior to the eruption. As the eruption evolves, the inner filament begins to rise and the overlying field lines reconnect with the ambient field and the field lines of the lower large filament (c). The smaller upper filament erupts creating a small jet, at same time as the eruption of the main filament and creation of the jet. This scenario is indicative of destabilization of the field by smaller reconnection events taking place above and below the primary jet, often discussed in breakout reconnection models [Archontis and Hood, 2013]. The NLFFF model of this jet was completed and presented by William Wainwright [Wainwright, 2020], a summer REU student for whom I was a co-advisor.

Figures 4.5 a-j shows the evolution of the Jet 2, observed 2015-01-17, eruption in the SZ plane, along the yellow line indicated in 4.6. Two possible regions where magnetic reconnection is likely taking place are identified by yellow (lower region) and blue (upper region) arrows. A magnetic null develops in the lower region as a result of the rising filament, wrapped in tightly wound field lines. The magnetic field lines can be seen converging near $\sim$ 10 height units, corresponding to $\sim$ 10.4 Mm above the photosphere. Simultaneously an outer reconnection region between the field of the large filament and main filament releases twist and straightens as the eruption progresses (blue arrow). This type of 2-step reconnection is characteristic of the model of blowout jets presented by [Sterling et al., 2015, Moore et al., 2018] where both internal and external reconnection can cause the field to re-organize, driven by the eruption of an internal filament.

However the NLFFF model shows that there are two differences in this jet when compared to the blowout/filament model. Not shown in this figure is the effect of the smaller eruption to the north of the jet eruption which helps to destabilize the region and weaken the overlying field. More importantly, the null point (shown by the yellow arrow) does not appear to rise as predicated by the blow-out and filament models, remaining near 10.4 Mm at step 'j'. Instead, twisted field lines appear to peel away. This indicates external reconnection (and possibly a weakened field by the smaller eruption) is driving this eruption, in a scenario which the outer layers open, allowing the filament to escape rather than the rising of the filament and internal tether-cutting scenario, described by [Sterling et al., 2015, Moore et al., 2018]. This type of jet eruption can be attributed to 'break-out' reconnection, except in this case the overlying field is weakened by external reconnection first.

4.0.4 Topological Model of Jet 3 Observed 2012-09-21

Figure 4.7 shows the topological model for Jet 3, a large blow-out jet that erupts in the quiet sun. Prior to the eruption, a small sigmoidal filament is visible in AIA 304 Å. Using this as a guide, we insert a sigmoidal flux rope into the potential field and the result of the flux insertion is shown in Figure 4.7. In this case, we find the best fit stable model with axial flux 2.0x10^{20} Mx and poliodal flux of 5.0 $\times$ 10^{9} Mx/cm shown in blue in Figure 4.7 c and 4.7d.

As mentioned earlier, this jet was also examined by Panesar et al. [2017] in a survey of quiet sun coronal jets. In that study, the authors suggests that this jet forms as a result of the formation and eruption of a small filament. A schematic of the proposed formation is shown in Figure 4.0.4. Magnetic field lines and their associated direction (sign) are shown in black. In their interpretation, a negative polarity flux region sits between two positive polarity regions. The negative polarity flux region cancels with the majority positive flux region, forming a dome shaped inner region (b). Flux cancellation via reconnection very low in the corona (red star in (a)) creates a highly sheared field (black line beneath brown loop in b).

The authors correlated low lying reconnection with short, low bright coronal loops shown in Figure 3.1c. The pink star shows an interchange reconnection in the low corona above the flux cancellation neutral line (c). The blue sigmoid-shaped curve represents a cool-plasma filament. The reconnection between the open and closed field (pink star, b) resulted in the formation of newly open field lines and newly closed field lines (red lines in c), allowing the jet to form. When we compare this interpretation to the results of the NLFFF (see Figure 4.0.4), we find some similarities. A small filament does indeed form low in the corona (Figure 4.0.4b), and its rise due to reconnection occurring beneath it forces reconnection between the region enclosing it (closed lines) and the ambient magnetic field (open field region). The location of the null region in the NLFFF model. Figure 4.0.4c, matches well with the location in the schematic (pink star in 4.0.4b). We also see evidence of the newly closed loop system (red lines Figure 4.0.4c) and those in the NLFFF model (4.0.4c). However, we note that in the schematic (4.0.4b), the primary reconnection region is between the closed field lines of the positive and negative flux region, i.e. the pink star in b, is reconnection the closed field and open field *above the filament*. Instead, we find that the region above the filament is closed, and instead reconnects with the open magnetic field lines 4.0.4. This difference in location is significant because it means that when reconnecting occurs the twisted filament can unwind and escape along the open field as observed in EUV. This notable difference also allows more energy to be imparted onto the jet spire from the twist of the filament, since the magnetic field lines associated with the filament are opening and becoming straightened. The calculation of the squashing factor, Q, in Figures 4.15 highlights this difference by showing that the once closed, twisted field lines, become open during the eruption. This difference shows that rather, than the filament escaping as a single whole entangled mass (similar to a CME), the twisted field lines unravel, transforming potential magnetic energy as thermal and kinetic energy *along* the field, rather than using potential energy to move a large 'mass' or bubble as in the case of a CME. The significance of the unwinding field as a driver in the formation of the jet

found using the calculation of the squashing factor, Q in Figures 4.15 discussed below. In this case, we interpret the filament has a more passive role in the eruption; storing magnetic energy but not driving the initiation of the eruption. In other words, we believe that if reconnection had not occurred between the external open field and the closed field, the magnetic configuration would have remained intact.

4.0.4.1 Correspondence Between Magnetic Topology and Thermal Proprieties

To investigate the correspondence between the thermal properties and magnetic topology we overlay the emission measure with the results from the NLFFF model as shown in Figure 4.13. Emission measure, which is a proxy for density, is shown for LogT 6.0 - LogT 6.3.

Regions of high emission are considered more dense than less bright regions. The field lines calculated from the NLFFF model are shown in blue or purple lines. Interestingly, the field lines associated with the null-point region (marked by a yellow star), can be traced back to regions of high density, as highlighted by the yellow arrows, in Figure 4.13a.

4.0.4.2 Free Magnetic Energy Analysis for Jet 3

Table 4.1 shows the energy calculations for Jet 3 using the flux insertion method. The free energy calculated by CMS is very similar to the free energy measurement taken as the difference between the total and potential energy. Therefore, we only compare the free energy calculated by CMS (referred to as Free Energy -CMS) and the free energy using the calculated method (referred to as Free Energy Calculated) in Table 4.1 for reference. We find that overall the free energy in the system decreases after the start of the relaxation process (model iterations 10K - 90K) however only by a small percentage, $\sim$ 6.7 percentage decrease. Indicating that although free energy has reduced there is a large amount of free energy remaining, therefore it may be possible to fuel subsequent eruptions. We find helicity is declines as the iterations increase. This is expected since helicity would be released with unwinding flux ropes. In a later study, we plan to use helicity to probe the amount of additional energy deposited by twist onto the jet spire.

4.0.4.3 Squashing Factor Analysis for Jet 3

In Figure4.15 we plot the calculated QSL at four iterations steps of NLFFF model, using the method of [Tassev and Savcheva, 2019, 2017]. In the early stages of the jet eruption,

enhanced Q values are observed surrounding the compact, tightly wound flux rope at the base of the jet shown in red in Figure 4.15.1a. As the jet erupts the inner twisted regions began extend and unfold. In Figure 4.15.2a large kink-like structure (pointed out by yellow arrows) can been seen as the filament begins to untwist. Simultaneously an enhanced region of current density appears where there had not been (yellow arrow Figure 4.15.2b. The twist in the filament is transferred to the magnetic field lines, creating the helical eruption 4.15 3a-4a. The regions of current density found at the kink in the twist have dissipated by the peak of the eruption. However, as the kink moves travels along the spire, the enhanced region can again be seen 4.15 3b,4b. We interpret the correlation between the enhanced regions of current density and highly twisted kink, to be evidence of the mostly likely location of magnetic reconnection. The location of the regions can be determined directly from the QSL code. We find that these regions coincide with the magnetic null point shown in Figure **??**b, and regions of enhanced current density shown in **??**b, supporting the idea that this region is the most likely location of magnetic reconnection. In summary, we find a reconnection region below the seperatrix layer, pointing to the location of internal reconnection. As the jet erupts we find that the internal null rises in a helical motion similar to the kink instability and internal breakout reconnection or tether-cutting models predicted by [Antiochos et al., 2002, Antiochos, 1996] and [Moore and Roumeliotis, 1992].

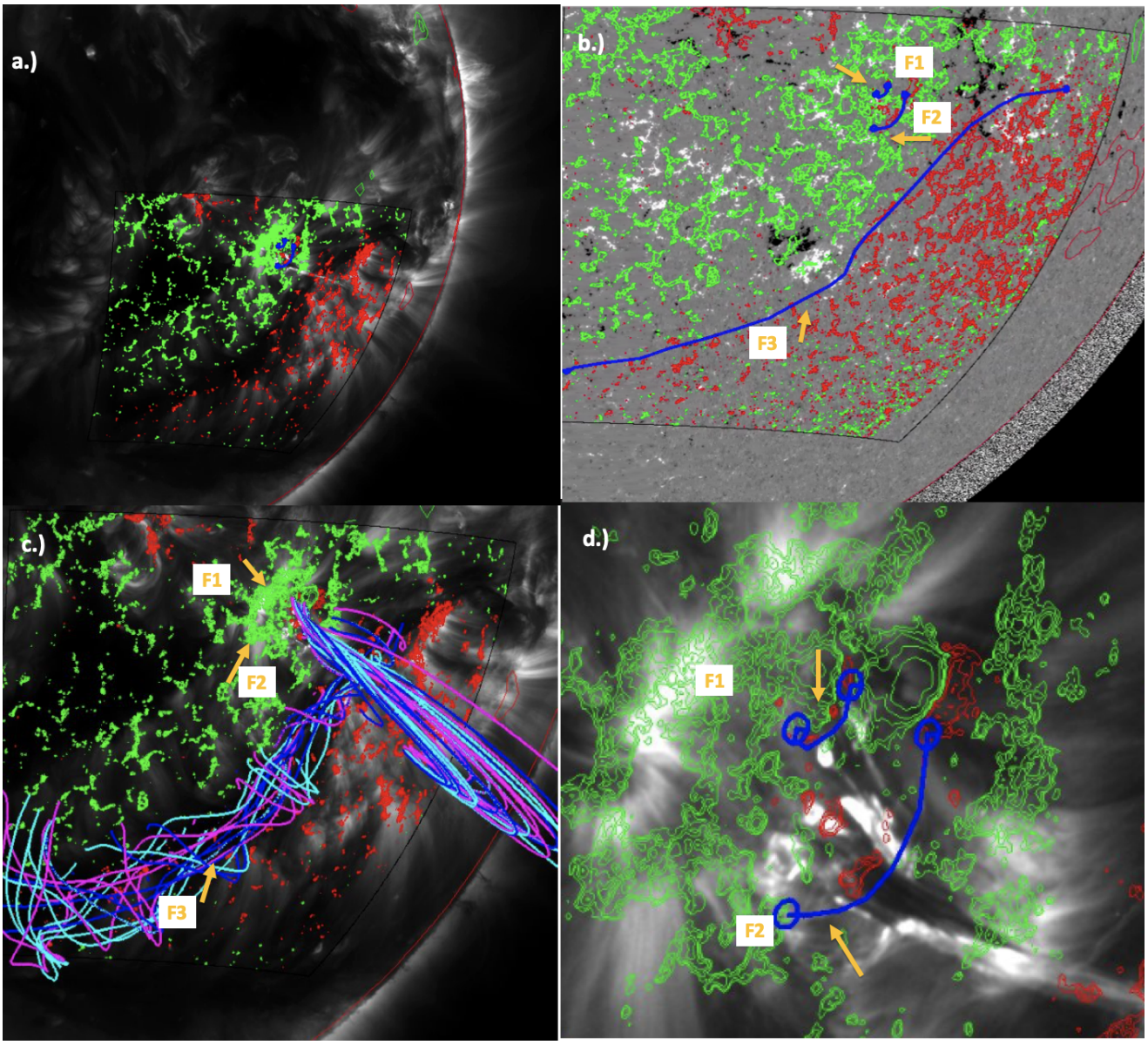

Figure 4.3: Model of Jet 2 observed 2015-01-17. The jet forms in a complex eruption when a small positive (red) polarity region cancels with negative (green) magnetic flux regions in images a-d. The jet eruption is affected by 3 filaments; a small one to the upper left (upper arrow marked by F1), the main curved filament (middle arrow marked by F2), and a large filament that lies below the AR (lower arrow marked by F3) in images b,d and d. The magnetic field of the large filament is shown (purple and blue lines in image c. A close up of just the jet region is shown in image d. The small upper (F1) and primary jet (F2) are visible in AIA 193Å image (black and white background).

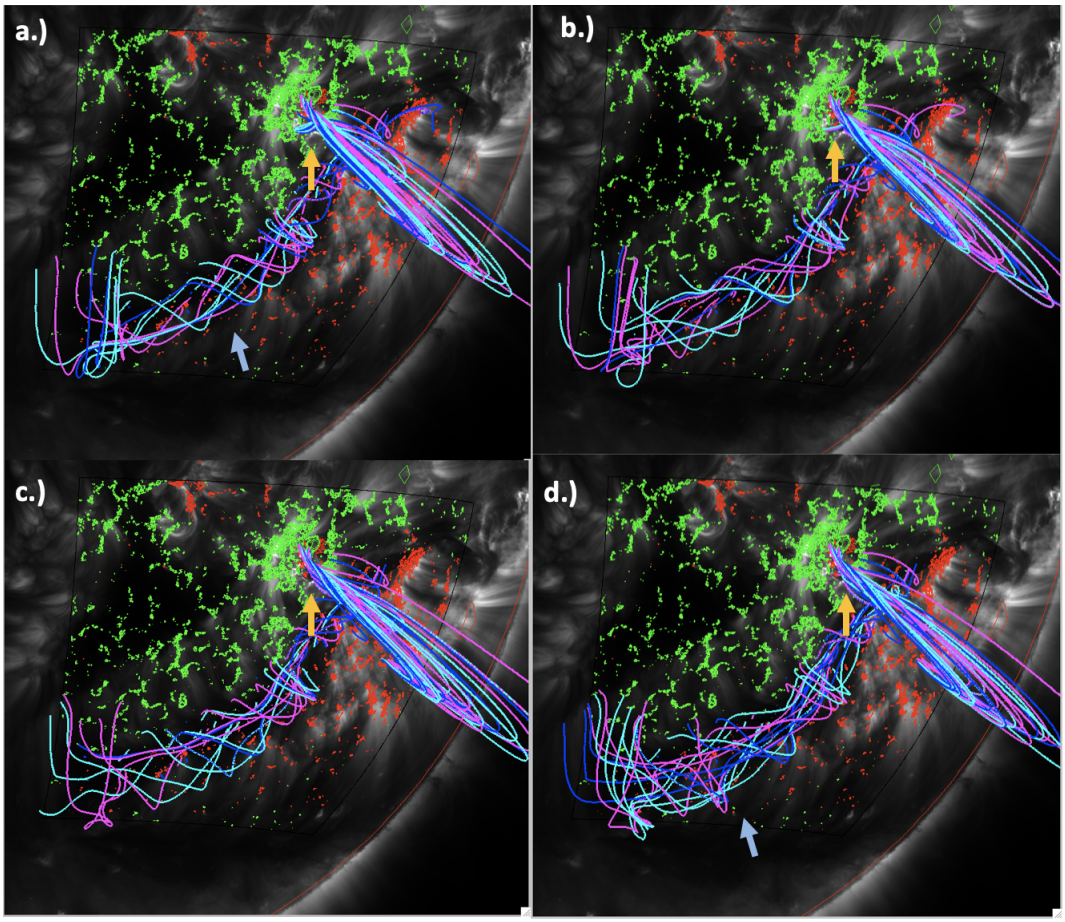

Figure 4.4: The magnetic topological evolution of Jet 2, observed 2015-01-17 with AIA 193Å image in background and overlayed with contours of magnetic flux regions for model iterations 1K, 3K, 5K, 7K,respectively. In the early stages of the eruption magnetic field lines (purple and blue) are tightly wound around the large southern filament and the filament at the base of the jet.As the eruption continues both filaments show a decrease in helicity and null region forms at the base of the jet spire (yellow arrow in a,b). During and after the eruption the field lines appear to unwind until becoming 'smoothed',i.e. less tangled.

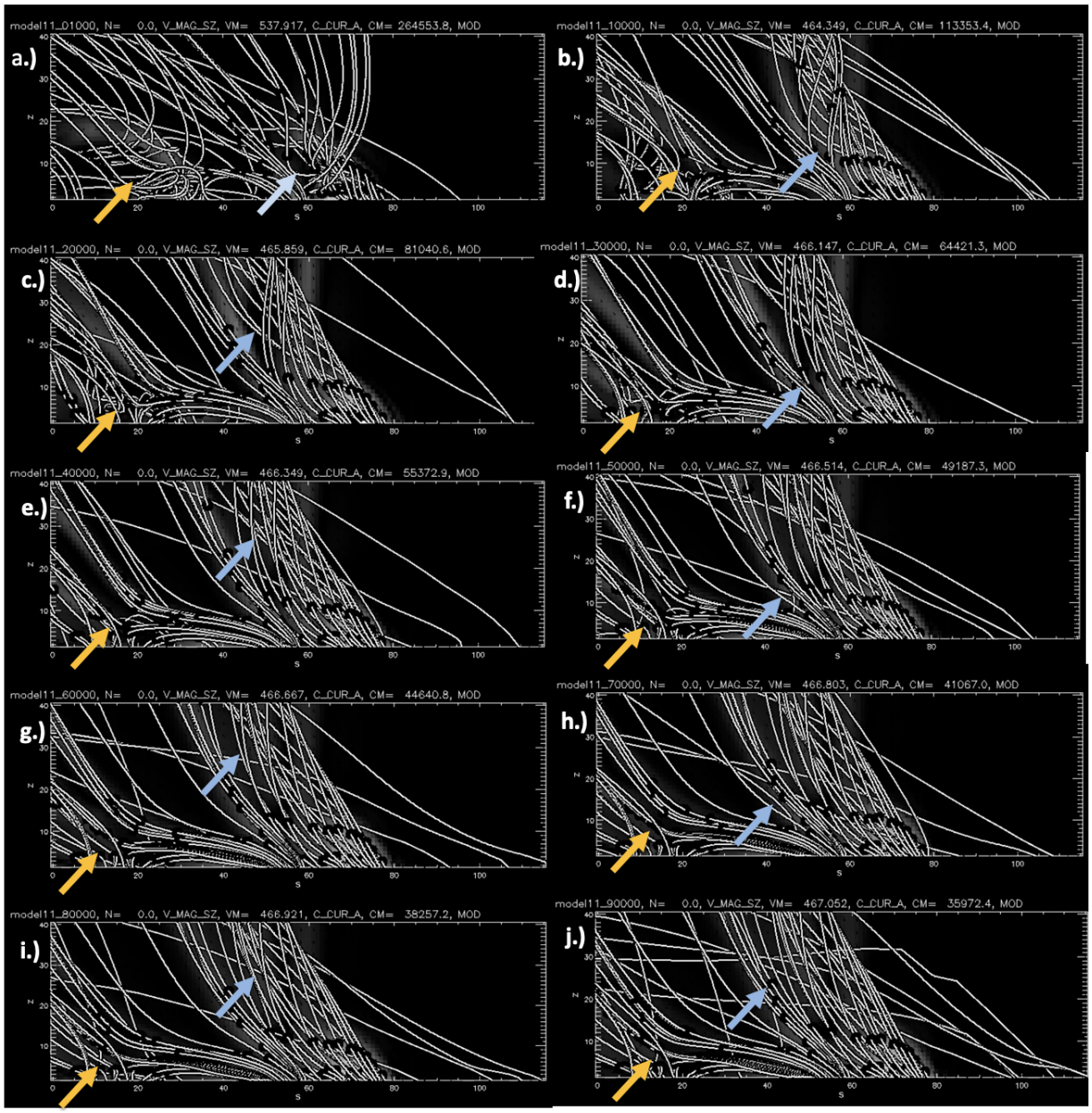

Figure 4.5: Evolution of Jet 2, observed 2015-01-17, in the SZ reference frame corresponding to the slice shown in Figure 4.6 The location of the magnetic null can be seen as a region where magnetic field lines (black) converge. Two possible null regions; a lower (yellow arrow) region where internal reconnection is taking place due to the rising filament, and an upper region (blue arrows) where the field lines of the jet are reconnecting with the field of the larger filament.

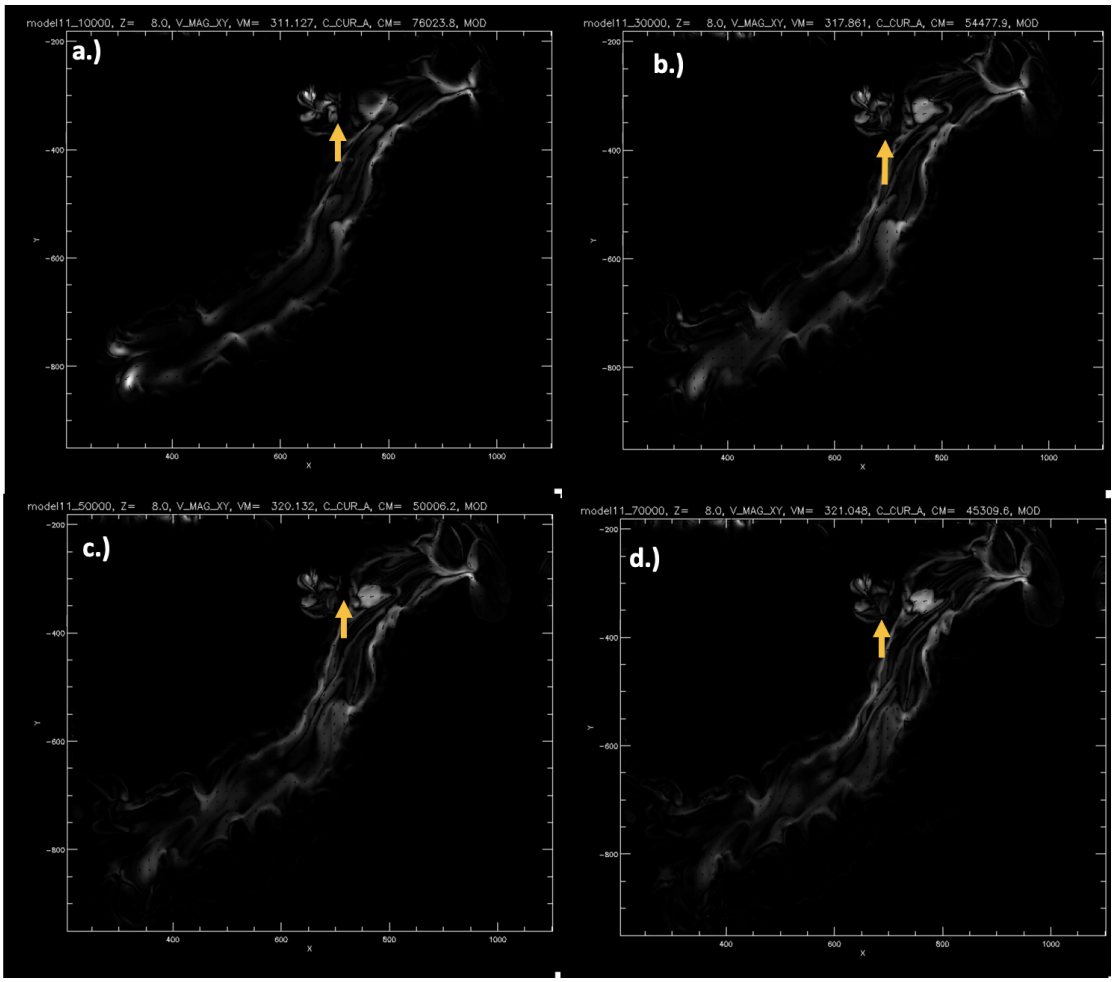

Figure 4.6: Evolution of current density from NLFFF model for Jet 2 observed 2015-01-17 at $\sim$ 4.5 Mm, iterations 1K, 3K, 5K, 7K, respectively. White contours show regions of enhanced current density along the large southern filament and at the base of the jet. A region of enhanced current appears and dissolves coinciding with the appearance of the jet (yellow arrows).

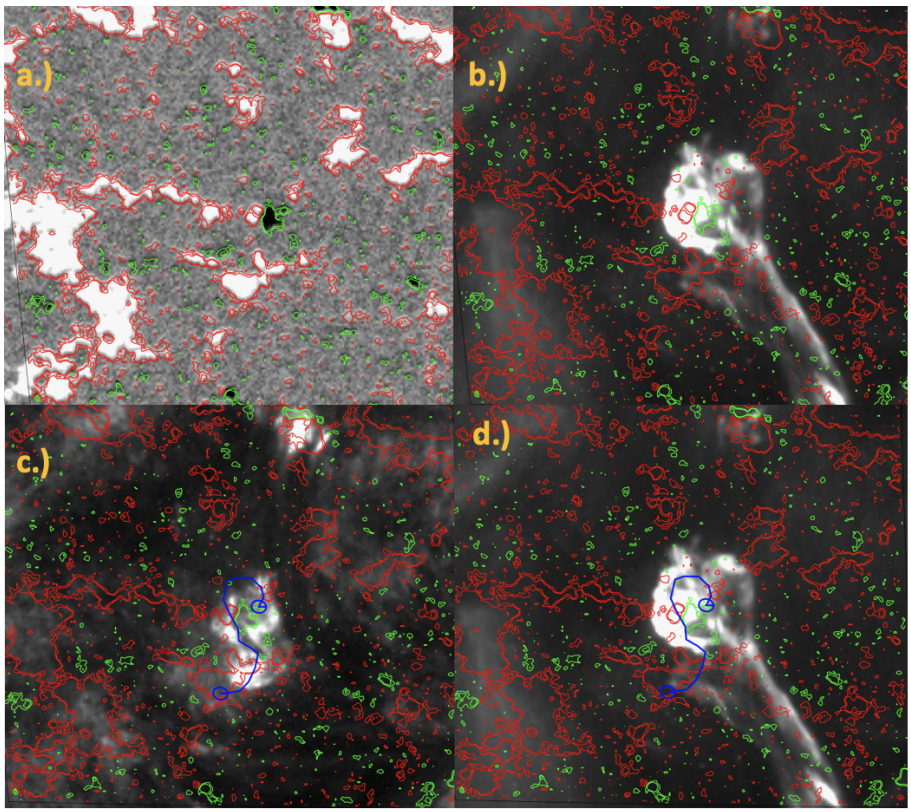

Figure 4.7: The process of selecting a filament for Jet 3, observed 2012-09-21. HMI photospheric magnetogram before the eruption is shown with contours of $-/+$ 50 Gauss. Regions of positive magnetic flux (red contours) and negative polarity flux regions(green contours) are shown over AIA 193 Å image (b-d). The filament (blue line) is selected along the polarity inversion line of positive and negative flux regions. The inserted filament has an axial flux of 1×10^{20} Mx and a poloidal flux per unit length along the length -5×10^{9} Mx

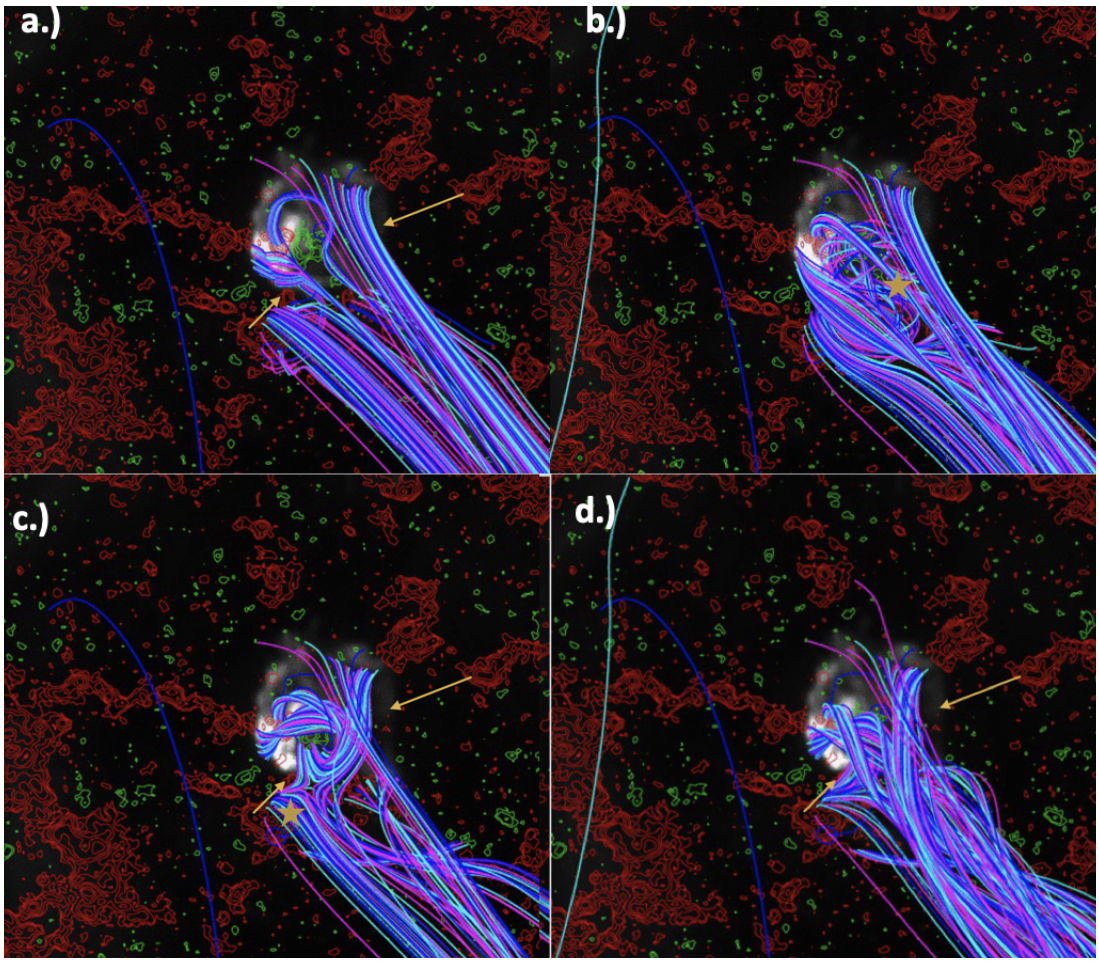

Figure 4.8: NLFFF Model result for Jet 3 observed 2013-09-21. Selected field lines show jet evolution (purple blue). AIA 193Å image of jet near the peak is shown in the background. The most relevant location of magnetic reconnection (yellow star) is between the field enclosing the filament and the ambient open magnetic field lines. Magnetic flux regions of positive and negative flux are shown in red and green contours, respectively

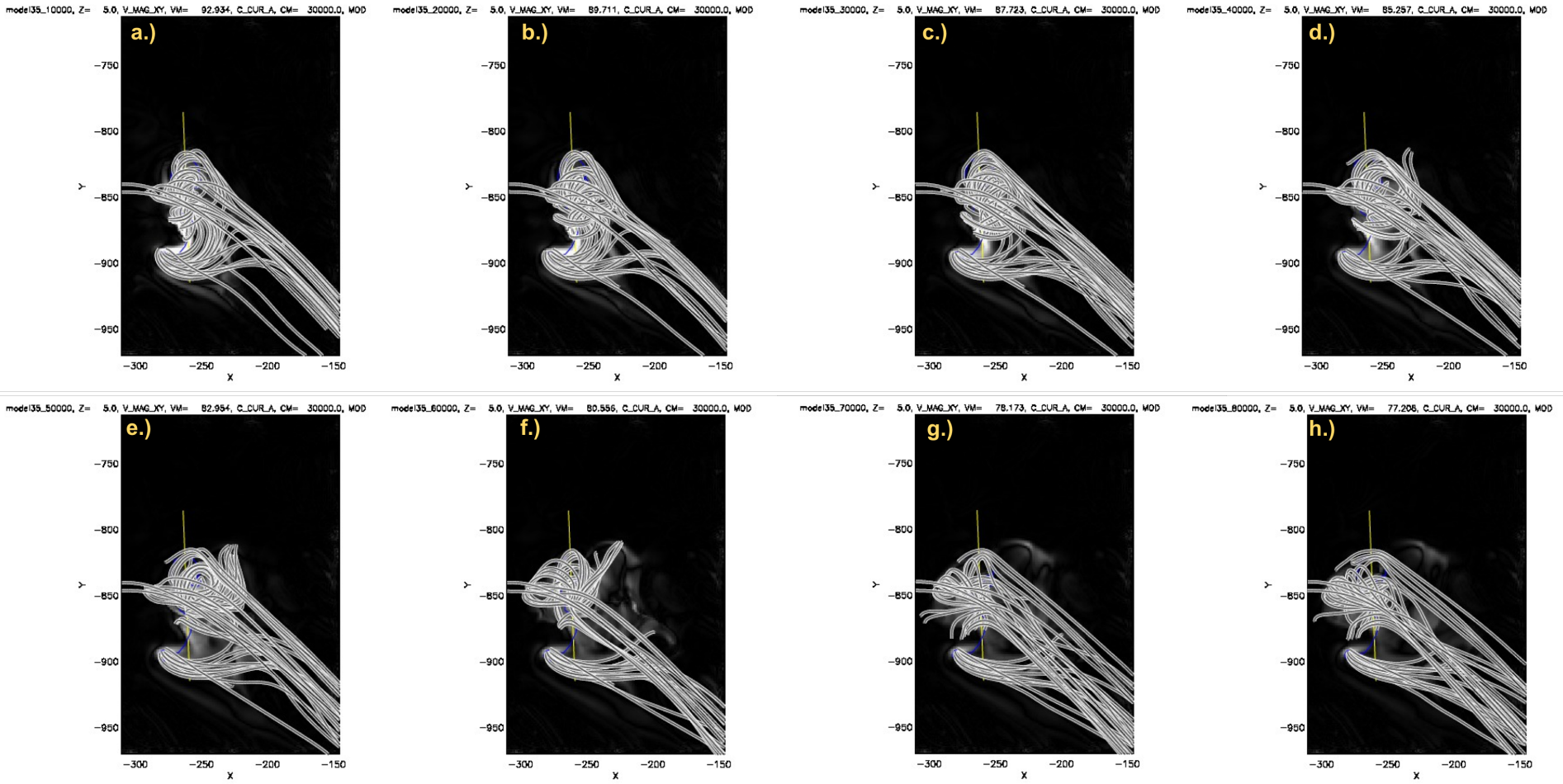

Figure 4.9: Model evolution in XY space for selected iterations for Jet 3 observed 2013-09-21.

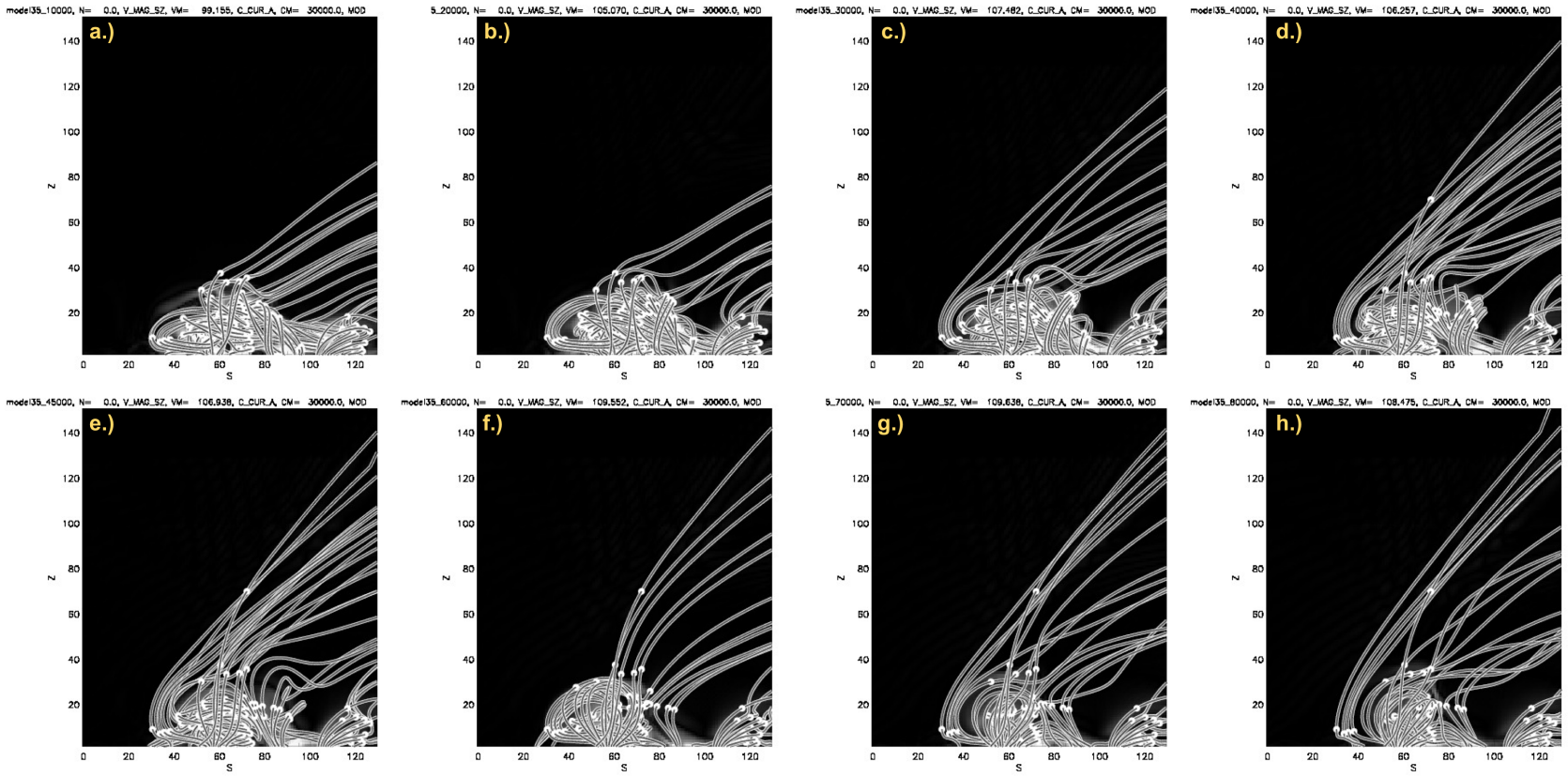

Figure 4.10: Model evolution in SZ space for selected iterations for Jet 3 observed 2013-09-21.

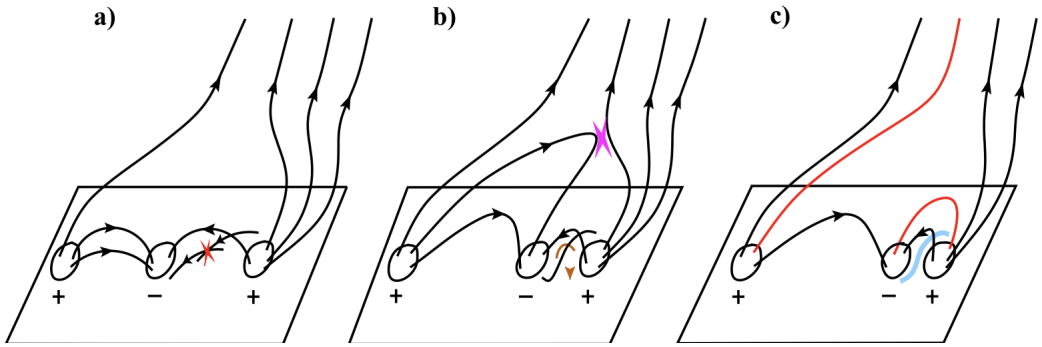

Figure 4.11: Schematic of Jet 3 proposed by Panesar et al. [2017]. In their interpretation of jet formation, a negative polarity region (negative sign on middle circle in a-c) sits between two positive polarity regions. A small filament forms between the positive and negative polarity regions on right (b).. Reconnection also occurs between the closed loop and open magnetic field lines (pink star in b). The new configuration includes closed overlying loops (red) over a small filament (blue line) in figure c.

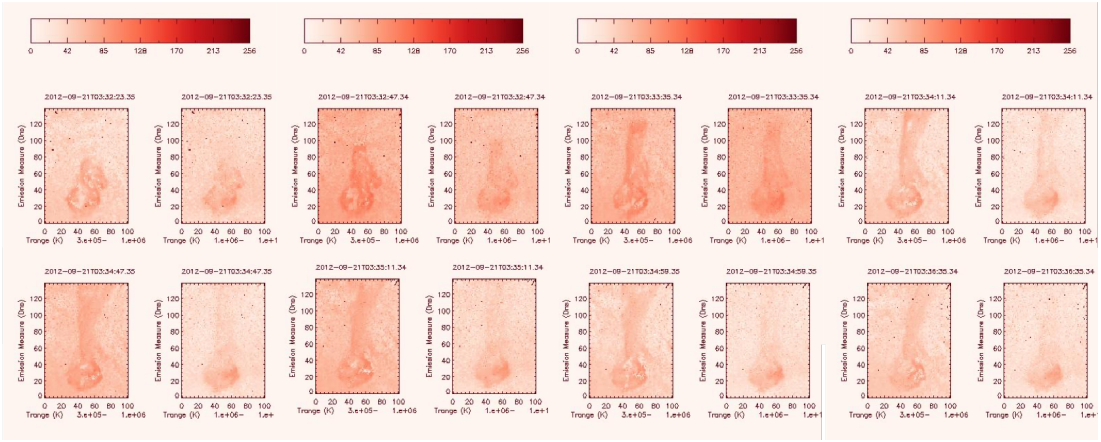

Figure 4.12: Emission measure weighted temperature calculated for the Jet 3, at three times during the jet eruption at 2013-09-21 03:32 UT, 03:33 UT and 03:34 UT. EM is integrated from 3×10^5 MK to 1×10^6 MK (in panels 1a, 2a, 3a) and 1×10^6 MK to 1×10^8 MK in panels (1b, 2b, and 3c), essentially comparing the density of the 'cool' emission that of the 'warm' emission.

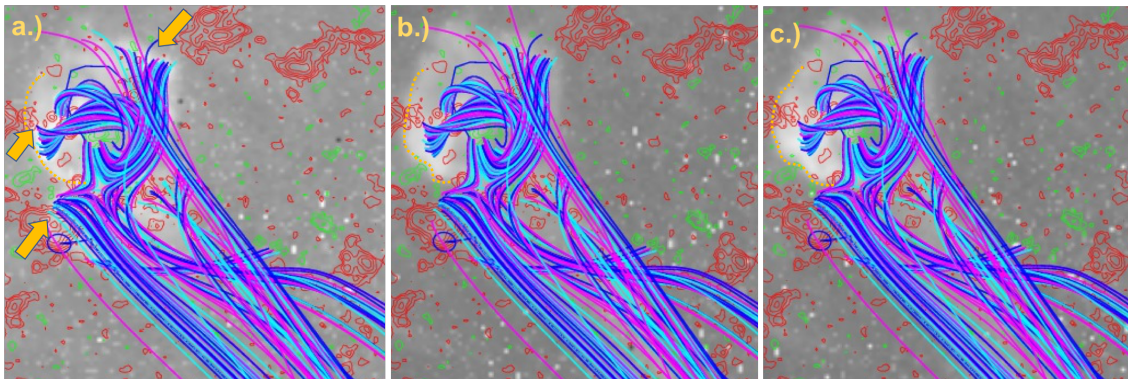

Figure 4.13: Emission Measure calculated from Logt 6.0-6.8 and results of NLFFF model at iteration 60 prior to eruption (Figure, panel c) overlayed. Field lines associated with the null point region, can be traced to footpoints with enhanced density A.) Early in the eruption the field lines are aligned with the outer edge of the jet base B.) As the eruption continues, the outer edge of the jet begins to move outward. C) At Tpeak the outer edge of the jet has moved several km since Panel A.

Model Iteration	**Total Energy (ergs)**	**Helicity**	**Free Energy-CMS (ergs)**	**Free Energy-Calculated (ergs)**
100	3.24E+33	2.51E+43	2.24E+33	2.24E+33
1K	1.45E+33	2.51E+43	4.51E+32	4.51E+32
20K	1.18E+33	2.58E+43	1.77E+32	1.78E+32
30K	1.17E+33	2.60E+43	1.68E+32	1.68E+32
40K	1.16E+33	2.63E+43	1.63E+32	1.63E+32
50K	1.16E+33	2.65E+43	1.59E+32	1.59E+32
60K	1.16E+33	2.67E+43	1.57E+32	1.57E+32
70K	1.15E+33	2.68E+43	1.55E+32	1.55E+32
80K	1.15E+33	2.70E+43	1.53E+32	1.53E+32
90K	1.15E+33	2.71E+43	1.52E+32	1.52E+32

Table 4.1: Free Energy for Jet 3 for each model iteration. Poliodal and Axial Flux used in this model are 5.0 $\times 10^9 Mx/cm$ and 2.0×10^{20} Mx, respectively. The potential energy throughout the relaxation processes is 9.99×10^{32} ergs.

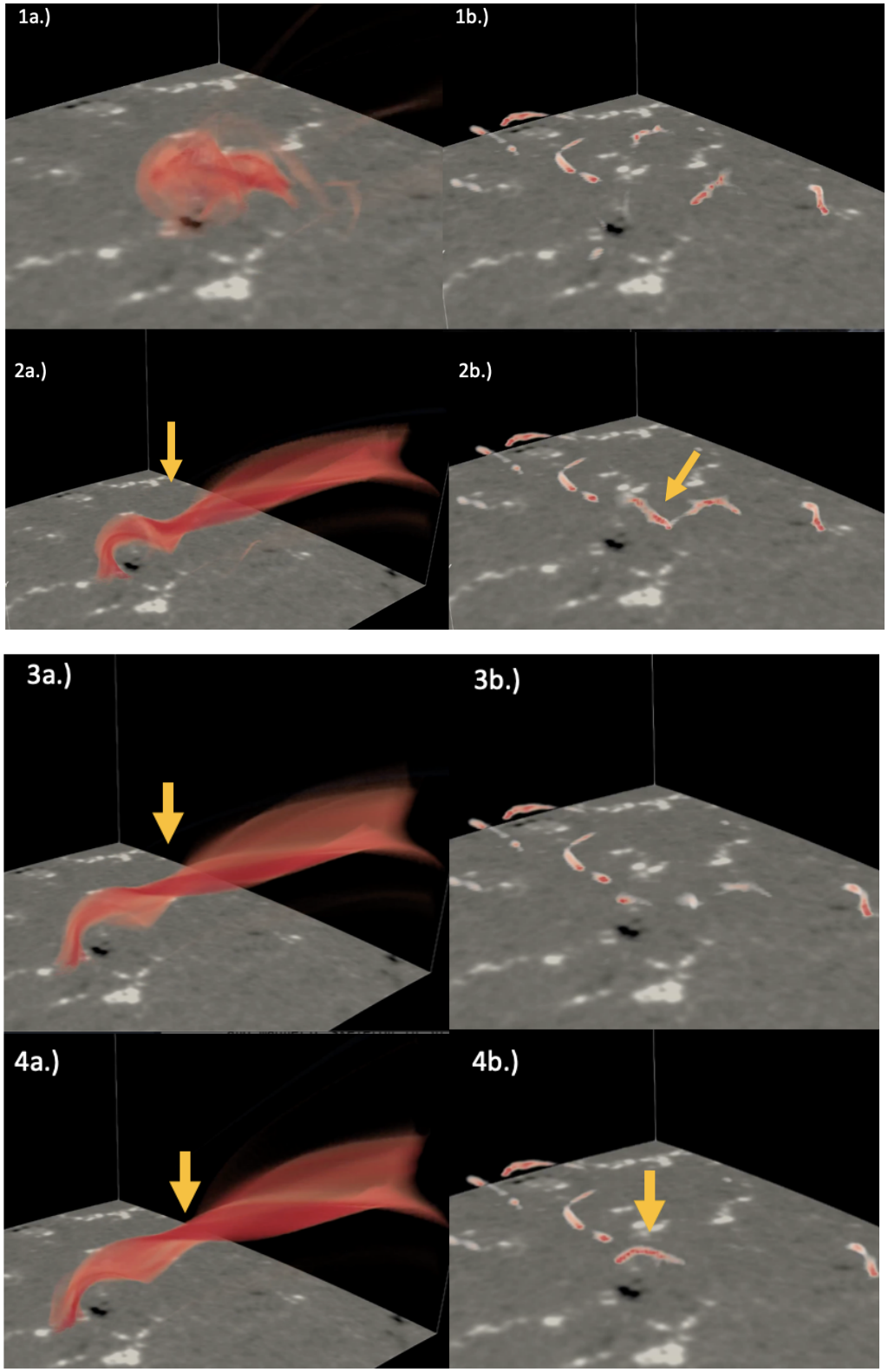

Figure 4.14: Maps of Squashing Factor, Q, for different model iterations.

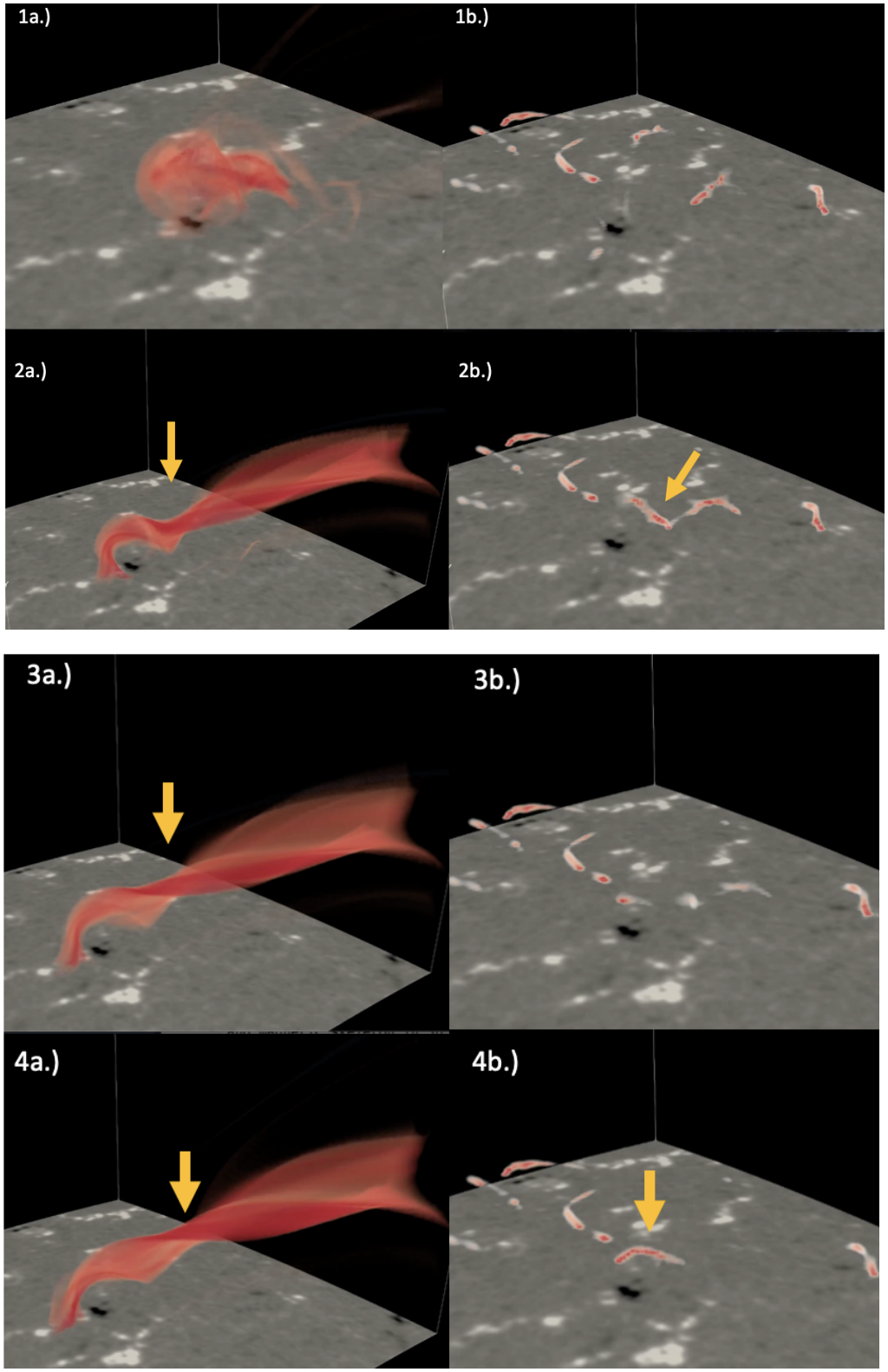

Figure 4.15: Maps of Squashing Factor, Q, for different model iterations.

4.0.5 Topological Model of Jet 4 Observed 2014-11-01

The topological features of Jet 4 were extensively examined by Chen et al. [2018]. In that paper, the authors investigate the source of Type III radio emission associated with the eruption of the coronal jet. Using broadband radio dynamic imaging spectroscopy from the Karl G. Jansky Very Large Array (VLA) Perley et al. [2011], and AIA observations, they are able to map the trajectories of semi-relativistic electron beams to a compact region ($\sim$ 600 km^2) in the low solar corona near the base of Jet 4. For that study, we provided the NLFFF topological model and the associated QSL analysis; the first time the NLFFF model with flux rope insertion has been applied to a coronal jet. The combination of observations and topological modeling showed that the beams of semi-relativistic electrons emanate from behind the erupting jet spire and above the closed arcades, near the region suggested as the most likely source of magnetic reconnection. In the passages below we discuss the NLFF model that supported the QSL analysis presented in Chen et al. [2018]. Figure 4.16 shows the magnetic field and filament selection for Jet 4 observed 2014-11-01. Jet 4 erupts on the periphery of a disk center active region, later named AR12203. In Figure 4.16a, the HMI LOS magnetogram is shown in black in white with contours of $\pm$ 100 G. The jet forms when positive (red) and negative (green) magnetic flux regions merge and cancel (a). The filament path is selected on the polarity inversion line between the two polarities; shown by the yellow arrow in Figure 4.16b. A small number of magnetic field lines (purple and blue in panel c), have been selected to show the magnetic topology of the corona produced by the NLFF model overlapped with an AIA 193Å image near the peak of the jet eruption. The best fit model for this jet traces the jet spire and base (yellow arrows), as well as active region loops observed in AIA. The magnetic field lines show that the jet forms between open (shown as semi-parallel, linear field lines) and closed flux (shown as curved field lines) regions.

In Figure 4.17, we show the evolution of the coronal magnetic field calculated by the NLFFF model at different steps in the relaxation process over an AIA 193 Å image of the

jet at the peak of the eruption. The same magnetic field lines are selected in both panels, at iteration 20K (a) and 60K (b). As mentioned earlier, the NLFFFF model cannot map specific magnetic field lines in AIA. However, by following particular field lines over the relaxation process allows us to map where and how bundles of field lines are changing. The field lines from the NLFFF model show that at the location of the jet, the magnetic topology changes dramatically from open to closed field near the filament, which we will refer to as the primary region (upper arrow in image a), and goes from open to closed near a small negative polarity flux region (lower arrow image a) which we refer to as the secondary region. The NLFFF model shows that the jet may have been formed in a two-step acceleration process described in the passages below.

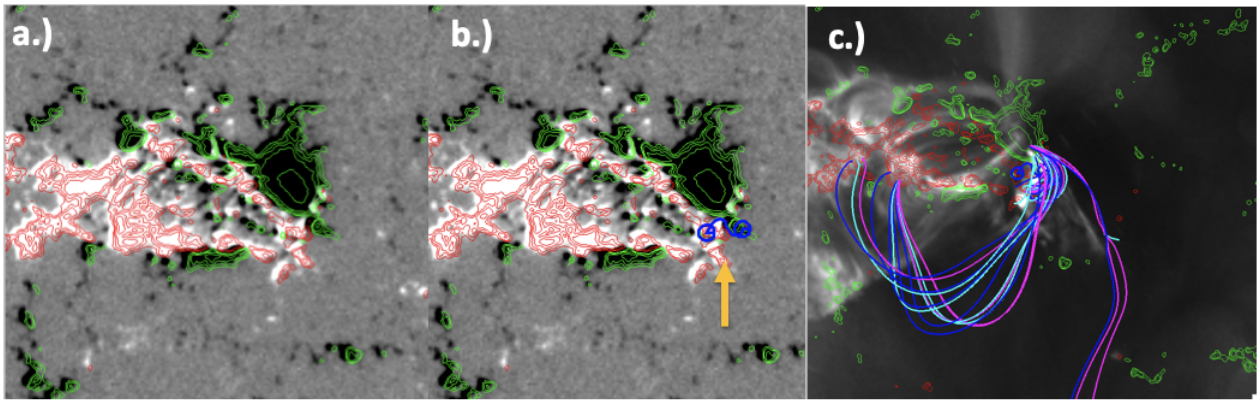

Figure 4.16: Magnetic field and filament path for Jet 4 observed 2014-11-01. The jet forms in a region of positive (red) and negative (green) polarity magnetic flux regions (a,b) on the periphery of an active region between open and closed field regions (c). The filament path is drawn on the based on AIA 304Å observations and HMI magnetograms (black and white background in a,b)

When the jet begins to form, magnetic field lines of opposite polarity come into contact in two regions; one located at the intersection with the open field (pointed out by blue arrow) and one near the intersection with the closed field (pointed out by yellow arrow), as shown in Figure 4.18. The same magnetic field lines from Figure **??**c, are drawn as white lines in Figure 4.18 a-e. The evolution of the magnetic field in Figure 4.18 a-f,shows that both of these regions are relevant in the evolution of this jet. First, the filament (near yellow

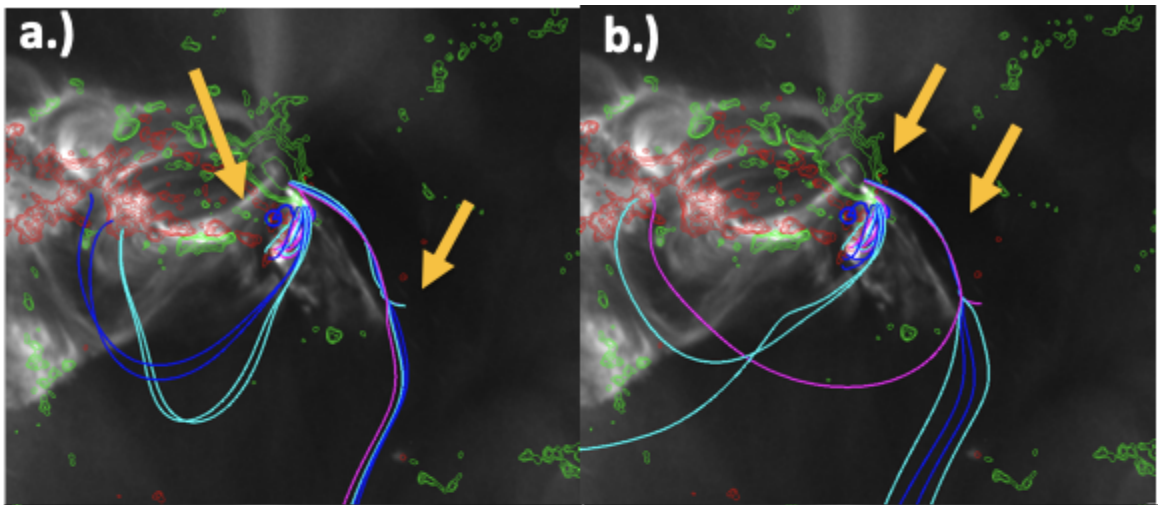

Figure 4.17: Magnetic field evolution of Jet 4 shown increasing number of magnetic field lines (purple and blue) and AIA 193Å image in the background. Positive (red) and negative (green) flux regions are found near the base of the jet. The jet erupts near open and closed regions. The open field lines are shown reconnecting to the closed field during the eruption.

arrow) begins to rise and reconnection occurs between the closed field of the filament, and the closed, but opposite polarity region of the active region (Figure 4.18, image b). This causes the re-organization of the field, and closed field lines were once tied to the active region, are now tied the the second reconnection region (blue arrow in Figures 4.18 c and d). Now, the closed field of the active region extends to the outer region (blue arrow). The filament continues to expand until reaching the outer region (blue arrow) where a secondary reconnection occurs between the open field lines, and the closed field of the new loop system. In Figures 4.18 f - g2, additional field lines are selected to show the evolution of the complex region near the time of the jet eruption (f). After the peak of the eruption, the field again reorganizes, and the field lines of the active region once again closes at the boundary between open and close field (g1, yellow arrow). Figure g2 shows the final configuration after the eruption and now a closed flux region (yellow arrow) is embedded beneath the new active region closed loop system.

Figure 4.19 a-e, shows the evolution of the magnetic field in the SZ direction, taken along the yellow line in Figure 4.18. The same magnetic field lines from Figure 4.18 are

drawn in white. In addition the current density is shown in white in the background of each of the figures. We can clearly see the discontinuous field in the region near the jet filament (primary region, yellow arrow) and the secondary region (blue arrow). The secondary region does not affect the initial eruption, but will impact the eruption later. We interpret these regions to be the most likely location of magnetic reconnection associated with the jet eruption. In Figure a-b, the closed loop system of the filament can be seen rising and reconnection with the open field. A magnetic null point and region of enhanced current density are located near the yellow arrow in Figure 4.18b. As the eruption progresses these same field lines are shown to be tied to the lower region (blue arrow c and d), demonstrating the reconfiguration of the magnetic field. In the final stages of the jet, the secondary region becomes relevant and the discontinuous field and magnetic null are located near the blue arrow (d,e). The resulting configuration (f-g2) are shown with additional field lines drawn (same as Figure 4.18 f-g2). There are two regions, the inner closed loop system, and the highly curved overlying closed loop system, and a seperatrix layer (g2) between the two regions; a topology that could support subsequent eruptions.

The magnetic topological evolution of Jet 4 is significant in two ways. First, the NLFFF topological model shows that the jet evolves in a two-step reconnection process. Jet 4 was associated with the first observation of semi-relativistic particles emanating from a coronal jet Chen et al. [2018]. The 2-step reconnection and acceleration supports the idea that particle velocities could have been enhanced in both regions, resulting in atypical velocities. Next, the final topology (Figures 4.18 and 4.19 g1, g2) shows the new magnetic field configuration contains an extensive seperatrix layer, making it likely that subsequent eruptions will occur. This active region was associated with several C1.4 - C1.7 class flares 8 days later, from 11-09-2014 at 20:35 UT to 11-10-2014 19:54 UT. Unfortunately the base of the AR and its associated sunspots were already around the limb and not visible during the eruption. Still, we will able to follow the evolution of the region, up to 1 day before the flares begin. In future work, we intend to continue field relaxation to determine if additional

eruptions occur and the resulting configuration.

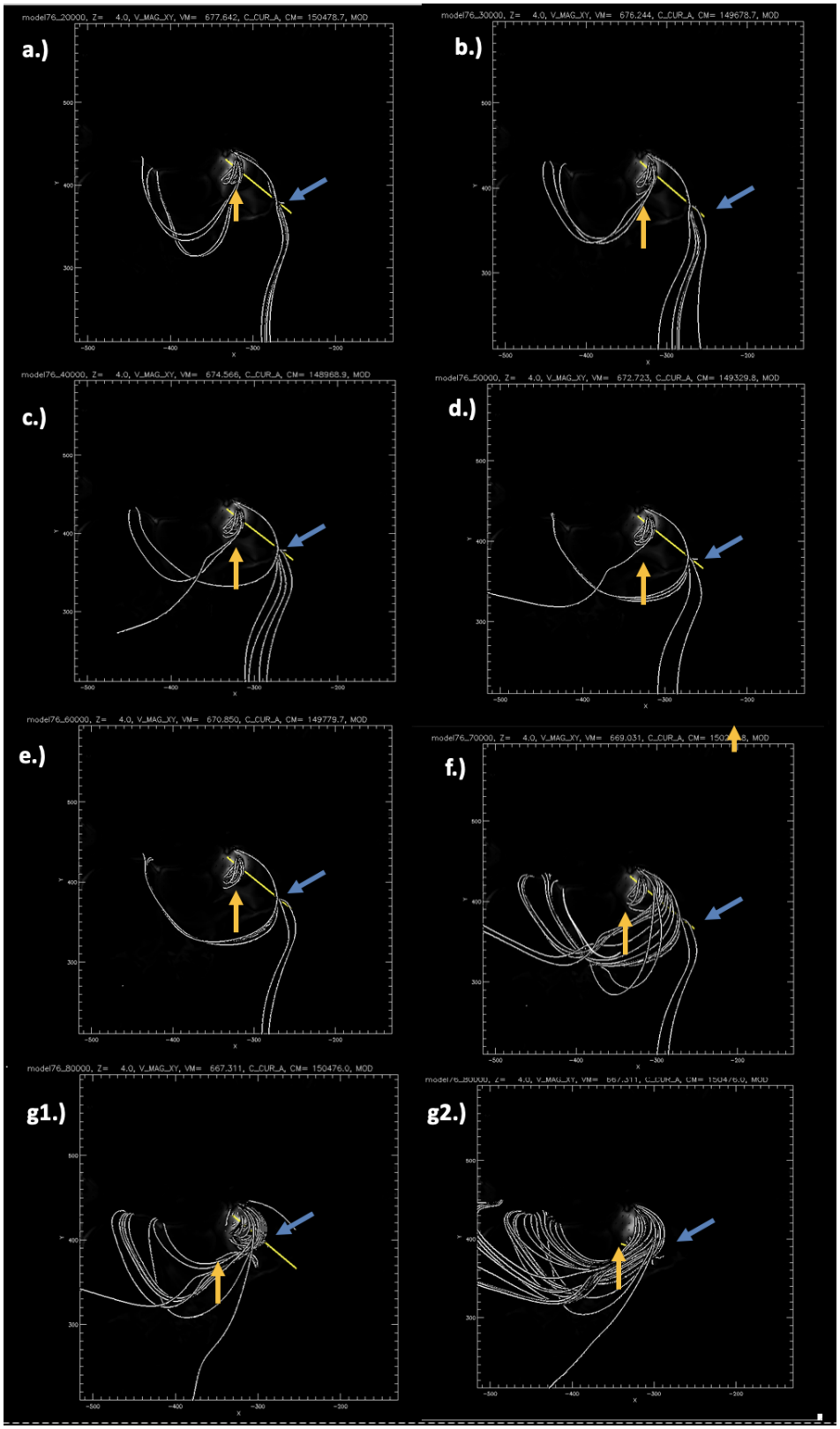

Figure 4.18: Evolution of Jet 4 in XY. Selected magnetic field lines (white) are drawn. The jet is the result of reconnection of a filament at its base (yellow arrow) and a secondary reconnection with a small closed field region (blue arrow).

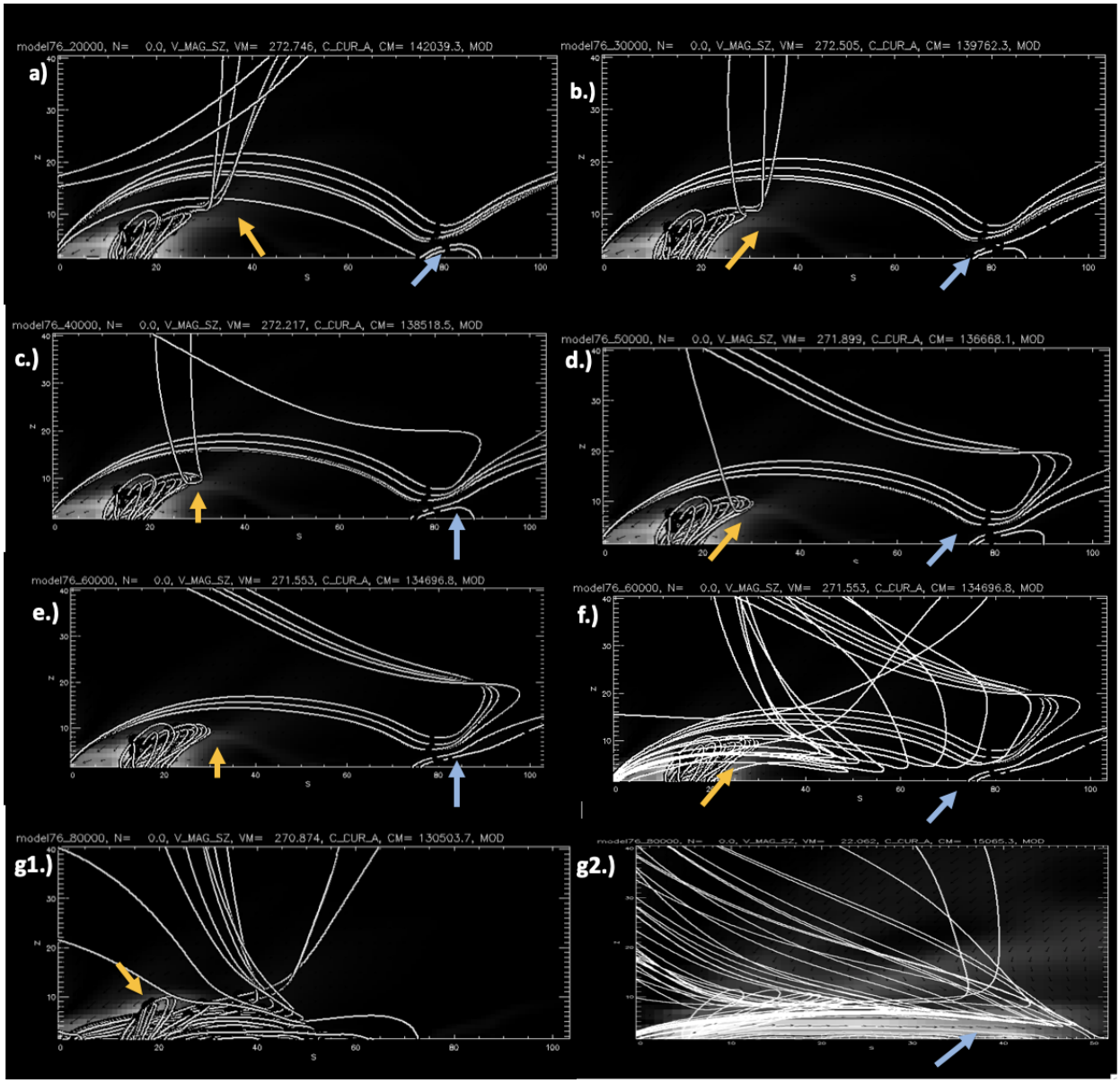

Figure 4.19: Magnetic field evolution of Jet 4 along the yellow slice in Figure 4.18a,b. Three reconnection features are observed in the jet evolution. Internal null (primary region) shown by yellow arrows, external null (secondary region) show by blue arrows, a and seperatrix surface, pointed out by yellow arrow in g1 and blue arrow in g2. The internal null (primary region) a-g1, and the seperatrix surface (g2) corresponds to regions of enhanced current density (white).

4.0.5.1 QSL Analysis for Jet 4

In the passages below we discuss the QSL visualization analysis presented in Chen et al. [2018] based off of the NLFFF model discussed above. In that paper, authors use a combination of observations and topological modeling to show that beams of semi-relativistic electrons emanate from a compact region at the base of the jet spire, in a region where reconnection is most likely occurring (referred to as the primary region in section above). In Figures 4.20 and **??** we plot the calculated QSL visualization four iterations steps of NLFFF model, using the method of [Tassev and Savcheva, 2019, 2017]. Both of these images are presented and discussed in detail with respect to the electron beam in Chen et al. [2018]. Here I discuss the implications of the QSL results for determining the topological evolution responsible for the formation of Jet 4. Figure 4.20 show the results of the QSL for Jet 4. The secondary region is not pictured in this QSL analysis. During the eruption process the flux rope interacts with the ambient field and forms a reconnection feature (orange field lines in Figures 4.20 (middle,right).The red parallel lines in (right) show the source of the semirelatvistic electron beams discussed in Chen et al. [2018].Early in the eruption, the region enclosing the filament (white region left) image, begins to rise, causing reconnection between the open (black lines) and closed regions. The reconnecting field lines are shown in orange. The once closed field lines can be seen opening allowing the jet to erupt and the inner region to continue to expand. Near the jet peak Figure 4.21 , the field lines of the underlying region, are shown unraveling and continuing to reconnect withe the upper region. The location of the vertical lines in **??** right image, are shown by red stars. In this case, the orange field lines in the Figures correspond to the quasi-seperatrix region shown in the NLFFF model in Figure 4.19g1 and g2. The white region in Figures 4.20 and 4.21. After the field lines reconnect, they recoil transferring magnetic tension into heating, resulting in enhanced emission in EUV and and heating along the newly closed loops. Thus the formation of Jet 4 supports the blow-out jet scenario of formation due to internal reconnection and an erupting filament as suggested by Shimojo et al. [1996], Moore et al.

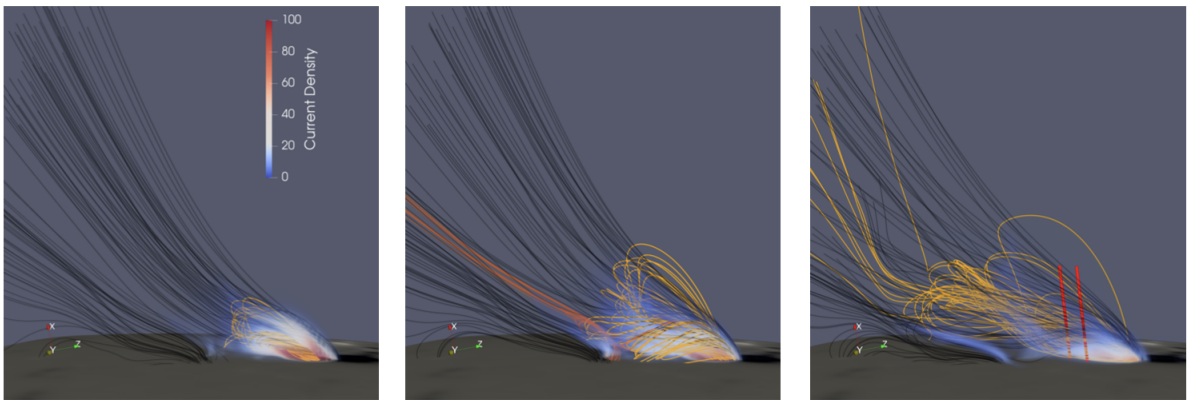

Figure 4.20: Results of QSL visualization for Jet 4, observed 2014-11-01. The regions of enhanced Q are locations where magnetic reconnection is most likely to occur, corresponding to magnetic nulls and high energy particles (red line). Figure from [Chen et al., 2016].

[2010], Sterling et al. [2015].

4.0.6 Discussion of Free Magnetic Energy for Jet 4

As mentioned previously, the CMS algorithm also calculates free and potential energy in the HRES region. Table 4.2 summarizes the parameters found for the eruptive models for Jet 4. Similar to Jet 3, free energy calculated by CMS is very similar to the free energy measurement taken as the difference between the total and potential energy. Therefore, we only compare the total energy calculated by CMS and the free energy calculated by CMS. In Jet 4, the free energy only decreased a small amount (.17 percent decrease), while the total energy showed almost no change, supporting the idea that the magnetic configuration can fuel subsequent eruptions.

4.0.7 Summary of Topological Analysis

In this work, we have used a Non-linear Force Free Model with the flux insertion method to model the coronal magnetic field of four coronal jets. Jet 1, was found to have a simple magnetic topology, appropriate for potential field extrapolation. Magnetic reconnec-

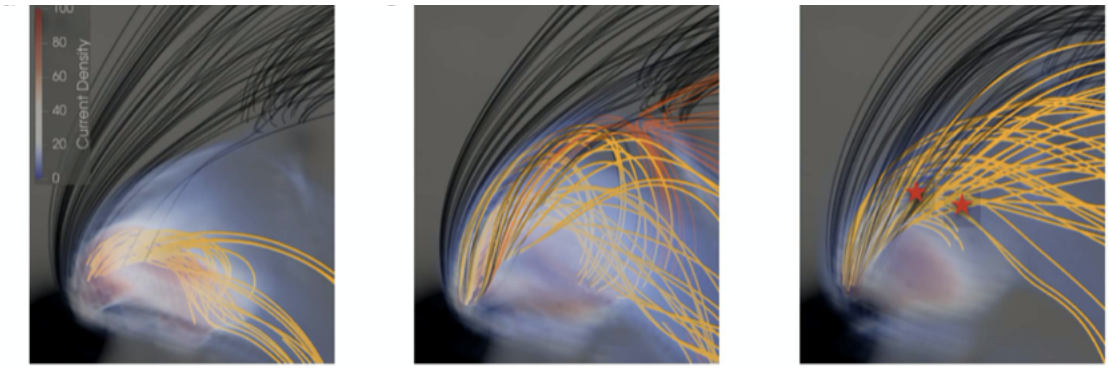

Figure 4.21: Results of QSL visualization for Jet 4, observed 2014-11-01. The regions of enhanced Q are locations where magnetic reconnection is most likely to occur, corresponding to magnetic nulls and high energy particles (marked with black star). Figure from [Chen et al., 2016].

Model Iteration	Total Energy (ergs)	**Free Energy (ergs)**
10K	4.20E+30	-2.89E+31
20K	4.19E+30	-2.89E+31
30K	4.18E+30	-2.89E+31
40K	4.17E+30	-2.89E+31
50K	4.17E+30	-2.89E+31
60K	4.16E+30	-2.89E+31
70K	4.15E+30	-2.90E+31
80K	4.15E+30	-2.90E+31
90K	4.14E+30	-2.90E+31

Table 4.2: Free Energy for Jet 4 for each model iteration. Poliodal and Axial Flux used in the model are -5.0 $\times 10^9$ Mx / cm and 1.0×10^{20} Mx, respectively. The potential energy throughout the magnetofrictional relaxation process is 3.31×10^{31} ergs.

tion is likely occurring externally, where the jet base meets the ambient corona, resulting in a canonical standard jet. In Jet 2, the jet eruption correlated with the ejection of a S-shaped filament, whose spire direction was influenced by a large filament to the south, and a small filament directly northward. We applied the flux-rope insertion method using 3 filaments to identify regions where magnetic reconnection is likely to occur. Interestingly we find that the bundled flux rope, does not initiate the ejection as it does not rise as described in MHD models of filament eruptions. Instead,the outer layers of the external jet cusp are pealed away via external reconnection, and further destabilized by a small erupting jet north of the main jet. In this case the eruption is caused by external reconnection and a weakening outer dome, thus allowing the filament to escape, rather than the upward force of the filament and tether-cutting reconnection. Jet 3, was previously discussed by [Panesar et al., 2016], and was found to be the result of magnetic flux cancellation in the quiet sun. A curved filament is visible in EUV and thus we employ the flux-insertion method to study the magnetic topological evolution. We also calculate the emission-measure weighted temperature of the jet and trace the magnetic field topology from the NLFFF to regions of enhanced density and heating in the temperature maps. For the first time, we can associated the magnetic field topology of the null region, to regions of enhanced density and heating. Furthermore, we observe the outward motion of field lines similar to post-flare ribbon loop expansion observed in solar flares. We also calculate the squashing factor, Q, to locate regions of enhanced current density and discontinuities in the magnetic field. We find correlations with the appearance of QSL and the eruption of the jet, near the same location in the topological model, thus supporting the idea that this jet formed as a result of internal reconnection. Jet 4, was discussed in a prior work by [Chen et al., 2018], where we used the flux rope insertion method to model the active region jet. In that study, we found that the jet forms as the result of the eruption of a small filament, but is accelerated in a two-step reconnection process where it is accelerated both at the base, and again by a small flux region in the spire path. We also calculate Q, for this region and find strong correlations between the

magnetic null regions and regions of enhanced current density and heating in EUV images. We analyze the free magnetic energy associated with Jet 3 and Jet 4, and found that free magnetic energy and helicity are correlated as expected. Furthermore, each of these regions experience a loss of free magnetic energy, however the percentage is small, possibly indicating enough free energy for further eruptions. Indeed several of the jets occurred in regions were homologous (repeating jets) were found.

Chapter 5

Discussion and Future Work

Coronal jets are energetic, small-scale eruptions characterized by a culminated spire, bright dome-shaped base, and magnetic flux emergence, cancellation or other notable changes in photopsheric flux. Although coronal jets, specifically, EUV and X-ray jets, have been studied extensively, a complete picture of their initiation and acceleration mechanisms has not been found. Current models of jets present 2, informal categories based loosely on their morphology, and speculation on the location of magnetic reconnection. Namely, 'standard' jets, are associated with narrow spires, simple magnetic topologies, and are thought to form via external reconnection, when one polarity region emerges or cancels with a flux region of the opposite polarity. Conversely, blow-out jets are thought to form when internal reconnection (with or without external reconnection) frees tightly wound flux tubes, via tether-cutting reconnection, causing a much more complex eruption of cool and warm plasma. In each of these scenarios, erupting jet plasma can be accelerated by a number of different mechanisms working in tandem or independently. The most commonly discussed are release of magnetic tension resulting in the sling-shot of plasma, the deposition of energy from twist and/or propagating torsional Alfvén waves, and acceleration due to the pressure gradient created by suddenly heating chromospheric plasma, known as chromospheric evaporation. Each of these mechanisms present observational clues that can be tested and used to verify and eliminate jet models. Here we present a novel approach developed to determine if chromosphere evaporation is responsible for jet acceleration by calculating jet velocity as a function of temperature. Furthermore, we identify if twist or filaments are present, indicative of torsional waves. Finally we model the magnetic topological structure of four jets, to identify regions where magnetic cancellation could occur. By combining observational tests with topological modeling, we can better identify the

initiation and acceleration mechanisms for jets.

Jet 1,observed 10-24-2015, was found to have a simple magnetic topology resulting from flux cancellation, with only one region where the magnetic null would be located. A filament was not visible and a potential field model was found to fit the jet spire and dome when compared with AIA 193Å observations. Thus, we interpret this to indicate that the jet follows the canonical, standard jet model (discussed by Moore et al. [2010]), where magnetic reconnection occurs between the external field of the jet base and the ambient corona. A filament was not visible and verified by the lack of twist found in the jet spire in both AIA data and IRIS spectroscopic observations. Instead, we find evidence of plasmoids, indicative of magnetic reconnection. Furthermore, this jet was found to have a clear temperature-dependent velocity, within 2.35Cs, characteristic of chromospheric evaporation. Thus we conclude that the primary acceleration this is chromospheric evaporation, when external magnetic reconnection drives jet initiation. Using IRIS spectroscopic data, we identify the possible location of magnetic reconnection, based on relatively large enhancements in non-thermal width and Doppler velocity. We speculate that the sling-shot mechanism, may be applied here, but it may not be as impactful as chromospheric evaporation, particularly since the magnetic flux regions associated with the jet are small, compared to the other jets in this study.

Jet 2, observed 2015-01-17 is a blow-out jet that forms on the periphery of an active region and a large filament, as a result of magnetic flux cancellation. By examining the relationship between velocity and temperature, jet we find three of the cooler channels (193 and 94c and 171) have a temperature-dependent velocity, but this trend does not apply to the warmer channels, thus chromospheric evaporation may only contribute partially to the eruption. The jet is associated with the eruption of a large filament with oscillatory signatures at periods of $1-2$ minutes, possibly indicating the presence of torsional Alfvén waves. The magnetic topology of Jet 2 revealed a complex eruption influenced by a large filament in the south, small filament northward, and a the eruption of an S-shaped filament at its

base. Because of the large filament associated with this eruption, we expected to find evidence of internal reconnection and tether-cutting, as in the blowout-jet scenario, however instead we find evidence of external reconnection where the filament escapes, rather than drives the eruption. Therefore, we conclude that magnetic tension, along with destabilization of the overlying field may be the primary acceleration mechanisms. Although we did not find a singular velocity as a function of temperature (as expected from magnetic dominated acceleration), the spread of temperatures is narrow. Their similarities appear to hint a the expected temperature distribution. A study that uses narrow bands of temperature, for instance spectroscopic observations or by calculating the velocity of emission measure weighted temperatures over a narrow range, could validate this theory.

Jet 3, is best described as a blow-out quiet-sun jet. The temperature and velocity of Jet 3 appeared to show an inverse relationship, indicating that chromospheric evaporation is not a contributor to acceleration. A signature of the hot and cool component of the jet ws found as discussed by previous authors [Shimojo et al., 1996]. Jet 3 was found to also be associated with an eruption of a large filament and signatures of oscillatory behavior of a period of $\sim$ 4 minutes. This jet was previously discussed by [**?**] as part of a survey of quiet sun coronal jets. In that study, the authors find that magnetic flux cancellation leads to the formation of a small filament, which inturn erupts due to internal magnetic reconnection. In this work, we show no evidence of chromospheric evaporation and concluded that the acceleration mechanism was more likely related to the mechanical force from retracting reconnecting lines, often called 'sling-shot' mechanism. Using the NLFFF, flux-insertion method we have modeled the 3D topological structure of the coronal jet. We find three probable locations of external magnetic reconnection (magnetic null points) with the open field and one internal reconnection region. As the jet erupts we show that the internal null rises in a helical motion as a consequence of kink instability and breakout reconnection predicted by [**??**]. The topological model agrees well with the blow-out jet configuration shown in [Meyer et al., 2019]. For the first time in coronal jets,

we find trace the magnetic field lines near the internal null point to their foot-points, and find outward motion of dense plasma similar to the motion of flare ribbons during an active region flare. We interpret the presence of outwardly moving dense material to be possible evidence of chromospheric evaporation. However, the velocity-temperature relationship does not indicate CE is likely not a factor. Therefore we believe that the eruption of the filament dominates the acceleration of the jet in this case, therefore any evidence of velocity associated with chromospheric evaporation is lost.

Jet 4 is a large active region, blow-out jet associated with the ejection of a filament, and CME-like mass through a complex 2-step eruption. We did not find any evidence of chromospheric evaporation in this jet while using the temperature-velocity analysis. The overall temperature and velocity are higher than other jets, but they are not correlated. Jet 4, was discussed by [Chen et al., 2018], where we used the flux rope insertion method to model the magnetic topology and found evidence of semi-relativistic particles that could be traced by to the reconnection site. We also calculated the squashing factor,Q, for this region and find strong correlations between the magnetic null regions and regions of enhanced current density as predicted by the NLFFF model. In Jet 4, we show that the post-eruption configuration contains an extensive seperatrix region, making future eruptions likely. The AR associated with Jet 4 is associated with several C-class flares, 9 days after the jet eruption. There are two scenarios for flare production that can be tested using NLFF model. It is possible that the closed field region again reconnects. However, now that the closed field encompasses a larger area, this scenario could result in a failed eruption. Failed eruptions are sometimes observed in active regions when an eruption occurs, but it does not escape the inner corona and the ejected material returns along closed magnetic field lines. In those cases the magnetic field tension of the overlying field is greater than the field strength and/or the same direction as the expanding underlying region. It is possible that the new field configuration allows the storage, of magnetic energy but not the release, forcing potential magnetic energy to increase until the closed field gives way, resulting in a larger

eruption as discussed by Antiochos [1996], Antiochos et al. [2002]. Another possibility is that smaller, failed eruptions continue to re-reorganize and expand the overlying field, until reaching an open field (or opposite direction) region allowing external reconnection (flare) and the release of the inner structure in the form of a CME as proposed by Forbes and Isenberg [1991], Lin and Forbes [2000]. In future work, we intend to continue field relaxation to determine if additional eruptions occur and the resulting configuration.

Jets 5 and 6 were not modeled using the NLFFF model, but will be included in a future study. The velocity of some channels of Jet 5 show a slight dependence on temperature. This jet is a standard jet, but it is also associated with the ejection of a filament and oscillatory behavior with periods, on the order of 4 minutes. The site of this jet is the location of several repeating jets and a long-lived sigmoidal active region. The velocity for channels Iris1330, 1400, AIA 171,193, 211, are increasing in a trend very similar to what is expected for chromospheric evaporation. However, the X-ray velocities lie on the cusp of the upper limit for chromospheric evaporation. It is possible that chromospheric evaporation plays a small role in the acceleration of the cooler channels, but magnetic tension for torsional Alfvén waves are more relevant. Topological modeling in a later study should be more revealing of the acceleration mechanism.

Jet 6 is best described as a standard jet, since its spire is narrow, however it is also associated with oscillatory behavior similar to the other jets. However, unlike to others, this jet does not appear to have a filament and its ejecta does not leave along open radial magnetic field lines. There are several dark regions near the jet, which we interpret as coronal dimming, similar to dimming observed in CMEs. Some channels, AIA 171, 193, and 94c Å, increase as a function of temperature, as expected with chromospheric evaporation, however the other channels do not follow a similar trend. Therefore, we do not think chromospheric evaporation is responsible for this jet. IRIS spectroscopic analysis along the spire of this jet, indicated the presence of bidirectional flows and enhanced non-thermal broadening for a few pixels at the jet base. Topological modeling could show if

these regions correlate with magnetic null regions, supporting the idea that they are the site of magnetic reconnection.

In this work, we have shown that multiple mechanisms may be responsible for the acceleration of coronal jets and that the combination of observational tests and magnetic modeling are useful in understanding their complex formation. Previous studies of jets using high spatial and temporal resolution instruments have primarily relied on MHD modeling and/or case observational studies to investigate formation and acceleration of coronal jets. This research demonstrates a novel technique that can identify the drivers of their complex structures, and examines how several acceleration mechanisms may act in tandem.

Future narrow-band observations of jets will be instrumental in developing unified jet models. However, because jets occur sporadically, spectroscopic observations of jets are rare. Furthermore, non-thermal heating is difficult to detect with the limited dynamic range and sensitivity of current EUV and X-ray instrumentation. Direct focusing X-ray telescopes such as the proposed Focusing Optics X-ray Solar Imager (FOXSI) mission [**?**] could alleviate these problems. Another limitation is the lack of direct measurements of the coronal magnetic field. NLFFF models allow us to map the coronal magnetic field of jets based on photospheric magnetograms. A better constraint would be direct coronal magnetic field measurements. Currently direct measurements of the corona are not substantial for large scale jet studies. The newly commissioned Daniel K. Inouye Solar Telescope (DKIST) [Schmidt et al., 2016], instrument has begun making measurements of the chromospheric magnetic field and will be able to advance our understanding of the complex structure of coronal jets.

5.1 Acknowledgements

Hinode is a Japanese mission developed and launched by ISAS/JAXA, with NAOJ as domestic partner and NASA and STFC (UK) as international partners. It is operated by these agencies in co-operation with ESA and the NSC (Norway).IRIS is a NASA small

explorer mission developed and operated by LMSAL with mission operations executed at NASA Ames Research center and major contributions to downlink communications funded by ESA and the Norwegian Space Centre. This work was supported by NSF grant number NNX15AF43G.

LIST OF ABBREVIATIONS

CCD Charge Coupled Device

FWHM Full Width Half-Maximum

POS Plane-of-Sky

BIBLIOGRAPHY

L. W. Acton, J. W. Leibacher, R. C. Canfield, T. A. Gunkler, H. S. Hudson, and A. L. Kiplinger. Chromospheric evaporation in a well-observed compact flare. , 263:409–422, Dec 1982. doi: 10.1086/160513.

D. Alexander and L. Fletcher. High-resolution Observations of Plasma Jets in the Solar Corona. , 190:167–184, Dec. 1999. doi: 10.1023/A:1005213826793.

H. Alfvén. Existence of Electromagnetic-Hydrodynamic Waves. , 150(3805):405–406, Oct 1942. doi: 10.1038/150405d0.

S. K. Antiochos. A Model for Coronal Mass Ejections. In *American Astronomical Society Meeting Abstracts*, volume 189 of *American Astronomical Society Meeting Abstracts*, page 56.03, Dec 1996.

S. K. Antiochos and P. A. Sturrock. Evaporative cooling of flare plasma. , 220:1137–1143, Mar 1978. doi: 10.1086/155999.

S. K. Antiochos, P. J. MacNeice, D. S. Spicer, and J. A. Klimchuk. The Dynamic Formation of Prominence Condensations. , 512:985–991, Feb. 1999. doi: 10.1086/306804.

S. K. Antiochos, J. T. Karpen, and C. R. DeVore. Coronal Magnetic Field Relaxation by Null-Point Reconnection. , 575(1):578–584, Aug. 2002. doi: 10.1086/341193.

P. Antolin, K. Shibata, T. Kudoh, D. Shiota, and D. Brooks. Predicting Observational Signatures of Coronal Heating by Alfvén Waves and Nanoflares. , 688(1):669–682, Nov 2008. doi: 10.1086/591998.

V. Archontis and A. W. Hood. A Numerical Model of Standard to Blowout Jets. , 769(2): L21, Jun 2013. doi: 10.1088/2041-8205/769/2/L21.

V. Archontis and T. Török. Eruption of magnetic flux ropes during flux emergence. , 492 (2):L35–L38, Dec 2008. doi: 10.1051/0004-6361:200811131.

R. G. Athay. *The solar chromosphere and corona: Quiet sun*, volume 53. 1976. doi: 10.1007/978-94-010-1715-2.

G. Aulanier, E. Pariat, and P. Démoulin. Current sheet formation in quasi-separatrix layers and hyperbolic flux tubes. , 444(3):961–976, Dec. 2005. doi: 10.1051/0004-6361: 20053600.

D. Baker, L. van Driel-Gesztelyi, C. H. Mandrini, P. Démoulin, and M. J. Murray. Magnetic Reconnection along Quasi-separatrix Layers as a Driver of Ubiquitous Active Region Outflows. , 705(1):926–935, Nov 2009. doi: 10.1088/0004-637X/705/1/926.

J. M. Beckers. Solar Spicules. , 10:73, Jan 1972. doi: 10.1146/annurev.aa.10.090172. 000445.

A. Bhattacharjee and Y. C. Kwok. Relaxation of toroidal plasmas with finite pressure. *Physics of Fluids*, 29(4):1156–1160, Apr 1986. doi: 10.1063/1.865861.

A. Bhattacharjee, Y.-M. Huang, H. Yang, and B. Rogers. Fast reconnection in high-Lundquist-number plasmas due to the plasmoid Instability. *Physics of Plasmas*, 16(11): 112102, Nov 2009. doi: 10.1063/1.3264103.

M. G. Bobra, A. A. van Ballegooijen, and E. E. DeLuca. Modeling Nonpotential Magnetic Fields in Solar Active Regions. , 672(2):1209–1220, Jan 2008. doi: 10.1086/523927.

P. Boerner, C. Edwards, J. Lemen, A. Rausch, C. Schrijver, R. Shine, L. Shing, R. Stern, T. Tarbell, A. Title, C. J. Wolfson, R. Soufli, E. Spiller, E. Gullikson, D. McKenzie, D. Windt, L. Golub, W. Podgorski, P. Testa, and M. Weber. Initial Calibration of the Atmospheric Imaging Assembly (AIA) on the Solar Dynamics Observatory (SDO). , 275(1-2):41–66, Jan 2012. doi: 10.1007/s11207-011-9804-8.

P. F. Boerner, P. Testa, H. Warren, M. A. Weber, and C. J. Schrijver. Photometric and Thermal Cross-calibration of Solar EUV Instruments. , 289(6):2377–2397, Jun 2014. doi: 10.1007/s11207-013-0452-z.

A. H. Boozer. Ohm's law for mean magnetic fields. *Journal of Plasma Physics*, 35(1): 133–139, Feb 1986. doi: 10.1017/S0022377800011181.

M. Bout, P. Lamy, and A. Llebaria. Electron density in coronal jets. In A. Wilson, editor, *From Solar Min to Max: Half a Solar Cycle with SOHO*, volume 508 of *ESA Special Publication*, pages 379–382, Jun 2002.

P. K. Browning, C. Gerrard, A. W. Hood, R. Kevis, and R. A. M. van der Linden. Heating the corona by nanoflares: simulations of energy release triggered by a kink instability. , 485(3):837–848, Jul 2008. doi: 10.1051/0004-6361:20079192.

G. E. Brueckner, R. A. Howard, M. J. Koomen, C. M. Korendyke, D. J. Michels, J. D. Moses, D. G. Socker, K. P. Dere, P. L. Lamy, A. Llebaria, M. V. Bout, R. Schwenn, G. M. Simnett, D. K. Bedford, and C. J. Eyles. The Large Angle Spectroscopic Coronagraph (LASCO). , 162(1-2):357–402, Dec 1995. doi: 10.1007/BF00733434.

R. C. Canfield, K. P. Reardon, K. D. Leka, K. Shibata, T. Yokoyama, and M. Shimojo. H alpha Surges and X-Ray Jets in AR 7260. , 464:1016, June 1996. doi: 10.1086/177389.

P. J. Cargill. A Possible Difficulty with a Nanoflare-Heated Corona. , 167(1-2):267–279, Aug 1996. doi: 10.1007/BF00146339.

Chandra, R., Mandrini, C. H., Schmieder, B., Joshi, B., Cristiani, G. D., Cremades, H., Pariat, E., Nuevo, F. A., Srivastava, A. K., and Uddin, W. Blowout jets and impulsive eruptive flares in a bald-patch topology. *A&A*, 598:A41, 2017. doi: 10.1051/0004-6361/201628984. URL https://doi.org/10.1051/0004-6361/201628984.

K. Chandrashekhar, R. J. Morton, D. Banerjee, and G. R. Gupta. The dynamical behaviour of a jet in an on-disk coronal hole observed with AIA/SDO. , 562:A98, Feb 2014. doi: 10.1051/0004-6361/201322408.

B. Chen, S. Yu, M. Battaglia, S. Farid, A. Savcheva, K. K. Reeves, S. Krucker, T. S. Bastian, F. Guo, and S. Tassev. Magnetic Reconnection Null Points as the Origin of Semirelativistic Electron Beams in a Solar Jet. , 866(1):62, Oct 2018. doi: 10.3847/1538-4357/aadb89.

H.-D. Chen, J. Zhang, and S.-L. Ma. The kinematics of an untwisting solar jet in a polar coronal hole observed by SDO/AIA. *Research in Astronomy and Astrophysics*, 12(5): 573–583, May 2012. doi: 10.1088/1674-4527/12/5/009.

J. Chen. Structure of Non-force-free Magnetic Flux Ropes in an Ambient Medium. , 761 (2):179, Dec 2012. doi: 10.1088/0004-637X/761/2/179.

N. Chen, W.-H. Ip, and D. Innes. Flare-Associated Type III Radio Bursts and Dynamics of the EUV Jet from SDO/AIA and RHESSI Observations. , 769(2):96, Jun 2013. doi: 10.1088/0004-637X/769/2/96.

Y. Chen, G. Du, D. Zhao, Z. Wu, W. Liu, B. Wang, G. Ruan, S. Feng, and H. Song. IMAGING a MAGNETIC-BREAKOUT SOLAR ERUPTION. *The Astrophysical Journal*, 820 (2):L37, mar 2016. doi: 10.3847/2041-8205/820/2/l37. URL https://doi.org/10.3847%2F2041-8205%2F820%2F2%2Fl37.

X. Cheng, J. Zhang, S. H. Saar, and M. D. Ding. Differential Emission Measure Analysis of Multiple Structural Components of Coronal Mass Ejections in the Inner Corona. , 761 (1):62, Dec. 2012. doi: 10.1088/0004-637X/761/1/62.

M. C. M. Cheung, B. De Pontieu, T. D. Tarbell, Y. Fu, H. Tian, P. Testa, K. K. Reeves, J. Martínez-Sykora, P. Boerner, J. P. Wülser, J. Lemen, A. M. Title, N. Hurlburt,

L. Kleint, C. Kankelborg, S. Jaeggli, L. Golub, S. McKillop, S. Saar, M. Carlsson, and V. Hansteen. Homologous Helical Jets: Observations By IRIS, SDO, and Hinode and Magnetic Modeling With Data-Driven Simulations. , 801(2):83, Mar 2015. doi: 10.1088/0004-637X/801/2/83.

C. Chifor, H. Isobe, H. E. Mason, I. G. Hannah, P. R. Young, G. Del Zanna, S. Krucker, K. Ichimoto, Y. Katsukawa, and T. Yokoyama. Magnetic flux cancellation associated with a recurring solar jet observed with Hinode, RHESSI, and STEREO/EUVI. , 491 (1):279–288, Nov 2008. doi: 10.1051/0004-6361:200810265.

G. Chintzoglou, A. Vourlidas, A. Savcheva, S. Tassev, S. Tun Beltran, and G. Stenborg. Magnetic Flux Rope Shredding By a Hyperbolic Flux Tube: The Detrimental Effects of Magnetic Topology on Solar Eruptions. , 843(2):93, July 2017. doi: 10.3847/1538-4357/aa77b2.

J. W. Cirtain, L. Golub, L. Lundquist, A. van Ballegooijen, A. Savcheva, M. Shimojo, E. DeLuca, S. Tsuneta, T. Sakao, K. Reeves, M. Weber, R. Kano, N. Narukage, and K. Shibasaki. Evidence for Alfvén Waves in Solar X-ray Jets. *Science*, 318:1580, Dec. 2007. doi: 10.1126/science.1147050.

N. U. Crooker, S. K. Antiochos, X. Zhao, and M. Neugebauer. Global network of slow solar wind. *Journal of Geophysical Research (Space Physics)*, 117(A4):A04104, Apr 2012. doi: 10.1029/2011JA017236.

B. De Pontieu, A. M. Title, J. R. Lemen, G. D. Kushner, D. J. Akin, B. Allard, T. Berger, P. Boerner, M. Cheung, C. Chou, J. F. Drake, D. W. Duncan, S. Freeland, G. F. Heyman, C. Hoffman, N. E. Hurlburt, R. W. Lindgren, D. Mathur, R. Rehse, D. Sabolish, R. Seguin, C. J. Schrijver, T. D. Tarbell, J. P. Wülser, C. J. Wolfson, C. Yanari, J. Mudge, N. Nguyen-Phuc, R. Timmons, R. van Bezooijen, I. Weingrod, R. Brookner, G. Butcher, B. Dougherty, J. Eder, V. Knagenhjelm, S. Larsen, D. Mansir, L. Phan, P. Boyle, P. N.

Cheimets, E. E. DeLuca, L. Golub, R. Gates, E. Hertz, S. McKillop, S. Park, T. Perry, W. A. Podgorski, K. Reeves, S. Saar, P. Testa, H. Tian, M. Weber, C. Dunn, S. Eccles, S. A. Jaeggli, C. C. Kankelborg, K. Mashburn, N. Pust, L. Springer, R. Carvalho, L. Kleint, J. Marmie, E. Mazmanian, T. M. D. Pereira, S. Sawyer, J. Strong, S. P. Worden, M. Carlsson, V. H. Hansteen, J. Leenaarts, M. Wiesmann, J. Aloise, K. C. Chu, R. I. Bush, P. H. Scherrer, P. Brekke, J. Martinez-Sykora, B. W. Lites, S. W. McIntosh, H. Uitenbroek, T. J. Okamoto, M. A. Gummin, G. Auker, P. Jerram, P. Pool, and N. Waltham. The Interface Region Imaging Spectrograph (IRIS). , 289(7):2733–2779, Jul 2014. doi: 10.1007/s11207-014-0485-y.

G. Del Zanna, K. P. Dere, P. R. Young, E. Landi, and H. E. Mason. CHIANTI - An atomic database for emission lines. Version 8. , 582:A56, Oct 2015. doi: 10.1051/0004-6361/201526827.

J.-P. Delaboudiniere, G. E. Artzner, J. Brunaud, A. H. Gabriel, J. F. Hochedez, F. Millier, X. Y. Song, B. Au, K. P. Dere, R. A. Howard, R. Kreplin, D. J. Michels, J. D. Moses, J. M. Defise, C. Jamar, P. Rochus, J. P. Chauvineau, J. P. Marioge, R. C. Catura, J. R. Lemen, L. Shing, R. A. Stern, J. B. Gurman, W. M. Neupert, A. Maucherat, F. Clette, P. Cugnon, and E. L. van Dessel. EIT: Extreme-Ultraviolet Imaging Telescope for the SOHO Mission. , 162:291–312, 1995.

P. Demoulin, L. van Driel-Gesztelyi, B. Schmieder, J. C. Hemoux, G. Csepura, and M. J. Hagyard. Evidence for magnetic reconnection in solar flares. , 271:292, Apr 1993.

P. Demoulin, J. C. Henoux, and C. H. Mandrini. Are magnetic null points important in solar flares ? , 285:1023–1037, May 1994.

K. P. Dere, G. D. Zanna, P. R. Young, E. Landi, and R. S. Sutherland. CHIANTI—an atomic database for emission lines. XV. version 9, improvements for the x-ray satellite

lines. *The Astrophysical Journal Supplement Series*, 241(2):22, mar 2019. doi: 10.3847/1538-4365/ab05cf. URL https://doi.org/10.3847%2F1538-4365%2Fab05cf.

V. Domingo, B. Fleck, and A. I. Poland. The SOHO Mission: an Overview. , 162(1-2): 1–37, Dec 1995. doi: 10.1007/BF00733425.

B. Filippov, A. K. Srivastava, B. N. Dwivedi, S. Masson, G. Aulanier, N. C. Joshi, and W. Uddin. Formation of a rotating jet during the filament eruption on 2013 April 10–11. *Monthly Notices of the Royal Astronomical Society*, 451(1):1117–1129, 06 2015. ISSN 0035-8711. doi: 10.1093/mnras/stv1039. URL https://doi.org/10.1093/mnras/stv1039.

G. H. Fisher, R. C. Canfield, and A. N. McClymont. Chromospheric evaporation velocities in solar flares. , 281:L79–L82, Jun 1984. doi: 10.1086/184290.

G. H. Fisher, R. C. Canfield, and A. N. McClymont. Flare Loop Radiative Hydrodynamics - Part Six - Chromospheric Evaporation due to Heating by Nonthermal Electrons. , 289: 425, Feb 1985. doi: 10.1086/162902.

T. G. Forbes and L. W. Acton. Reconnection and Field Line Shrinkage in Solar Flares. , 459:330–+, Mar. 1996. URL http://adsabs.harvard.edu/cgi-bin/nph-bib_query?bibcode=1996ApJ...459..330F&db_key=AST.

T. G. Forbes and P. A. Isenberg. A Catastrophe Mechanism for Coronal Mass Ejections. , 373:294, May 1991. doi: 10.1086/170051.

T. G. Forbes and J. M. Malherbe. A numerical simulation of magnetic reconnection and radiative cooling in line-tied current sheets. , 135(2):361–391, Oct 1991. doi: 10.1007/BF00147508.

S. L. Freeland and B. N. Handy. Data Analysis with the SolarSoft System. , 182(2): 497–500, Oct 1998. doi: 10.1023/A:1005038224881.

H. P. Furth, J. Killeen, and M. N. Rosenbluth. Finite-Resistivity Instabilities of a Sheet Pinch. *Physics of Fluids*, 6(4):459–484, Apr 1963. doi: 10.1063/1.1706761.

T. Gehrels, B. G. Marsden, R. S. McMillan, and J. V. Scotti. Astrometry with a scanning CCD. , 91:1242, May 1986. doi: 10.1086/114098.

M. K. Georgoulis, D. M. Rust, A. A. Pevtsov, P. N. Bernasconi, and K. M. Kuzanyan. Solar Magnetic Helicity Injected into the Heliosphere: Magnitude, Balance, and Periodicities Over Solar Cycle 23. , 705(1):L48–L52, Nov 2009. doi: 10.1088/0004-637X/705/1/L48.

L. Glesener and G. D. Fleishman. Electron Acceleration and Jet-facilitated Escape in an M-class Solar Flare on 2002 August 19. , 867(1):84, Nov 2018. doi: 10.3847/1538-4357/aacefe.

L. Golub, E. E. Deluca, A. Sette, and M. Weber. Differential Emission Measure Reconstruction with the SolarB X-Ray Telescope. In T. Sakurai & T. Sekii, editor, *The Solar-B Mission and the Forefront of Solar Physics*, volume 325 of *Astronomical Society of the Pacific Conference Series*, pages 217–+, Dec. 2004.

L. Golub, E. Deluca, G. Austin, J. Bookbinder, D. Caldwell, P. Cheimets, J. Cirtain, M. Cosmo, P. Reid, A. Sette, M. Weber, T. Sakao, R. Kano, K. Shibasaki, H. Hara, S. Tsuneta, K. Kumagai, T. Tamura, M. Shimojo, J. McCracken, J. Carpenter, H. Haight, R. Siler, E. Wright, J. Tucker, H. Rutledge, M. Barbera, G. Peres, and S. Varisco. The X-Ray Telescope (XRT) for the Hinode Mission. , 243(1):63–86, Jun 2007. doi: 10.1007/s11207-007-0182-1.

T. Gou, R. Liu, and Y. Wang. Do All Candle-Flame-Shaped Flares Have the Same Temperature Distribution? , 290(8):2211–2230, Aug 2015. doi: 10.1007/s11207-015-0750-8.

L. M. Green, B. Kliem, T. Török, L. van Driel-Gesztelyi, and G. D. R. Attrill. Transient Coronal Sigmoids and Rotating Erupting Flux Ropes. , 246(2):365–391, Dec 2007. doi: 10.1007/s11207-007-9061-z.

G. E. Hale. On the Probable Existence of a Magnetic Field in Sun-Spots. , 28:315, Nov 1908. doi: 10.1086/141602.

Y. Hanaoka. Flares and Plasma Flow Caused by Interacting Coronal Loops. , 165(2): 275–301, May 1996. doi: 10.1007/BF00149715.

B. N. Handy, L. W. Acton, C. C. Kankelborg, C. J. Wolfson, D. J. Akin, M. E. Bruner, R. Caravalho, R. C. Catura, R. Chevalier, D. W. Duncan, C. G. Edwards, C. N. Feinstein, S. L. Freeland, F. M. Friedlaender, C. H. Hoffmann, N. E. Hurlburt, B. K. Jurcevich, N. L. Katz, G. A. Kelly, J. R. Lemen, M. Levay, R. W. Lindgren, D. P. Mathur, S. B. Meyer, S. J. Morrison, M. D. Morrison, R. W. Nightingale, T. P. Pope, R. A. Rehse, C. J. Schrijver, R. A. Shine, L. Shing, K. T. Strong, T. D. Tarbell, A. M. Title, D. D. Torgerson, L. Golub, J. A. Bookbinder, D. Caldwell, P. N. Cheimets, W. N. Davis, E. E. Deluca, R. A. McMullen, H. P. Warren, D. Amato, R. Fisher, H. Maldonado, and C. Parkinson. The transition region and coronal explorer. , 187:229–260, July 1999. doi: 10.1023/A:1005166902804.

J. W. Harvey. *Magnetic Fields Associated with Solar Active-Region Prominences.* PhD thesis, National Solar Observatory, Jun 1969.

J. Heyvaerts, E. R. Priest, and D. M. Rust. An emerging flux model for the solar phenomenon. , 216:123–137, Aug 1977. doi: 10.1086/155453.

J. Hong, Y. Jiang, J. Yang, Y. Bi, H. Li, B. Yang, and D. Yang. Coronal Bright Points Associated with Minifilament Eruptions. , 796(2):73, Dec 2014. doi: 10.1088/0004-637X/796/2/73.

J.-C. Hong, Y.-C. Jiang, J.-Y. Yang, R.-S. Zheng, Y. Bi, H.-D. Li, B. Yang, and D. Yang. Twist in a polar blowout jet. *Research in Astronomy and Astrophysics*, 13:253–258, Mar. 2013. doi: 10.1088/1674-4527/13/3/001.

H. Iijima and T. Yokoyama. A three-dimensional magnetohydrodynamic simulation of the formation of solar chromospheric jets with twisted magnetic field lines. *The Astrophysical Journal*, 848(1):38, oct 2017. doi: 10.3847/1538-4357/aa8ad1. URL https://doi.org/10.3847%2F1538-4357%2Faa8ad1.

D. E. Innes, A. Genetelli, R. Attie, and H. E. Potts. Quiet Sun mini-coronal mass ejections activated by supergranular flows. , 495(1):319–323, Feb 2009. doi: 10.1051/0004-6361:200811011.

D. E. Innes, R. Bučík, L. J. Guo, and N. Nitta. Observations of solar X-ray and EUV jets and their related phenomena. *Astronomische Nachrichten*, 337(10):1024, Nov 2016. doi: 10.1002/asna.201612428.

M. Janvier, A. Savcheva, E. Pariat, S. Tassev, S. Millholland, V. Bommier, P. McCauley, S. McKillop, and F. Dougan. Evolution of flare ribbons, electric currents, and quasi-separatrix layers during an X-class flare. , 591:A141, July 2016. doi: 10.1051/0004-6361/201628406.

Y. Jiang, L. Yang, K. Li, and Y. Shen. Magnetic Interaction: An Erupting Filament and a Remote Coronal Hole. , 667(1):L105–L108, Sep 2007. doi: 10.1086/521949.

N. C. Joshi, N. Nishizuka, B. Filippov, T. Magara, and A. G. Tlatov. Flux rope breaking and formation of a rotating blowout jet. *Monthly Notices of the Royal Astronomical Society*, 476(1):1286–1298, 02 2018. ISSN 0035-8711. doi: 10.1093/mnras/sty322. URL https://doi.org/10.1093/mnras/sty322.

M. L. Kaiser, T. A. Kucera, J. M. Davila, O. C. St. Cyr, M. Guhathakurta, and E. Christian. The STEREO Mission: An Introduction. , 136(1-4):5–16, Apr 2008. doi: 10.1007/s11214-007-9277-0.

N. Karna, A. Savcheva, K. Dalmasse, S. Gibson, S. Tassev, G. de Toma, and E. E. DeLuca.

Forward Modeling of a Pseudostreamer. , 883(1):74, Sep 2019. doi: 10.3847/1538-4357/ab3c50.

M. Karovska. Enhancement of Lasco C1, C2, and C3 Coronagraph Images. Technical report, Jan 1999.

J. T. Karpen, S. K. Antiochos, and C. R. DeVore. The Mechanisms for the Onset and Explosive Eruption of Coronal Mass Ejections and Eruptive Flares. , 760(1):81, Nov 2012. doi: 10.1088/0004-637X/760/1/81.

Y.-H. Kim, Y.-J. Moon, Y.-D. Park, T. Sakurai, J. Chae, K. S. Cho, and S.-C. Bong. Small-Scale X-Ray/EUV Jets Seen in Hinode XRT and TRACE. , 59:S763, Nov 2007. doi: 10.1093/pasj/59.sp3.S763.

A. R. Kobelski, S. H. Saar, M. A. Weber, D. E. McKenzie, and K. K. Reeves. Calibrating Data from the Hinode/X-Ray Telescope and Associated Uncertainties. , 289(7):2781–2802, Jul 2014. doi: 10.1007/s11207-014-0487-9.

T. Kosugi, K. Matsuzaki, T. Sakao, T. Shimizu, Y. Sone, S. Tachikawa, T. Hashimoto, K. Minesugi, A. Ohnishi, T. Yamada, S. Tsuneta, H. Hara, K. Ichimoto, Y. Suematsu, M. Shimojo, T. Watanabe, S. Shimada, J. M. Davis, L. D. Hill, J. K. Owens, A. M. Title, J. L. Culhane, L. K. Harra, G. A. Doschek, and L. Golub. The Hinode (Solar-B) Mission: An Overview. , 243(1):3–17, Jun 2007. doi: 10.1007/s11207-007-9014-6.

J. R. Kuhn and R. F. Stein. Accounting for the Solar Acoustic and Luminosity Variations from the Deep Convection Zone. , 463:L117, Jun 1996. doi: 10.1086/310067.

P. Kumar, J. T. Karpen, S. K. Antiochos, P. F. Wyper, C. R. DeVore, and C. E. DeForest. Evidence for the Magnetic Breakout Model in an Equatorial Coronal-hole Jet. , 854(2):155, Feb 2018. doi: 10.3847/1538-4357/aaab4f.

K.-S. Lee, D. E. Innes, Y.-J. Moon, K. Shibata, J.-Y. Lee, and Y.-D. Park. FAST EXTREME-ULTRAVIOLET DIMMING ASSOCIATED WITH a CORONAL JET SEEN IN MULTI-WAVELENGTH AND STEREOSCOPIC OBSERVATIONS. *The Astrophysical Journal*, 766(1):1, feb 2013. doi: 10.1088/0004-637x/766/1/1. URL https://doi.org/10.1088%2F0004-637x%2F766%2F1%2F1.

J. R. Lemen, A. M. Title, D. J. Akin, P. F. Boerner, C. Chou, J. F. Drake, D. W. Duncan, C. G. Edwards, F. M. Friedlaender, G. F. Heyman, N. E. Hurlburt, N. L. Katz, G. D. Kushner, M. Levay, R. W. Lindgren, D. P. Mathur, E. L. McFeaters, S. Mitchell, R. A. Rehse, C. J. Schrijver, L. A. Springer, R. A. Stern, T. D. Tarbell, J.-P. Wuelser, C. J. Wolfson, C. Yanari, J. A. Bookbinder, P. N. Cheimets, D. Caldwell, E. E. Deluca, R. Gates, L. Golub, S. Park, W. A. Podgorski, R. I. Bush, P. H. Scherrer, M. A. Gummin, P. Smith, G. Auker, P. Jerram, P. Pool, R. Soufli, D. L. Windt, S. Beardsley, M. Clapp, J. Lang, and N. Waltham. The Atmospheric Imaging Assembly (AIA) on the Solar Dynamics Observatory (SDO). , pages 172–+, June 2011. doi: 10.1007/s11207-011-9776-8.

H. Li, Y. Jiang, J. Yang, B. Yang, Z. Xu, J. Hong, and Y. Bi. Rotating Magnetic Structures Associated with a Quasi-circular Ribbon Flare. , 836(2):235, Feb 2017. doi: 10.3847/1538-4357/aa5eac.

J. Lin and T. G. Forbes. Effects of reconnection on the coronal mass ejection process. , 105 (A2):2375–2392, Feb 2000. doi: 10.1029/1999JA900477.

C. Liu, N. Deng, J. Lee, T. Wiegelmann, R. L. Moore, and H. Wang. Evidence for Solar Tether-cutting Magnetic Reconnection from Coronal Field Extrapolations. , 778(2):L36, Dec 2013. doi: 10.1088/2041-8205/778/2/L36.

J. Liu, Y. Wang, and R. Erdélyi. How Many Twists Do Solar Coronal Jets Release? *Frontiers in Astronomy and Space Sciences*, 6:44, Jun 2019. doi: 10.3389/fspas.2019.00044.

W. Liu, T. E. Berger, A. M. Title, and T. D. Tarbell. An Intriguing Chromospheric Jet

Observed by Hinode: Fine Structure Kinematics and Evidence of Unwinding Twists. , 707(1):L37–L41, Dec 2009. doi: 10.1088/0004-637X/707/1/L37.

W. Liu, T. E. Berger, A. M. Title, T. D. Tarbell, and B. C. Low. Chromospheric Jet and Growing "Loop" Observed by Hinode: New Evidence of Fan-spine Magnetic Topology Resulting from Flux Emergence. , 728(2):103, Feb 2011. doi: 10.1088/0004-637X/728/2/103.

D. W. Longcope, A. C. Des Jardins, T. Carranza-Fulmer, and J. Qiu. A Quantitative Model of Energy Release and Heating by Time-dependent, Localized Reconnection in a Flare with Thermal Loop-top X-ray Source. , 267(1):107–139, Nov 2010. doi: 10.1007/s11207-010-9635-z.

B. C. Low and M. Zhang. The Hydromagnetic Origin of the Two Dynamical Types of Solar Coronal Mass Ejections. , 564:L53–L56, Jan. 2002. doi: 10.1086/338798.

A. T. Y. Lui. Comment on "Tail Reconnection Triggering Substorm Onset". *Science*, 324 (5933):1391, Jun 2009. doi: 10.1126/science.1167726.

B. J. Lynch, S. K. Antiochos, C. R. DeVore, J. G. Luhmann, and T. H. Zurbuchen. Topological Evolution of a Fast Magnetic Breakout CME in Three Dimensions. , 683(2):1192–1206, Aug 2008. doi: 10.1086/589738.

D. H. Mackay, L. M. Green, and A. van Ballegooijen. Modeling the Dispersal of an Active Region: Quantifying Energy Input into the Corona. , 729(2):97, Mar 2011. doi: 10.1088/0004-637X/729/2/97.

J. T. Mariska. *The Solar Transition Region*. 1992.

P. C. H. Martens. Yohkoh-SXT Observations of reconnection. *Advances in Space Research*, 32(6):905–916, Sep 2003. doi: 10.1016/S0273-1177(03)00292-8.

S. F. Martin. Conditions for the Formation and Maintenance of Filaments (Invited Review). , 182:107–137, Sept. 1998. doi: 10.1023/A:1005026814076.

S. Masuda, T. Kosugi, H. Hara, S. Tsuneta, and Y. Ogawara. A loop-top hard X-ray source in a compact solar flare as evidence for magnetic reconnection. , 371(6497):495–497, Oct 1994. doi: 10.1038/371495a0.

Y. Matsui, T. Yokoyama, N. Kitagawa, and S. Imada. MULTI-WAVELENGTH SPECTROSCOPIC OBSERVATION OF EXTREME-ULTRAVIOLET JET IN AR 10960. *The Astrophysical Journal*, 759(1):15, oct 2012. doi: 10.1088/0004-637x/759/1/15. URL https://doi.org/10.1088%2F0004-637x%2F759%2F1%2F15.

D. E. McKenzie and S. L. Savage. Quantitative Examination of Supra-arcade Downflows in Eruptive Solar Flares. , 697(2):1569–1577, Jun 2009. doi: 10.1088/0004-637X/697/2/1569.

D. L. McKenzie. Properties of solar coronal active regions deduced from X-ray line spectra. , 322:512–521, Nov. 1987. doi: 10.1086/165747.

K. A. Meyer, J. Sabol, D. H. Mackay, and A. A. van Ballegooijen. The Storage and Dissipation of Magnetic Energy in the Quiet Sun Corona Determined from SDO/HMI Magnetograms. , 770(2):L18, Jun 2013. doi: 10.1088/2041-8205/770/2/L18.

K. A. Meyer, A. S. Savcheva, D. H. Mackay, and E. E. DeLuca. Nonlinear Force-free Field Modeling of Solar Coronal Jets in Theoretical Configurations. , 880(1):62, Jul 2019. doi: 10.3847/1538-4357/ab271a.

T. Miyagoshi and T. Yokoyama. Magnetohydrodynamic Numerical Simulations of Solar X-Ray Jets Based on the Magnetic Reconnection Model That Includes Chromospheric Evaporation. , 593(2):L133–L136, Aug 2003. doi: 10.1086/378215.

R. L. Moore and G. Roumeliotis. *Triggering of Eruptive Flares - Destabilization of the Preflare Magnetic Field Configuration*, volume 399, page 69. 1992. doi: 10.1007/3-540-55246-4_79.

R. L. Moore and A. C. Sterling. Initiation of Coronal Mass Ejections. *Washington DC American Geophysical Union Geophysical Monograph Series*, 165:43, Oct 2006. doi: 10.1029/165GM07.

R. L. Moore, J. W. Cirtain, A. C. Sterling, and D. A. Falconer. Dichotomy of Solar Coronal Jets: Standard Jets and Blowout Jets. , 720:757–770, Sept. 2010. doi: 10.1088/0004-637X/720/1/757.

R. L. Moore, A. C. Sterling, and N. K. Panesar. Onset of the Magnetic Explosion in Solar Polar Coronal X-Ray Jets. , 859(1):3, May 2018. doi: 10.3847/1538-4357/aabe79.

F. Moreno-Insertis, K. Galsgaard, and I. Ugarte-Urra. Jets in Coronal Holes: Hinode Observations and Three-dimensional Computer Modeling. , 673(2):L211, Feb 2008. doi: 10.1086/527560.

S. M. Mulay, D. Tripathi, G. Del Zanna, and H. Mason. Multiwavelength study of 20 jets that emanate from the periphery of active regions. , 589:A79, May 2016. doi: 10.1051/0004-6361/201527473.

S. M. Mulay, G. Del Zanna, and H. Mason. Temperature and density structure of a recurring active region jet. , 598:A11, Feb 2017. doi: 10.1051/0004-6361/201628796.

N. Narukage, T. Sakao, R. Kano, H. Hara, M. Shimojo, T. Bando, F. Urayama, E. Deluca, L. Golub, M. Weber, P. Grigis, J. Cirtain, and S. Tsuneta. Coronal-Temperature-Diagnostic Capability of the Hinode/ X-Ray Telescope Based on Self-Consistent Calibration. , 269(1):169–236, Mar 2011. doi: 10.1007/s11207-010-9685-2.

N. Narukage, T. Sakao, R. Kano, M. Shimojo, A. Winebarger, M. Weber, and K. K. Reeves. Coronal-Temperature-Diagnostic Capability of the Hinode/ X-Ray Telescope Based on Self-consistent Calibration. II. Calibration with On-Orbit Data. , 289(3):1029–1042, Mar 2014. doi: 10.1007/s11207-013-0368-7.

W. M. Neupert. Comparison of Solar X-Ray Line Emission with Microwave Emission during Flares. , 153:L59, Jul 1968. doi: 10.1086/180220.

A. Nindos. Magnetic helicity of solar active regions. In N. Gopalswamy and D. F. Webb, editors, *Universal Heliophysical Processes*, volume 257 of *IAU Symposium*, pages 133–143, Mar 2009. doi: 10.1017/S1743921309029184.

A. Nindos and M. D. Andrews. The Association of Big Flares and Coronal Mass Ejections: What Is the Role of Magnetic Helicity? , 616(2):L175–L178, Dec 2004. doi: 10.1086/426861.

G. Nisticò, V. Bothmer, S. Patsourakos, and G. Zimbardo. Observational features of equatorial coronal hole jets. *Annales Geophysicae*, 28(3):687–696, Mar 2010. doi: 10.5194/angeo-28-687-2010.

N. V. Nitta, G. M. Mason, L. Wang, C. M. S. Cohen, and M. E. Wiedenbeck. Solar Sources of ^{3}He-rich Solar Energetic Particle Events in Solar Cycle 24. , 806(2):235, Jun 2015. doi: 10.1088/0004-637X/806/2/235.

B. O'Dwyer, G. Del Zanna, H. E. Mason, M. A. Weber, and D. Tripathi. SDO/AIA response to coronal hole, quiet Sun, active region, and flare plasma. , 521:A21, Oct. 2010. doi: 10.1051/0004-6361/201014872.

O´Dwyer, B., Del Zanna, G., and Mason, H. E. Response of hinode xrt to quiet sun, active region and flare plasma. *A&A*, 561:A20, 2014. doi: 10.1051/0004-6361/201016346. URL https://doi.org/10.1051/0004-6361/201016346.

Y. Ogawara, T. Takano, T. Kato, T. Kosugi, S. Tsuneta, T. Watanabe, I. Kondo, and Y. Uchida. The SOLAR-A Mission - An Overview. , 136:1–16, Nov. 1991. doi: 10.1007/BF00151692.

N. K. Panesar, A. C. Sterling, R. L. Moore, and P. Chakrapani. Magnetic Flux Cancelation as the Trigger of Solar Quiet-region Coronal Jets. , 832(1):L7, Nov 2016. doi: 10.3847/2041-8205/832/1/L7.

N. K. Panesar, A. C. Sterling, and R. L. Moore. Magnetic flux cancellation as the origin of solar quiet-region pre-jet minifilaments. *The Astrophysical Journal*, 844(2):131, jul 2017. doi: 10.3847/1538-4357/aa7b77. URL https://doi.org/10.3847%2F1538-4357%2Faa7b77.

N. K. Panesar, A. C. Sterling, R. L. Moore, S. K. Tiwari, B. De Pontieu, and A. A. Norton. IRIS and SDO Observations of Solar Jetlets Resulting from Network-edge Flux Cancelation. , 868(2):L27, Dec 2018. doi: 10.3847/2041-8213/aaef37.

A. R. Paraschiv and A. Donea. On solar recurrent coronal jets: Coronal geysers as sources of electron beams and interplanetary type-III radio bursts. *The Astrophysical Journal*, 873(2):110, mar 2019. doi: 10.3847/1538-4357/ab04a6. URL https://doi.org/10.3847%2F1538-4357%2Fab04a6.

E. Pariat, S. K. Antiochos, and C. R. DeVore. A Model for Solar Polar Jets. , 691:61–74, Jan. 2009. doi: 10.1088/0004-637X/691/1/61.

E. Pariat, S. K. Antiochos, and C. R. DeVore. Three-dimensional Modeling of Quasi-homologous Solar Jets. , 714(2):1762–1778, May 2010. doi: 10.1088/0004-637X/714/2/1762.

E. Pariat, K. Dalmasse, C. R. DeVore, S. K. Antiochos, and J. T. Karpen. Model for straight and helical solar jets. I. Parametric studies of the magnetic field geometry. , 573:A130, Jan 2015a. doi: 10.1051/0004-6361/201424209.

E. Pariat, G. Valori, P. Démoulin, and K. Dalmasse. Testing magnetic helicity conservation in a solar-like active event. , 580:A128, Aug 2015b. doi: 10.1051/0004-6361/201525811.

E. N. Parker. Topological Dissipation and the Small-Scale Fields in Turbulent Gases. , 174:499–+, June 1972. doi: 10.1086/151512.

E. N. Parker. Magnetic neutral sheets in evolving fields. I - General theory. , 264:635–647, Jan. 1983. doi: 10.1086/160636.

S. Patsourakos and J. A. Klimchuk. Nonthermal Spectral Line Broadening and the Nanoflare Model. , 647(2):1452–1465, Aug 2006. doi: 10.1086/505517.

S. Patsourakos, E. Pariat, A. Vourlidas, S. K. Antiochos, and J. P. Wuelser. STEREO SECCHI Stereoscopic Observations Constraining the Initiation of Polar Coronal Jets. , 680:L73, June 2008. doi: 10.1086/589769.

R. A. Perley, C. J. Chandler, B. J. Butler, and J. M. Wrobel. THE EXPANDED VERY LARGE ARRAY: A NEW TELESCOPE FOR NEW SCIENCE. *The Astrophysical Journal*, 739(1):L1, aug 2011. doi: 10.1088/2041-8205/739/1/l1. URL https://doi.org/10.1088%2F2041-8205%2F739%2F1%2Fl1.

W. D. Pesnell, B. J. Thompson, and P. C. Chamberlin. The Solar Dynamics Observatory (SDO). , 275(1-2):3–15, Jan 2012. doi: 10.1007/s11207-011-9841-3.

I. M. Podgorny and A. I. Podgorny. Physical Mechanism of a Solar Flare Based on the Accumulation of the Energy in the Magnetic Field of the Current Sheet in the Solar Corona. *Cosmic Research*, 57(6):389–406, Jan 2020. doi: 10.1134/S0010952519060054.

E. R. Priest, A. W. Hood, and U. Anzer. A Twisted Flux-Tube Model for Solar Prominences. I. General Properties. , 344:1010, Sept. 1989. doi: 10.1086/167868.

E. R. Priest, C. E. Parnell, and S. F. Martin. A converging flux model of an X-ray bright point and an associated canceling magnetic feature. , 427:459–474, May 1994. doi: 10.1086/174157.

E. R. Priest, J. F. Heyvaerts, and A. M. Title. A Flux-Tube Tectonics Model for Solar Coronal Heating Driven by the Magnetic Carpet. , 576(1):533–551, Sept. 2002. doi: 10.1086/341539.

L. A. Rachmeler, E. Pariat, C. E. DeForest, S. Antiochos, and T. Török. Symmetric Coronal Jets: A Reconnection-controlled Study. , 715(2):1556–1565, Jun 2010. doi: 10.1088/0004-637X/715/2/1556.

N. E. Raouafi and G. Stenborg. Role of Transients in the Sustainability of Solar Coronal Plumes. , 787(2):118, Jun 2014. doi: 10.1088/0004-637X/787/2/118.

N. E. Raouafi, M. K. Georgoulis, D. M. Rust, and P. N. Bernasconi. Micro-sigmoids as Progenitors of Coronal Jets: Is Eruptive Activity Self-similarly Multi-scaled? , 718(2):981–987, Aug 2010. doi: 10.1088/0004-637X/718/2/981.

N. E. Raouafi, S. Patsourakos, E. Pariat, P. R. Young, A. C. Sterling, A. Savcheva, M. Shimojo, F. Moreno-Insertis, C. R. DeVore, V. Archontis, T. Török, H. Mason, W. Curdt, K. Meyer, K. Dalmasse, and Y. Matsui. Solar Coronal Jets: Observations, Theory, and Modeling. , 201(1-4):1–53, Nov 2016. doi: 10.1007/s11214-016-0260-5.

K. K. Reeves, T. B. Guild, W. J. Hughes, K. E. Korreck, J. Lin, J. Raymond, S. Savage, N. A. Schwadron, H. E. Spence, D. F. Webb, and M. Wiltberger. Posteruptive phenomena in coronal mass ejections and substorms: Indicators of a universal process? *Journal of Geophysical Research (Space Physics)*, 113(A9):A00B02, Sep 2008. doi: 10.1029/2008JA013049.

K. K. Reeves, P. I. McCauley, and H. Tian. Direct Observations of Magnetic Reconnection

Outflow and CME Triggering in a Small Erupting Solar Prominence. , 807(1):7, Jul 2015. doi: 10.1088/0004-637X/807/1/7.

T. Sakao, R. Kano, N. Narukage, J. Kotoku, T. Bando, E. E. DeLuca, L. L. Lundquist, S. Tsuneta, L. K. Harra, Y. Katsukawa, M. Kubo, H. Hara, K. Matsuzaki, M. Shimojo, J. A. Bookbinder, L. Golub, K. E. Korreck, Y. Su, K. Shibasaki, T. Shimizu, and I. Nakatani. Continuous Plasma Outflows from the Edge of a Solar Active Region as a Possible Source of Solar Wind. *Science*, 318:1585–, Dec. 2007. doi: 10.1126/science.1147292.

S. L. Savage, D. E. McKenzie, K. K. Reeves, T. G. Forbes, and D. W. Longcope. Reconnection Outflows and Current Sheet Observed with Hinode/XRT in the 2008 April 9 "Cartwheel CME" Flare. , 722(1):329–342, Oct 2010. doi: 10.1088/0004-637X/722/1/329.

S. L. Savage, G. Holman, K. K. Reeves, D. B. Seaton, D. E. McKenzie, and Y. Su. Low-altitude Reconnection Inflow-Outflow Observations during a 2010 November 3 Solar Eruption. , 754(1):13, Jul 2012. doi: 10.1088/0004-637X/754/1/13.

A. Savcheva and A. van Ballegooijen. Nonlinear Force-free Modeling of a Long-lasting Coronal Sigmoid. , 703:1766–1777, Oct. 2009. doi: 10.1088/0004-637X/703/2/1766.

A. Savcheva, J. Cirtain, E. E. Deluca, L. L. Lundquist, L. Golub, M. Weber, M. Shimojo, K. Shibasaki, T. Sakao, N. Narukage, S. Tsuneta, and R. Kano. A Study of Polar Jet Parameters Based on Hinode XRT Observations. , 59:771, Nov. 2007.

A. Savcheva, E. Pariat, A. van Ballegooijen, G. Aulanier, and E. DeLuca. Sigmoidal Active Region on the Sun: Comparison of a Magnetohydrodynamical Simulation and a Nonlinear Force-free Field Model. , 750(1):15, May 2012a. doi: 10.1088/0004-637X/750/1/15.

A. Savcheva, E. Pariat, S. McKillop, P. McCauley, E. Hanson, Y. Su, E. Werner, and E. E.

DeLuca. The Relation between Solar Eruption Topologies and Observed Flare Features. I. Flare Ribbons. , 810:96, Sept. 2015. doi: 10.1088/0004-637X/810/2/96.

A. S. Savcheva, A. A. van Ballegooijen, and E. E. DeLuca. Field Topology Analysis of a Long-lasting Coronal Sigmoid. , 744:78, Jan. 2012b. doi: 10.1088/0004-637X/744/1/78.

P. H. Scherrer, J. Schou, R. I. Bush, A. G. Kosovichev, R. S. Bogart, J. T. Hoeksema, Y. Liu, T. L. Duvall, J. Zhao, A. M. Title, C. J. Schrijver, T. D. Tarbell, and S. Tomczyk. The Helioseismic and Magnetic Imager (HMI) Investigation for the Solar Dynamics Observatory (SDO). , 275:207–227, Jan. 2012. doi: 10.1007/s11207-011-9834-2.

J. T. Schmelz, V. L. Kashyap, S. H. Saar, B. R. Dennis, P. C. Grigis, L. Lin, E. E. De Luca, G. D. Holman, L. Golub, and M. A. Weber. Some Like It Hot: Coronal Heating Observations from Hinode X-ray Telescope and RHESSI. , 704(1):863–869, Oct 2009a. doi: 10.1088/0004-637X/704/1/863.

J. T. Schmelz, S. H. Saar, E. E. DeLuca, L. Golub, V. L. Kashyap, M. A. Weber, and J. A. Klimchuk. Hinode X-Ray Telescope Detection of Hot Emission from Quiescent Active Regions: A Nanoflare Signature? , 693:L131–L135, Mar. 2009b. doi: 10.1088/0004-637X/693/2/L131.

J. T. Schmelz, S. H. Saar, K. Nasraoui, V. L. Kashyap, M. A. Weber, E. E. DeLuca, and L. Golub. Multi-stranded and Multi-thermal Solar Coronal Loops: Evidence from Hinode X-ray Telescope and EUV Imaging Spectrometer Data. , 723(2):1180–1187, Nov 2010. doi: 10.1088/0004-637X/723/2/1180.

W. Schmidt, M. Schubert, M. Ellwarth, J. Baumgartner, A. Bell, A. Fischer, C. Halbgewachs, F. Heidecke, T. Kentischer, O. von der Lühe, T. Scheiffelen, and M. Sigwarth. End-to-end simulations of the visible tunable filter for the Daniel K. Inouye Solar Telescope. In C. J. Evans, L. Simard, and H. Takami, editors, *Ground-based and*

Airborne Instrumentation for Astronomy VI, volume 9908, pages 1473 – 1483. International Society for Optics and Photonics, SPIE, 2016. doi: 10.1117/12.2232518. URL https://doi.org/10.1117/12.2232518.

B. Schmieder, P. Démoulin, and G. Aulanier. Solar filament eruptions and their physical role in triggering coronal mass ejections. *Advances in Space Research*, 51(11):1967–1980, Jun 2013. doi: 10.1016/j.asr.2012.12.026.

C. J. Schrijver, M. L. De Rosa, T. Metcalf, G. Barnes, B. Lites, T. Tarbell, J. McTiernan, G. Valori, T. Wiegelmann, M. S. Wheatland, T. Amari, G. Aulanier, P. Démoulin, M. Fuhrmann, K. Kusano, S. Régnier, and J. K. Thalmann. Nonlinear Force-free Field Modeling of a Solar Active Region around the Time of a Major Flare and Coronal Mass Ejection. , 675:1637–1644, Mar. 2008. doi: 10.1086/527413.

D. B. Seaton, A. E. Bartz, and J. M. Darnel. Observations of the Formation, Development, and Structure of a Current Sheet in an Eruptive Solar Flare. , 835(2):139, Feb 2017. doi: 10.3847/1538-4357/835/2/139.

F. Shen, X. S. Feng, S. T. Wu, C. Q. Xiang, and W. B. Song. Three-dimensional MHD simulation of the evolution of the April 2000 CME event and its induced shocks using a magnetized plasma blob model. *Journal of Geophysical Research (Space Physics)*, 116 (A4):A04102, Apr 2011a. doi: 10.1029/2010JA015809.

Y. Shen, Y. D. Liu, J. Su, Z. Qu, and Z. Tian. On a Solar Blowout Jet: Driving Mechanism and the Formation of Cool and Hot Components. , 851(1):67, Dec 2017. doi: 10.3847/1538-4357/aa9a48.

Y.-D. Shen, Y. Liu, and R. Liu. A time series of filament eruptions observed by three eyes from space: from failed to successful eruptions. *Research in Astronomy and Astrophysics*, 11(5):594–606, May 2011b. doi: 10.1088/1674-4527/11/5/009.

K. Shibata. Coronal x-ray jets: Observation and theory. In *Solar Wind Eight*, page 28, Jun 1995.

K. Shibata. Evidence of Magnetic Reconnection in Solar Flares and a Unified Model of Flares. , 264:129–144, Jan 1999. doi: 10.1023/A:1002413214356.

K. Shibata and T. Magara. Solar Flares: Magnetohydrodynamic Processes. *Living Reviews in Solar Physics*, 8(1):6, Dec 2011. doi: 10.12942/lrsp-2011-6.

K. Shibata, Y. Ishido, L. W. Acton, K. T. Strong, T. Hirayama, Y. Uchida, A. H. McAllister, R. Matsumoto, S. Tsuneta, T. Shimizu, H. Hara, T. Sakurai, K. Ichimoto, Y. Nishino, and Y. Ogawara. Observations of X-ray jets with the YOHKOH Soft X-ray Telescope. , 44: L173–L179, Oct. 1992a.

K. Shibata, Y. Ishido, L. W. Acton, K. T. Strong, T. Hirayama, Y. Uchida, A. H. McAllister, R. Matsumoto, S. Tsuneta, T. Shimizu, H. Hara, T. Sakurai, K. Ichimoto, Y. Nishino, and Y. Ogawara. Observations of X-ray jets with the YOHKOH Soft X-ray Telescope. , 44: L173–L179, Oct. 1992b.

K. Shibata, S. Nozawa, and R. Matsumoto. Magnetic Reconnection Associated with Emerging Magnetic Flux. , 44:265–272, Jun 1992c.

K. Shibata, S. Nozawa, and R. Matsumoto. Magnetic reconnection associated with emerging magnetic flux. , 44:265–272, June 1992d.

M. Shimojo, S. Hashimoto, K. Shibata, T. Hirayama, H. S. Hudson, and L. W. Acton. Statistical Study of Solar X-Ray Jets Observed with the YOHKOH Soft X-Ray Telescope. , 48:123–136, Feb. 1996.

M. Shimojo, K. Shibata, and K. L. Harvey. Magnetic Field Properties of Solar X-Ray Jets. , 178(2):379–392, Jan 1998. doi: 10.1023/A:1005091905214.

N. Soto, K. Reeves, and A. S. Savcheva. Mechanisms of Plasma Acceleration in Coronal Jets. In *AGU Fall Meeting Abstracts*, pages SH31B–2568, Dec. 2016.

A. C. Sterling and J. V. Hollweg. The Rebound Shock Model for Solar Spicules: Dynamics at Long Times. , 327:950, Apr 1988. doi: 10.1086/166252.

A. C. Sterling, C. Chifor, H. E. Mason, R. L. Moore, and P. R. Young. Evidence for magnetic flux cancelation leading to an ejective solar eruption observed by Hinode, TRACE, STEREO, and SoHO/MDI. , 521:A49, Oct 2010a. doi: 10.1051/0004-6361/201014006.

A. C. Sterling, L. K. Harra, and R. L. Moore. Fibrillar Chromospheric Spicule-like Counterparts to an Extreme-ultraviolet and Soft X-ray Blowout Coronal Jet. , 722(2):1644–1653, Oct 2010b. doi: 10.1088/0004-637X/722/2/1644.

A. C. Sterling, R. L. Moore, D. A. Falconer, and M. Adams. Small-scale filament eruptions as the driver of X-ray jets in solar coronal holes. , 523:437–440, July 2015. doi: 10.1038/nature14556.

A. C. Sterling, R. L. Moore, and N. K. Panesar. Magnetic Flux Cancelation as the Buildup and Trigger Mechanism for CME-producing Eruptions in Two Small Active Regions. , 864(1):68, Sep 2018. doi: 10.3847/1538-4357/aad550.

A. C. Sterling, L. K. Harra, R. L. Moore, and D. A. Falconer. A Two-sided Loop X-Ray Solar Coronal Jet Driven by a Minifilament Eruption. , 871(2):220, Feb 2019. doi: 10.3847/1538-4357/aaf1d3.

K. T. Strong, K. Harvey, T. Hirayama, N. Nitta, T. Shimizu, and S. Tsuneta. Observations of the variability of coronal bright points by the Soft X-ray Telescope on YOHKOH. , 44:L161–L166, Oct. 1992.

Y. Su, A. M. Veronig, G. D. Holman, B. R. Dennis, T. Wang, M. Temmer, and W. Gan.

Imaging coronal magnetic-field reconnection in a solar flare. *Nature Physics*, 9(8):489–493, Aug 2013. doi: 10.1038/nphys2675.

L. Sui and G. D. Holman. Evidence for the Formation of a Large-Scale Current Sheet in a Solar Flare. , 596(2):L251–L254, Oct 2003. doi: 10.1086/379343.

S. Tassev and A. Savcheva. QSL Squasher: A Fast Quasi-separatrix Layer Map Calculator. , 840(2):89, May 2017. doi: 10.3847/1538-4357/aa6f06.

S. Tassev and A. Savcheva. Coiling and Squeezing: Properties of the Local Transverse Deviations of Magnetic Field Lines. *arXiv e-prints*, art. arXiv:1901.00865, Jan. 2019.

J. K. Thalmann, S. K. Tiwari, and T. Wiegelmann. FORCE-FREE FIELD MODELING OF TWIST AND BRAIDING-INDUCED MAGNETIC ENERGY IN AN ACTIVE-REGION CORONA. *The Astrophysical Journal*, 780(1):102, dec 2013. doi: 10.1088/0004-637x/780/1/102. URL https://doi.org/10.1088%2F0004-637x%2F780%2F1%2F102.

H. Tian, G. Li, K. K. Reeves, J. C. Raymond, F. Guo, W. Liu, B. Chen, and N. A. Murphy. Imaging and Spectroscopic Observations of Magnetic Reconnection and Chromospheric Evaporation in a Solar Flare. , 797(2):L14, Dec 2014. doi: 10.1088/2041-8205/797/2/L14.

V. S. Titov. Generalized Squashing Factors for Covariant Description of Magnetic Connectivity in the Solar Corona. , 660(1):863–873, May 2007. doi: 10.1086/512671.

T. Török, B. Kliem, and V. S. Titov. Ideal kink instability of a magnetic loop equilibrium. , 413:L27–L30, Jan 2004. doi: 10.1051/0004-6361:20031691.

S. Tsuneta. Structure and Dynamics of Magnetic Reconnection in a Solar Flare. , 456:840, Jan 1996. doi: 10.1086/176701.

S. Tsuneta, L. Acton, M. Bruner, J. Lemen, W. Brown, R. Caravalho, R. Catura, S. Freeland, B. Jurcevich, M. Morrison, Y. Ogawara, T. Hirayama, and J. Owens. The Soft X-ray Telescope for the SOLAR-A Mission. , 136:37–67, Nov. 1991. doi: 10.1007/BF00151694.

S. Tsuneta, H. Hara, T. Shimizu, L. W. Acton, K. T. Strong, H. S. Hudson, and Y. Ogawara. Observation of a Solar Flare at the Limb with the YOHKOH Soft X-Ray Telescope. , 44:L63–L69, Oct 1992.

F. Urayama, T. Bando, R. Kano, H. Hara, N. Narukage, and T. Sakao. Molecular Contamination Assessments on <i>Hinode</i> X-Ray Telescope. *Japan Society of Aeronautical Space Sciences*, 56(658):536–542, Jan 2008. doi: 10.2322/jjsass.56.536.

A. A. van Ballegooijen. Electric currents in the solar corona and the existence of magnetostatic equilibrium. , 298:421–430, Nov 1985. doi: 10.1086/163626.

A. A. van Ballegooijen. Observations and Modeling of a Filament on the Sun. , 612: 519–529, Sept. 2004. doi: 10.1086/422512.

A. A. van Ballegooijen and S. R. Cranmer. Tangled Magnetic Fields in Solar Prominences. , 711(1):164–178, Mar 2010. doi: 10.1088/0004-637X/711/1/164.

A. A. van Ballegooijen, E. E. Deluca, K. Squires, and D. H. Mackay. Modeling magnetic flux ropes in the solar atmosphere. *Journal of Atmospheric and Solar-Terrestrial Physics*, 69(1-2):24–31, Feb 2007. doi: 10.1016/j.jastp.2006.06.007.

A. A. van Ballegooijen, M. Asgari-Targhi, S. R. Cranmer, and E. E. DeLuca. Heating of the Solar Chromosphere and Corona by Alfvén Wave Turbulence. , 736(1):3, Jul 2011. doi: 10.1088/0004-637X/736/1/3.

W. Wainwright. Analyzing Constraints on Coronal Jets Near Filaments and Sigmoid Active Regions Using Nonlinear Force-Free Models. In *American Astronomical Society*

Meeting Abstracts, American Astronomical Society Meeting Abstracts, page 210.06, Jan. 2020.

H. Wang, Y. Yan, T. Sakurai, and M. Zhang. Topology of Magnetic Field and Coronal Heating in Solar Active Regions - II. The Role of Quasi-Separatrix Layers. , 197(2): 263–273, Dec 2000. doi: 10.1023/A:1026566710505.

Y. M. Wang and J. Sheeley, N. R. Sources of the Solar Wind at Ulysses during 1990-2006. , 653(1):708–718, Dec 2006. doi: 10.1086/508929.

Y. M. Wang, J. Sheeley, N. R., D. G. Socker, R. A. Howard, G. E. Brueckner, D. J. Michels, D. Moses, O. C. St. Cyr, A. Llebaria, and J. P. Delaboudinière. Observations of Correlated White-Light and Extreme-Ultraviolet Jets from Polar Coronal Holes. , 508(2): 899–907, Dec 1998. doi: 10.1086/306450.

Y. M. Wang, P. Z. Ye, S. Wang, G. P. Zhou, and J. X. Wang. A statistical study on the geoeffectiveness of Earth-directed coronal mass ejections from March 1997 to December 2000. *Journal of Geophysical Research (Space Physics)*, 107(A11):1340, Nov 2002. doi: 10.1029/2002JA009244.

H. P. Warren, A. R. Winebarger, and D. H. Brooks. A Systematic Survey of High-temperature Emission in Solar Active Regions. , 759:141, Nov. 2012. doi: 10.1088/0004-637X/759/2/141.

H. P. Warren, D. H. Brooks, I. Ugarte-Urra, J. W. Reep, N. A. Crump, and G. A. Doschek. Spectroscopic Observations of Current Sheet Formation and Evolution. , 854(2):122, Feb 2018. doi: 10.3847/1538-4357/aaa9b8.

D. F. Webb, M. M. Bisi, C. A. de Koning, C. J. Farrugia, B. V. Jackson, L. K. Jian, N. Lugaz, K. Marubashi, C. Möstl, E. P. Romashets, B. E. Wood, and H. S. Yu. An Ensemble Study of a January 2010 Coronal Mass Ejection (CME): Connecting a Non-obvious

Solar Source with Its ICME/Magnetic Cloud. , 289(11):4173–4208, Nov 2014. doi: 10.1007/s11207-014-0571-1.

M. A. Weber, E. E. Deluca, L. Golub, and A. L. Sette. Temperature diagnostics with multichannel imaging telescopes. In A. V. Stepanov, E. E. Benevolenskaya, and A. G. Kosovichev, editors, *Multi-Wavelength Investigations of Solar Activity*, volume 223 of *IAU Symposium*, pages 321–328, Jan 2004. doi: 10.1017/S1743921304006088.

C.-C. Wei. Finite-Resistivity Instabilities of a Sheet Pinch. *Chinese Journal of Physics*, 6 (2):88, Apr 1968.

T. Wiegelmann. Nonlinear force-free modeling of the solar coronal magnetic field. *Journal of Geophysical Research (Space Physics)*, 113(A3):A03S02, Mar 2008. doi: 10.1029/2007JA012432.

T. Wiegelmann and T. Sakurai. Solar Force-free Magnetic Fields. *Living Reviews in Solar Physics*, 9(1):5, Sep 2012. doi: 10.12942/lrsp-2012-5.

A. R. Winebarger, J. T. Schmelz, H. P. Warren, S. H. Saar, and V. L. Kashyap. Using a Differential Emission Measure and Density Measurements in an Active Region Core to Test a Steady Heating Model. , 740(1):2, Oct 2011. doi: 10.1088/0004-637X/740/1/2.

G. L. Withbroe. The analysis of XUV emission lines. , 45:301–317, Dec. 1975. doi: 10.1007/BF00158452.

B. E. Wood, M. Karovska, J. W. Cook, R. A. Howard, and G. E. Brueckner. Kinematic Measurements of Polar Jets Observed by the Large-Angle Spectrometric Coronagraph. , 523(1):444–449, Sep 1999. doi: 10.1086/307721.

J. P. Wülser, S. Jaeggli, B. De Pontieu, T. Tarbell, P. Boerner, S. Freeland, W. Liu, R. Timmons, S. Brannon, C. Kankelborg, C. Madsen, S. McKillop, J. Prchlik, S. Saar,

N. Schanche, P. Testa, P. Bryans, and M. Wiesmann. Instrument Calibration of the Interface Region Imaging Spectrograph (IRIS) Mission. , 293(11):149, Nov 2018. doi: 10.1007/s11207-018-1364-8.

P. F. Wyper, C. R. DeVore, and S. K. Antiochos. Numerical simulation of helical jets at active region peripheries. , 490(3):3679–3690, Dec 2019. doi: 10.1093/mnras/stz2674.

J. Yang, Y. Jiang, B. Yang, J. Hong, D. Yang, Y. Bi, R. Zheng, and H. Li. A blowout surge from the eruption of a miniature filament confined by large coronal loops. , 17(8): 732–738, Nov 2012. doi: 10.1016/j.newast.2012.05.006.

W. H. Yang, P. A. Sturrock, and S. K. Antiochos. Force-free Magnetic Fields: The Magneto-frictional Method. , 309:383, Oct 1986. doi: 10.1086/164610.

T. Yokoyama. Magnetic reconnection model of coronal X-ray jets. In T.-D. Guyenne, editor, *Solar Jets and Coronal Plumes*, volume 421 of *ESA Special Publication*, page 215, Jan 1998.

T. Yokoyama and K. Shibata. Magnetic reconnection as the origin of X-ray jets and Hα surges on the Sun. , 375(6526):42–44, May 1995. doi: 10.1038/375042a0.

T. Yokoyama and K. Shibata. Numerical Simulation of Solar Coronal X-Ray Jets Based on the Magnetic Reconnection Model. , 48:353–376, Apr 1996a. doi: 10.1093/pasj/48.2.353.

T. Yokoyama and K. Shibata. MHD Simulation of Solar Coronal X-ray Jets: Emerging Flux Reconnection Model. *Astrophysical Letters and Communications*, 34:133, Jan 1996b.

T. Yokoyama and K. Shibata. Magnetohydrodynamic Simulation of a Solar Flare with Chromospheric Evaporation Effect Based on the Magnetic Reconnection Model. , 549 (2):1160–1174, Mar 2001. doi: 10.1086/319440.

P. R. Young and K. Muglach. Solar Dynamics Observatory and Hinode Observations of a Blowout Jet in a Coronal Hole. , 289(9):3313–3329, Sep 2014a. doi: 10.1007/s11207-014-0484-z.

P. R. Young and K. Muglach. A coronal hole jet observed with Hinode and the Solar Dynamics Observatory. , 66:S12, Dec 2014b. doi: 10.1093/pasj/psu088.

P. R. Young, G. Del Zanna, H. E. Mason, G. A. Doschek, L. Culhane, and H. Hara. Solar Transition Region Features Observed with Hinode/EIS. , 59:727–+, Nov. 2007.

Q. M. Zhang and H. S. Ji. A swirling flare-related EUV jet. , 561:A134, Jan 2014. doi: 10.1051/0004-6361/201322616.

Q. M. Zhang and L. Ni. Subarcsecond Blobs in Flare-related Coronal Jets. , 870(2):113, Jan 2019. doi: 10.3847/1538-4357/aaf391.

Q. M. Zhang, P. F. Chen, Y. Guo, C. Fang, and M. D. Ding. Two Types of Magnetic Reconnection in Coronal Bright Points and the Corresponding Magnetic Configuration. , 746:19, Feb. 2012. doi: 10.1088/0004-637X/746/1/19.

I. Zhelyazkov, R. Chandra, and A. K. Srivastava. Modeling Kelvin-Helmholtz Instability in Soft X-Ray Solar Jets. *Advances in Astronomy*, 2017:262649, Jan 2017. doi: 10.1155/2017/2626495.

C. Zhu, R. Liu, D. Alexander, and R. T. J. McAteer. Observation of the Evolution of a Current Sheet in a Solar Flare. , 821(2):L29, Apr 2016. doi: 10.3847/2041-8205/821/2/L29.

X. Zhu, H. Wang, X. Cheng, and C. Huang. A Solar Blowout Jet Caused by the Eruption of a Magnetic Flux Rope. , 844(2):L20, Aug 2017. doi: 10.3847/2041-8213/aa8033.